Title
Bio-inspired Methods for Reduction of Penetration Resistance in Granular Materials

Author
Hunt, Olivia Marie

Publication Date
2021

Peer reviewed|Thesis/dissertation

Bio-inspired Methods for Reduction of Penetration Resistance in Granular Materials

By

OLIVIA MARIE HUNT
THESIS

Submitted in partial satisfaction of the requirements for the degree of

MASTER OF SCIENCE

in

Civil Engineering

in the

OFFICE OF GRADUATE STUDIES

of the

UNIVERSITY OF CALIFORNIA

DAVIS

Approved:

Alejandro Martinez, Chair

Ross Boulanger

Jason DeJong

Committee in Charge

2021

Dedicated to my parents

ACKNOWLEDGEMENTS

Throughout graduate school I have received much support and encouragement. I would like to take a moment to thank those who have made this possible.

First, I would like to thank my advisor Alejandro Martinez for his many hours of assistance during my research and thesis writing. Thank you, Alejandro for all your efforts in writing proposals, and being an effective mentor, I am truly lucky to have had you as my advisor. I would also like to acknowledge the funding I received from NSF projects: EEC-1449501 and 1942369 as well as support from the PEGS21 program this research would not be possible. A special thank you to CBBG (Center for Bio-mediated and Bio-Inspired Geotechnics) for the support and learning opportunities that have been provided to me through the center.

Without the contributions from my research group, I would not be where I am today. Thank you, Kyle O'Hara, Yuyan Chen, Mandeep Basson, Sharif Ahmed, Jasmine Miller, Lin Huang, Alejandro Perez, and Sam Follett for your input on my research throughout the past two years and for always being available when I needed help. I especially want to thank Yuyan Chen for the time she has spent helping me with the simulation code, post-processing code, and in PFC. Without her help my research would have not been possible.

Additionally, I would like to thank all my professors at UC Davis. Thank you, Norman Abrahamson, Ross Boulanger, Colleen Bronner, Jason DeJong, Alejandro Martinez, and Katerina Ziotopoulou for always pushing me to be the best version of myself. All my professors made the transition to learning during a global pandemic as easy as possible and I truly appreciate their efforts.

Thank you to all the members in my cohort. I am especially thankful for James Heinz, Rachel Reardon, and Valerie Yanez, thank you for always being willing to meet up with me outside at Temple Coffee to get some writing done.

I want to thank my friends and family for their support throughout these past two years. Thank you to my friends: Caroline Christmas, Allie Evans and Rachell Campbell, Viktoria Prage, and Olivia Scott-Dahrouge for coming out to visit me and always being there for me. Thank you, Bailey Diaz and the whole Diaz family for always making me feel like family. Thank you to my grandparents and extended family for their continuous support throughout my studies. Thank you, Mom and Dad for your support in my pursuing my bachelor's and master's degrees and always letting me crash at your house whether the smoke from the wildfires was too thick, there was a heat wave, or there was a start of a global pandemic I always knew that I had a safe place I could go home to and work from. Thank you to Matthew for commuting from Davis to Folsom every day so that I could live close to campus and for always being supportive in my studies, even though it took up a good amount of our weekends. Thank you, Aaron, and Emmitt for motivating me to be a positive role model as your big sister. Finally, thank you to my puppy, Poppy, who brings me so much joy each day.

ABSTRACT

Numerous geotechnical applications such as pile installation or CPT exploration require large rigs to generate reaction forces for the penetration of geotechnical elements. These rigs can increase financial and environmental impacts and pose accessibility challenges to engineering projects. Bio-inspiration can be used to identify geometries of penetrometers to reduce the penetration resistances, which may enable the use smaller rigs that would reduce the related economic and environmental impacts of geotechnical activities. This research aims to identify the attributes of organisms that make them efficient burrowers and evaluate the application of these attributes for geotechnical engineering activities. Particularly, this work focuses on the attributes of penetrometer apex angle and geometric asymmetry. Evaluation of the bio-inspired penetrometer, in terms of the generated tip resistance, is accomplished by performing Discrete Element Method (DEM) simulations where each geometry is penetrated into a specimen contained in a calibration chamber. In this research, both shallow and deep penetration conditions are considered. Shallow penetration conditions are defined as penetration in an unconfined specimen at normalized depths ratios (Z/D, depth to probe diameter) smaller than 7, while deep penetration conditions are defined as penetration in a confined specimen subjected to a vertical stress of 100 kPa and a horizontal stress of 50 kPa. Results show that an apex angle close to that of a honeybee stinger, 30°, minimizes the tip penetration resistance for shallow penetration. Results additionally show that an apex angle of 15° reduce penetration resistance for deep penetration conditions. However, this reduction in penetration resistances at deep conditions was smaller than that achieved in shallow conditions. With DEM, it is possible to monitor the forces and position of each individual particle, thus allowing for close examination of the soil failure mechanisms generated by each tested probe geometry. The results show that

probes with small apex angles displace particles horizontally and create increases in horizontal stress at locations near the probe tip. In contrast, probes with large apex angles displace particles vertically down, creating an increase in vertical stresses below the probe tip. The asymmetric probes simulations showed no reduction of penetration resistance compared to their symmetric counterparts. The asymmetric tip may also contribute to an imbalance in the forces acting on the probe, which may cause the probe to not penetrate the substrate vertically. The mechanisms explored using DEM can also help develop an understanding for future improvements of probe geometry to achieve more efficient penetration during in-situ tests and construction activities.

TABLE OF CONTENTS

TABLE OF EQUATIONS, FIGURES, AND TABLES

1 INTRODUCTION

Numerous geotechnical activities require large rigs to mobilize reaction forces for the penetration of geotechnical elements such as CPTs or piles into the ground. The use of such rigs can increase project cost, reduce accessibility, and increase environmental impacts (Chen et al. 2021; 2020; Purdy et al. 2020). While previous studies have investigated the influence of the apex angle on penetration resistance generated by penetrometers with conical tips in dense and loose soils, these studies have not directly addressed the relationship between apex angle and penetration resistance in both deep and shallow penetration conditions. There is also a lack of consensus of the relationship between apex angle and penetration resistance among the previously conducted studies. In addition, the differences in the failure mechanisms within the soil developed by penetrometers with varying angle tips require further understanding. This study aims to isolate the effects of depth and geometry on penetration resistance for granular materials in order to increase the efficiency (i.e., force per unit length of penetration) of soil penetration processes.

1.1 RESEARCH OBJECTIVES

Bio-inspiration may help identify penetrometer geometries that can reduce penetration resistances, making it possible to use smaller rigs which would reduce the related economic and environmental impacts of geotechnical activities. This research identifies bio-inspired shapes that can prove as a guide to create geometries that reduce penetration resistance in granular materials,

then evaluates the potential of these geometries to reduce penetration resistance using Discrete Element Modeling (DEM) simulations.

Probes with symmetric conical tips with total apex angles of 15°, 30°, 45°, 60°, 90°, 120°, 150°, and 180° and probes asymmetric tips with half apex angles of 30° - 0°, 20° - 10°, and 60° - 0° were evaluated in the simulations. Figure 1 provides a schematic a probe with a symmetric 60° total apex angle tip, while an example of the asymmetric tip can be found in Figure 22. The penetration simulations were performed in vertically unconfined and confined specimens to simulate shallow and deep penetration conditions, respectively. In both cases there are rigid side walls and a base wall; additionally, there was gravity applied to the unconfined simulations, but no gravity was applied to the confined simulations. Figure 2 provides an example of the unconfined specimen and Figure 3 provides an example of the confined specimen.

The main hypothesis of this work is that the use of bio-inspired shapes or methods has the ability to reduce penetration resistance through altering the state of stresses of the soil around a probe during penetration. It is noted here that this work is part of a larger project; the DEM simulations presented here serve as a preliminary study to help identify promising tip geometries that will then be tested in the laboratory or field.

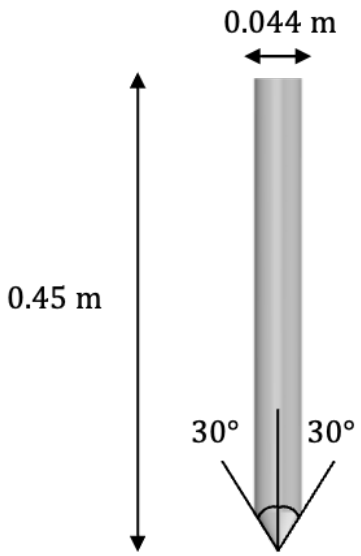

Figure 1. Schematic of probe with a 60° total apex angle tip

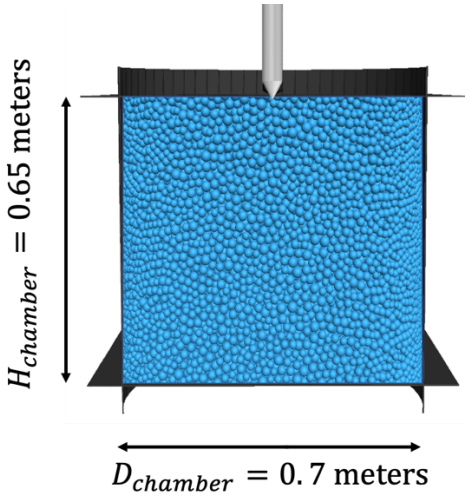

Figure 2. Schematic of unconfined specimen, note that a gravitational acceleration of 9.81 m/s^2 is included in this simulation

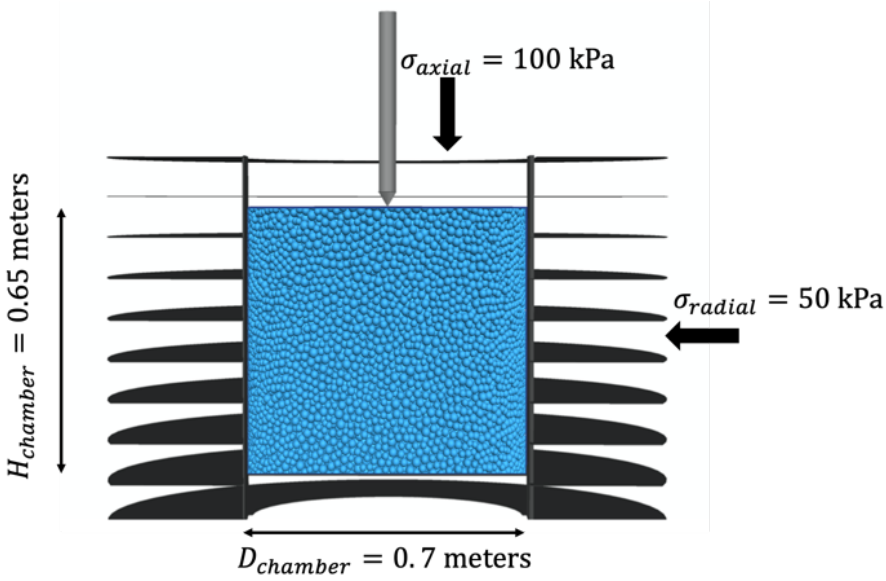

Figure 3. Schematic of confined specimen, note that no gravitational acceleration is included in this simulation

The layout of the chapters of the thesis is as follows:

Chapter 2 provides a Literature Review covering the following aspects: the bio-inspiration process, burrowing organisms, DEM cone penetration test simulations, relationship between apex angle and penetration resistance, and soil deformation processes for probe penetration.

Chapter 3 provides a description of the testing plan, simulation configuration and parameters, model verification, and testing parameters.

Chapter 4 presents the results of the simulation in the global, meso, and micro scales.

Chapter 5 concludes the research findings and provides recommendations for future work.

2 LITERATURE REVIEW

Due to the variety of topics that are integrated in this literature review, it is sub-divided into the following five parts:

1. Bio-inspiration process
2. Burrowing organisms
3. DEM Cone Penetration Test (CPT) simulations
4. Relationship between apex angle and penetration resistance
5. Soil Deformation Patterns

2.1 BIO-INSPIRATION PROCESS

This part of the literature review focuses on bio-inspired design processes and their use towards geotechnical engineering applications. Bio-inspiration is a concept developed to help transfer concepts from the biological domain to the engineering domain (Martinez et al. 2021).

The bio-inspired design process is commonly described by the problem-driven and solution-driven approaches (Helms et al. 2009). The problem-driven and solution-driven approaches are shown schematically in Figure 4 and Figure 5, respectively. The solution-driven approach is typically used by individuals familiar with organisms and their behaviors. The solution-driven approach consists of three main steps: solution abstraction, retrievial, and maping and transfer. The problem-driven approach is typically used by researchers familiar with the engineering domain and consists of three main steps: problem abstraction, retrieval, and mapping and transfer (Helms et al. 2009; DeJong et al. 2017). The “Problem-Driven Approach” will be the focus of this literature review and is discussed in more detail below, as described by DeJong et al. (2017).

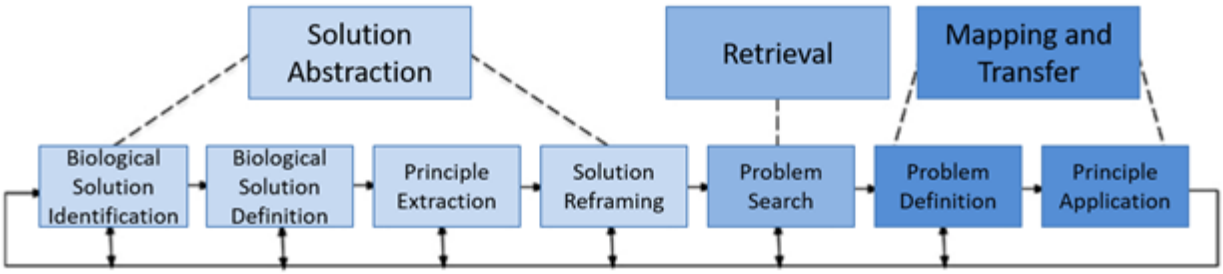

Figure 4. Solution driven approach (DeJong et al., 2017)

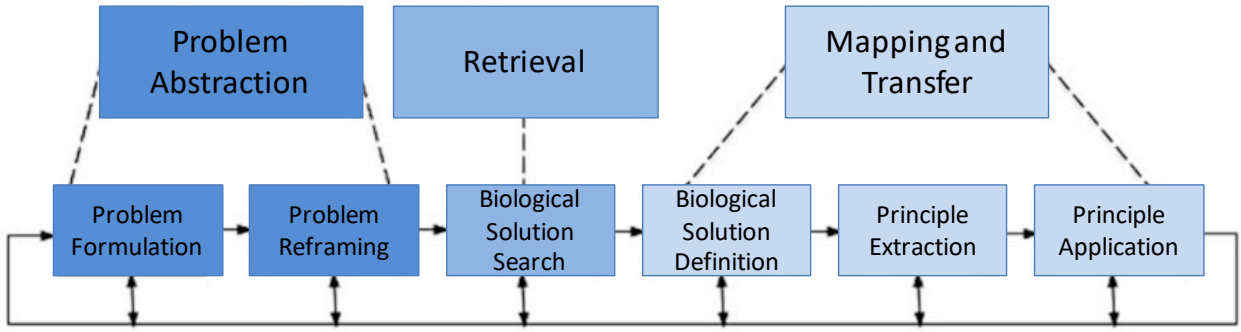

Figure 5. Problem-driven approach (DeJong et al. 2017; adapeted from Helms et al. 2009)

2.1.1 PROBLEM-DRIVEN APPROACH

The problem-driven approach first identifies an engineering problem that needs to be solved, then searches, defines, extracts, and applies a biological solution to solve that problem. A problem-driven approach is typically used by engineers because they are familiar with the problem and constraints. Within the problem formulation step, an engineering problem is identified and clearly defined in terms of the constraints and design expectations. Next, in the problem reframing step, a problem is broadly reframed through removing domain-specific terms; this allows for an easier search for a biological analog. After the problem reframing is complete the biological solution search is conducted, which is a research phase dedicated to identifying biological solutions that meet the conditions listed in the reframed problem. After the biological solution search is complete the biological solution is defined, a biological solution is defined in "terms of descriptions of the forms, behaviors, and principles" (Mak and Shu 2004). An example

of form, behavior, and principle for adaptations by plant root systems for generating anchorage are shown in Figure 6. Forms are physical structures that directly mimic the desired attribute of the organism, behaviors reference the process without the direct translation of the physical shapes, and principles describe the underlying reason for the behavior or adaptation. After the biological solution is defined in terms of forms, behaviors, and principles the principle extraction phase begins, where the solution is described with as little reference to environmental constraints and specific structures to prevent the transferring of features that are "too domain specific" (DeJong et al. 2017).

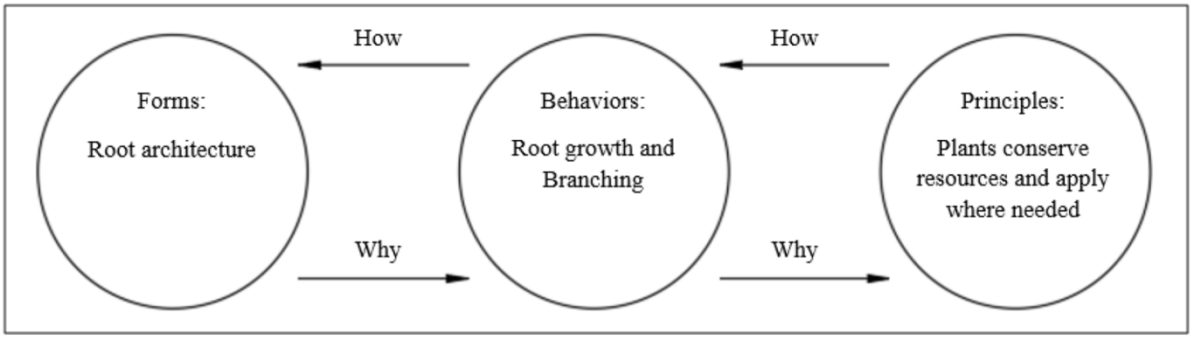

Figure 6. Example of abstraction of strategies employed by plant root systems to generate anchorage in terms of forms, behaviors, and principles (DeJong et al. 2017;adapted from Mak & Shu 2004)

The last step is the principle application phase, similar to what its name suggests, the principle that was previously extracted is applied in an engineering context.

Application of Bio-Inspiration in Geotechnical Engineering

Even with differences in spatial and temporal scales, bio-inspiration has been proved a useful tool in geotechnical engineering (Martinez et al. 2021). Previous research has looked into the use bio-inspiration to generate solutions to applications for soil penetration and excavation, foundation and anchoring elements, ground improvement, materials, slope stabilization and

erosion mitigation, earth moving and manipulation, renewable energy generation and regulation, transport of water and contaminants, filtration, and locomotion and mobility (Martinez et al. 2021). An example of current bioinspired research within geotechnical engineering is investigating the use of directionally dependent snakeskin-like materials for a variety of purposes including deep foundations, soil anchors, and landfill liner systems ((Martinez et al. 2021; O'Hara and Martinez 2020). The frictional anisotropy of the snake skin allows for the greater mobilization of shear resistance during the installation process or service life, depending on the directionality of the asperities (Martinez et al. 2021). An additional bio-inspiration study by Chen et al. (2020) and Chen et al. (2021) explores the potential of self-penetration of a CPT-like probe through using expanding anchors similar to that which an earthworm might use. Through the use of expanding anchors, CPT-like probes are able to significantly reduce penetration resistance (Chen et al. 2020; 2021).

2.2 BURROWING ORGANISMS

Through the processes of evolution and natural selection, many organisms have developed strategies to efficiently burrow in different soil conditions and to penetrate different substrates. These strategies serve as the biological solutions in the bio-inspired design process. The evolutionary developments to efficiently burrow vary by organism. This part of the literature review focuses on describing strategies used by burrowing organisms: shapes and motion sequences. Although these strategies are categorized separately, it is noted here that frequently organisms use more than one strategy simultaneously.

Many organisms that penetrate substrates take on many different shapes, which may help them in the penetration process. The use of a small apex angle, asymmetry, and barbs are all strategies

employed by organisms such as the worker honeybee (*Apis cerana cerana)*, parasitic wasp (*Diachasmimorpha longicaudata)*, and forest mosquito (*Aedes albopictus*) (Cerkvenik et al. 2017; Kong and Wu 2009; Ling et al. 2016). Both the worker honeybee stinger and forest mosquito fascicle's designs have been investigated for potential use in transdermal drug delivery. It is believed that the small apex angle of the worker bee stinger, which is approximately 33 °, as well as the barbs on the lancelets contribute to a relatively small a penetration resistance of the honey bee stinger into human skin and other biological substrates; because of the design of the honey bee stinger, the penetration of the stinger is relatively painless and vibration-free (Ling et al. 2016). Figure 16 displays a scanning electron microscope (SEM) image of a honeybee stinger. The use of a forest mosquito (*Aedes albopictus*) fascicle has been shown to produce penetration resistances at least three orders of magnitude smaller than traditional microneedles used for transdermal drug delivery (Kong and Wu 2009).

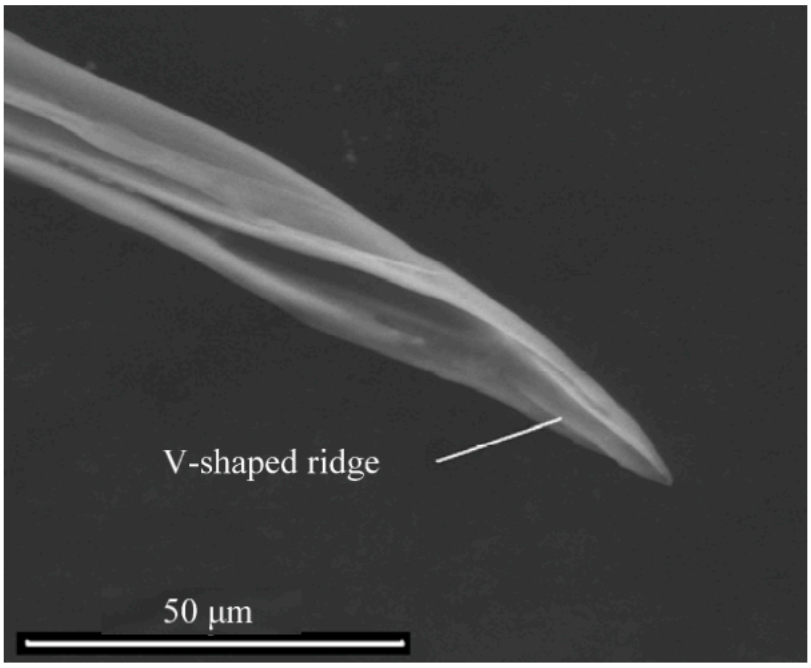

Figure 7. SEM image of a mosquito stinger labrum in lateral view (Kong and Wu 2009)

The parasitic wasp, which uses its ovipositor to insert eggs into hosts, has the ability to penetrate through a variety of substrate surfaces, including wood, fruit tissue, and other insects (Cerkvenik et al. 2017). In a soft substrate the parasitic wasp ovipositor is directly inserted into the substrate without the need for reciprocal motion; however, when a stiff substrate is encountered a reciprocal motion is used (Cerkvenik et al. 2017). The strategy of reciprocal motion is shown schematically in Figure 8. The reciprocal motion is a “sawing” type behavior between the two sides of the wasp ovipositor.

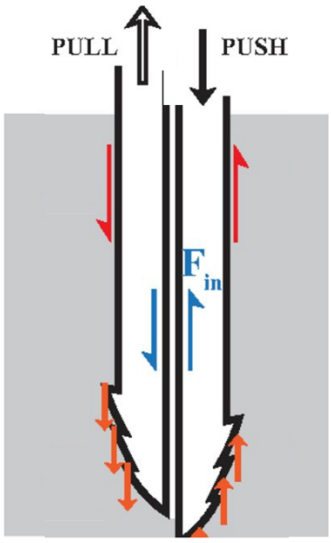

Figure 8. Schematic of reciprocal motion used by the parasitic wasp (adapted from Cerkvenik et al. 2017)

The Pacific sand lance (*Ammodytes personatus*) has the ability to burrow into a variety of soil types; the streamlined shape of the fish skeleton may provide insight into how the fish is able to penetrate a variety of substrates. (Bizzarro et al. 2016; Gidmark et al. 2011; Chen et al. 2021). Gidmark et al., 2011 evaluated the burrowing of the Pacific sand lance using X-ray video. It was hypothesized that the vibrations that the Pacific sand lance fish during penetration fluidized the sand surrounding the fish, however, no fluidization was seen near the particles surrounding the fish in the X-ray video. The X-ray video shows the fish using its pointed nose to push through the sand, while it uses its body to push against the sand causing the sand flow around the body of the Pacific sand lance (Bizzarro et al., 2016).The Pacific sand lance (*Ammodytes personatus*) has the ability to burrow into a variety of soil types; the streamlined shape of the fish skeleton may provide insight into how the fish is able to penetrate a variety of substrates. (Bizzarro et al. 2016; Gidmark et al. 2011; Chen et al. 2021). Gidmark et al., 2011 evaluated the burrowing of the Pacific sand lance using X-ray video. It was thought that the vibrations that the Pacific sand lance fish during penetration fluidized the sand surrounding the fish, however no fluidization was

seen near the particles surrounding the fish in the X-ray video. The X-ray video shows the fish using its pointed nose to push through the sand, while it uses its body to push against the sand causing the sand flow around the body of the Pacific sand lance (Bizzarro et al. 2016).

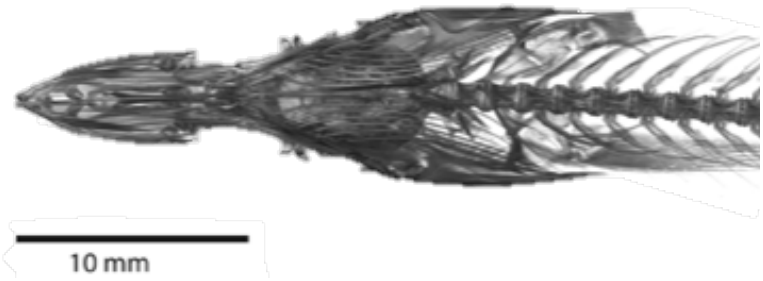

Figure 9. Pacific sand lance fish skeleton (Bizzarro et al. 2016)

A study performed by Mishra et. al (2018) evaluated the penetration force for a variety of tip shapes including: cylindrical, elliptical, parabolic, conical, and "root-like". The "root-like" tip profile was extracted using image processing and curve fitting techniques on a Zea Mays root, or corn root, then the extracted profile was fabricated using a 3D printer. The tip that produced the smallest amount of penetration force in the laboratory experiments of sandy loam was that of the "root-like" tip (Mishra et al. 2018)

As previously discussed for the parasitic wasp's adaptation, organisms also use motions to assist in the penetration of substrates. Another example of using motion to assist in penetration is the use of open mode discontinuity. An open mode discontinuity consists of the displacement of soil

grains due to the invasion of an immiscible fluid or an invading object, such as a plant root. An open mode discontinuity mainly involves lateral loading of the soil which reduces the normal stresses ahead of the object, thus reducing the penetration resistance (Shin and Santamarina 2011). Open mode discontinuities grow because of increased local porosity ahead of the tip or due to lower normal effective stresses ahead of the tip (Shin and Santamarina 2011). Both earthworms (*Eisenia Fetida*) and Atlantic razor clams (*Ensis directus*) use strategies that resemble open mode discontinuities to decrease stresses at the penetrating tip of the organism, allowing for burrowing with decreased energy use or force (Chen et al. 2020; Winter et al. 2014). For example, the Atlantic razor clam can dig up to 70 centimeters through the use of open mode discontinuities and local fluidization, thereby reducing burrowing drag. The clam contracts its valves to fail and fluidize the surrounding soil. This local fluidization allows the Atlantic razor clam to reduce the energy required to burrow by approximately 10 times (Winter et al. 2014). Additionally, Winter et al. concluded that this method is not limited to the small scale of the Atlantic razor clam. The burrowing method used by the Atlantic razor clam proved effective even when a large-scale prototype was tested (Winter et al. 2014).

One method that earth and marine worms use to reduce tip resistance while burrowing is radial expansion of a body portion near the tip. This radially-expanding body section generates a reduction in tip resistance through an open mode discontinuity mechanism and it also provides an anchor to further penetrate the soil (Chen et al. 2020; Dorgan 2015). Studies performed on the implementation of worm- and clam-inspired geotechnical devices have shown the potential to reduce penetration resistance (Chen et al. 2020; Cortes and John 2018; Huang et al. 2020; Tao, Huang, and Tang 2020). Plant roots such as the corn (*Zea mays*) root use circumnutation, a helictical movement to penetrate the soil. Through a comparison of penetration resistance with

and without root-inspired circumnutations, a reduction up to 33% of work was measured through laboratory testing using a robotic arm to penetrate an artificial probe into the substrate (Del Dottore et al. 2017; 2016). As previously discussed for the parasitic wasp's adaptation, organisms also use motions to assist in the penetration of substrates. Another example of using motion to assist in penetration is the use of open mode discontinuity. An open mode discontinuity consists of the displacement of soil grains due to the invasion of an immiscible fluid or an invading object, such as a plant root. An open mode discontinuity mainly involves lateral loading of the soil which produces a reduction in the normal stresses ahead of the object, thus reducing the penetration resistance (Shin and Santamarina 2011). Open mode discontinuities are able to grow because of increased local porosity ahead of the tip or due to lower normal effective stresses ahead of the tip (Shin and Santamarina 2011). Both earthworms (*Eisenia Fetida*) and Atlantic razor clams (*Ensis directus*) use strategies that resemble open mode discontinuities to decrease stresses at the penetrating tip of the organism, allowing for burrowing with decreased energy use or force (Chen et al. 2020; Winter et al. 2014). For example, the Atlantic razor clam can dig up to 70 centimeters through the use of open mode discontinuities and local fluidization, thereby reducing burrowing drag. The clam contracts its valves to fail and fluidize the surrounding soil; this local fluidization allows the Atlantic razor clam to reduce the energy required to burrow by approximately 10 times (Winter et al. 2014). Additionally, Winter et al. (2014) concluded that the use of this method is not limited to the small scale of the Atlantic razor clam. The burrowing method used by the Atlantic razor clam proved effective even when a large-scale prototype was tested (Winter et al. 2014). One method that earth and marine worms use to reduce tip resistance while burrowing is radial expansion of a body portion near the tip. This radially-expanding body section generates a reduction in tip resistance through an open

mode discontinuity mechanism and it also provides an anchor to further penetrate the soil (Chen et al. 2020; Dorgan 2015). Studies done on the implementation of worm- and clam-inspired geotechnical devices have shown the potential to reduce penetration resistance (Chen et al. 2020; Cortes and John 2018; Huang et al. 2020; Tao, Huang, and Tang 2020). Plant roots such as the corn (*Zea mays*) root use circumnutation, a helictical movement to penetrate the soil. Through a comparison of penetration resistance with and without root-inspired circumnutations, a reduction up to 33% of work was measured through laboratory testing using a robotic arm to penetrate an artificial probe into the substrate (Del Dottore et al. 2017; 2016). Figure 10 and Figure 11 display plots illustrating the force and energy, respectively, used versus depth comparing straight penetration to circumnutation.

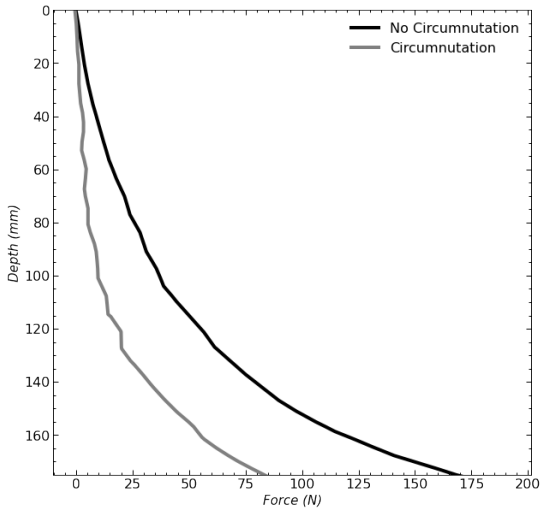

Figure 10. Plot of penetration resistance with depth for penetration with and without root-inspired circumnutations (adapted from: Del Dottore et al. 2017)

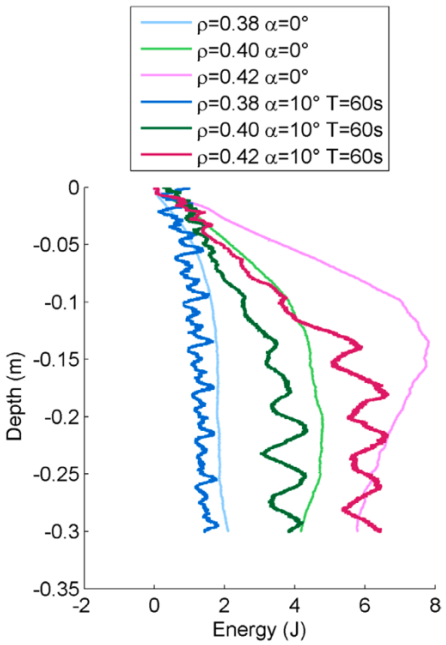

Figure 11. Instantaneous energies of using straight penetration and circumnutations, ρ indicates soil density, while α indicates the amplitude of the circumnutations, T indicates the period of rotation (Del Dottore et al. 2016)

2.3 DISCRETE ELEMENT MODELING OF CONE PENETRATION TESTS

Discrete Element Modeling is a numerical method first developed for soil mechanics applications in the 1970's by Peter A. Cundall and Otto D. L. Strack. Like its name suggests, DEM models each element discretely or individually (Cundall and Strack 1979). For a geotechnical engineer's use of DEM, these discrete elements represent soil particles. These discrete elements can be assigned physical properties including density, size, stiffness and friction coefficients (O'Sullivan 2011). A thorough description of the DEM method can be found in Cundall and Strack (1979) and O'Sullivan (2011).

DEM is a useful tool in engineering and scientific analysis to understand the fundamental aspects of the behavior of granular materials and their interactions with other objects. Examples of problems that have been investigated with DEM include: railroad ballasts, triaxial shearing, and retaining walls (Chang and Chao 1994; Kim and Park 2020; Qian et al. 2013).

In 2011, Arroyo et al. (2011) performed one of the first 3D DEM-based CPT simulations (Arroyo et al. 2011). A virtual calibration chamber (VCC) was created to find an alternative to the expensive and time-intensive calibration chamber testing that is performed in the laboratory to create empirical correlations for CPTs in sand. Arroyo et al. (2011) modeled Ticino sand and simulated cone penetration tests, and after the cone tip resistance values were corrected for cone and chamber size effects the simulation results showed good agreement with the previous experimental results. Arroyo et al. (2011) concluded that there was quantitative agreement between the numerical and physical experiments despite simplifications in the particle size distribution, particle behavior, and all other aspects of model construction that were used to allow the simulation to be computationally feasible (Arroyo et al. 2011).

Following the work of Arroyo et al. (2011) parametric studies have been performed to evaluate the influence modeling parameters and configurations can have on penetration resistance results for virtual CPT testing (Butlanska et al. 2014; Khosravi, Martinez, and DeJong 2020). Khosravi et al. (2020) examined the effect that nine parameters and configurations had on the behavior of cone resistance, q_c, and sleeve friction measurements, f_s. The nine parameters and configurations include stress anisotropy conditions, particle scaling factor, initial void ratio, chamber diameter, boundary conditions, penetration rate, interparticle friction coefficient, rolling resistance friction coefficient, and probe-ball friction coefficient. A soil behavior type chart in Figure 12 displays a summary of the findings in Khosravi et al. , where Q is the normalized tip resistance and F is the normalized friction ratio as defined in (Robertson 2016). As the void ratio of the specimens

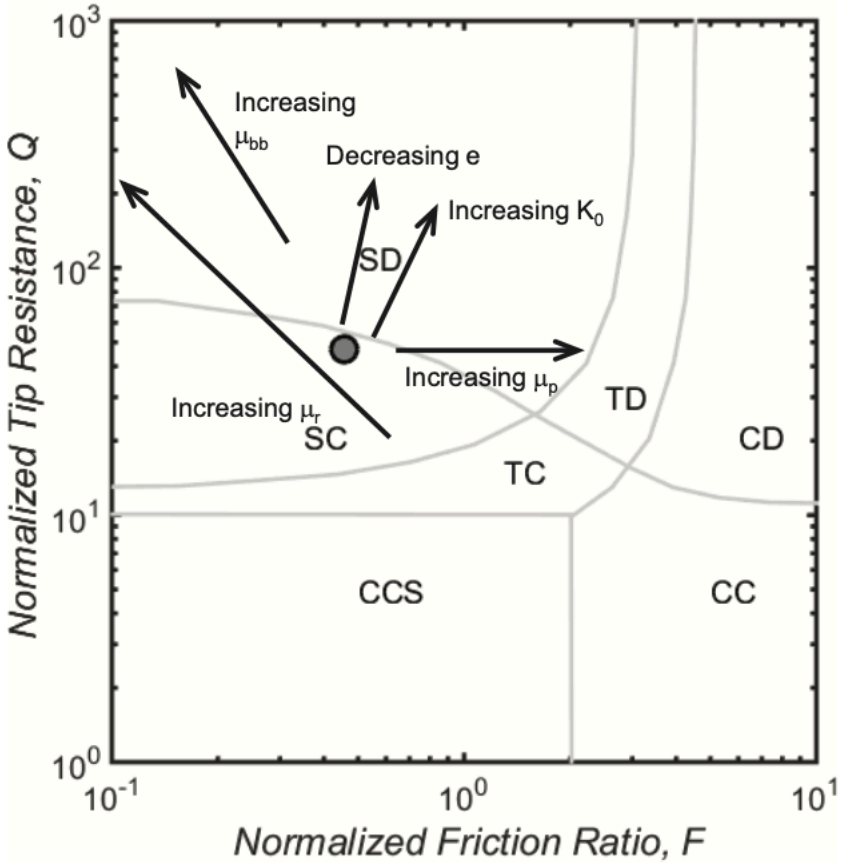

Figure 12. SBT chart DEM parameter trends(Khosravi, Martinez, and DeJong 2020)

decrease, the resistive forces tend to increase. As the particle chamber diameter decreased, a decrease in q_c and f_s was observed. Stress boundary conditions, such as isotropic and anisotropic ($K_0 = 0.5$, where $K_0 = \sigma'_h / \sigma'_v$) were seen to have a significant effect on penetration resistance, with tests on isotropic samples showing greater penetration resistances. Penetration resistance was compared for specimens prepared with interparticle friction coefficients of 0.2, 0.4, and 0.6, which directly influences the friction angle of the granular assemblies. The effect of the interparticle friction coefficient on the penetration resistance was significant, with increases in friction coefficient from 0.2 to 0.4 having a greater effect on penetration resistance than subsequent increases from 0.4 to 0.6. The authors also performed simulations with rolling resistance coefficients of 0.0, 0.175, and 0.350. The rolling resistance coefficient captures the effects of particle angularity on the granular assembly friction angle, which also had a significant effect on penetration resistance. As the rolling resistance coefficient was increased, so did the q_c. The rolling resistance coefficient had a minimal impact on f_s, only showing a slight increase in f_s with an increasing rolling resistance coefficient. As the probe-particle friction coefficient was increased so, did the value of f_s. However, increases in probe-particle friction coefficient had a minimal effect on the q_c value. (Khosravi, Martinez, and DeJong 2020).

If particle sizes and shapes corresponding directly to sandy soils were to be used in DEM simulations, they would be extremely computationally intensive (O'Sullivan 2011). To decrease computational time, two main approaches are typically taken in large-scale DEM simulations: up-scaling of particle sizes and using spherical particles while assigning rolling resistance coefficients to mimic particle angularity effects. While decreasing simulation time is a clear advantage to scaling the particle sizes, there is also a side effect of increasing the fluctuation of responses and slight increases in tip resistance (Butlanska et al. 2014; Khosravi, Martinez, and

DeJong 2020). Typical probe to particle size ratios , d_{probe}/d_{50}, where d_{probe} is the probe diameter and d_{50} is the mean particle size, range from values of about 2.6 to 3 for DEM penetration simulations (Arroyo et al. 2011; Butlanska et al. 2014; Chen et al. 2020). Table 1 provides values employed by several penetration investigations in DEM. In many instances, spherical particles are used to simulate soil particles in DEM, with their angularity and friction accounted for by the employing the rolling friction coefficient contact model (Ai et al. 2011; O'Sullivan 2011; Wensrich and Katterfeld 2012).

It is noted here that although Sturm (2019) evaluated that a D_{probe}/D_{50} ratio of 6 and larger results in no influence of the tip resistance in experimental results, Khosravi, Martinez, and DeJong (2020) evaluated that for DEM simulations if the D_{probe}/D_{50} ratio is larger than 2 the only identifiable difference in q_c is larger oscillations.

Table 2 lists common parameters used in previous DEM simulations. Unlisted parameters do not necessarily indicate that the parameter value was set to zero for the simulation, rather the value was not listed or discussed in the corresponding paper. The parameters selected define the contact behavior of soil particles in DEM. These parameters can include: rolling resistance coefficient, damping coefficient, particle density, probe-particle friction coefficient, the chamber-particle coefficient, particle normal stiffness, particle shear stiffness, and grain size distribution.

Some studies defined the normal and shear stiffnesses as ratios (Arroyo et al. 2011; Butlanska et al. 2014; Chen et al. 2020; Kuei 2019), while others chose to represent the normal and shear stiffnesses as constant values (Khosravi, Martinez, and DeJong 2020; Mcdowell, Falagush, and Yu 2012).

The ability to model CPT-type penetration through DEM has been used for many preliminary studies, for example Chen et al. (2021) evaluated an anchoring system in granular materials. Through DEM modeling it was possible to closely examine the soil behavior around the probe. From this examination it was determined that the stresses below the tip of the probe decreased after anchor expansion, contributing to a decrease in penetration resistance (Chen, Martinez, and DeJong 2022).

Table 1. Comparison of chamber diameter, probe diameter, and mean particle size.

Study	Chamber Diameter (mm)	Probe Diameter (mm)	Mean Particle Size, D_{50} (mm)	$D_{chamber}/D_{probe}$	D_{probe}/D_{50}
(Chen et al. 2021)	700	44	14.4	15.9	3.1
(M. O. Ciantia, O'Sullivan, and Jardine 2019)	432	36	8.19	12	4.4
(Zhang et al. 2019)	760	50.8	16.6	15	3.1
(Sadek, Tekeste, and Naderi 2017)	150	25	5	6	5
(Zeng and Chen 2016)	40	2.75	2	14.5	1.4
(Matteo Oryem Ciantia et al. 2016)	760	72.1	22	10.5	3.3
(Butlanska et al. 2014)	1200	71.2	26.5	16.9	2.7
(Arroyo et al. 2011)	1200	71.2	26.5	16.9	2.7

Table 2. DEM simulation parameter comparison.

Study	μ_{bb}	μ_r	μ_{bw}	μ_p	β	Includes Rolling Resistance in Contact Law?	k_n, (MN/m)	k_s, (MN/m)	$\frac{k_n}{k_s}$	e_o
Chen et al. 2021	0.4	0.4	0.1	0.3	0	Yes	1.44*	0.96*	1.5	0.61
Khosravi et al., 2019	0.4	0.175	0.1	0.2	0.05	Yes	305	152.5	2	varies
Butlanska et al., 2012	0.35		0	0.35	0.05	No	7.95*	1.9875*	4	
Arroyo et al., 2011	0.35				0.05	No	7.95*	1.9875*	4	0.58
McDowell et al., 2012			0.5	0.5		No	0.05	0.05	1	0.56
Jiang et al., 2018					0.2	No	0.04*	0.04*	1	0.63
Yan and Dong, 2011			0	0.5	0.7	No	0.1*	0.1*	1	0.76
Kuei, 2019	0.4	0.4	0.1		0.6	Yes	1.44*	0.96*	1.5	

Note: μ_{bb} = interparticle friction coefficient or sliding coefficient, μ_r = rolling resistance coefficient, μ_{bw} = ball-wall friction coefficient, μ_p = probe-particle friction coefficient, β = damping coefficient, k_n = normal stiffness, k_s = shear stiffness, $\frac{k_n}{k_s}$ = normal to shear stiffness ratio, e_o = initial void ratio

** indicates stiffness values for a particle with a diameter equal to D_{50}*

2.4 RELATIONSHIP BETWEEN PENETRATION RESISTANCE VERSUS APEX ANGLE

The thought of altering probe or pile tip geometry to reduce penetration resistance is not a new idea in geotechnical engineering; many studies have examined the relationship between probe apex angle and penetration resistance. A comparative analysis was conducted on five previous studies that attempted to evaluate the relationship between apex angle and penetration resistance (Browning 2005; Lin and Wu 2012; Lobo-Guerrero and Vallejo 2007; Tovar-Valencia et al. 2021; Wu and Yamamoto 2014). There is a difficulty in directly comparing the conclusions of these studies because the methods and parameters are different between the studies. The

parameters for each study are presented in Table 3. In Figure 13, results were normalized by the penetration resistance measurements taken for the 60° apex angle for ease of comparison.

2.4.1 BROWINING, (2005)

Browning (2005) evaluated five different apex angles (50, 60, 75, 90, 120°) in both the laboratory and field. From the laboratory testing, Browning (2005) concluded that the testing results indicated a parabolic shape trend with decreasing penetration resistance from 50 to 75 ° then increasing from 75 to 120 °, although Browning (2005) stated that it is believed chamber boundary effects were contributing to the higher than predicted penetration resistances. From the field testing Browning (2005) concluded that the obtuse angle tips are more advantageous in dense soils compared to the standard 60° tip used for a CPT which is thought to be attributed to the smaller volume of effected soil (Browning 2005).

2.4.2 LOBO-GUERRERO AND VALLEJO (2007)

Lobo-Guerrero and Vallejo (2007) examined the effect that pile tip shape has on the penetration resistance in crushable granular materials using 2D DEM simulations. Lobo-Guerrero and Vallejo (2007) concluded that the shape of the pile had a significant influence on penetration resistance and particle crushing. The highest penetration resistance was recorded for a flat tip (180°) pile which also saw the highest amount of particle crushing. This high amount of crushing is likely due to the concentration of stresses around the tip which causes breakage in weak granular materials (Lobo-Guerrero and Vallejo 2007).

2.4.3 LIN AND WU (2012)

Lin and Wu (2012) examined the dependence of penetration resistance on the penetrometer geometry for miniature penetrometers through using 3D DEM models. Lin and Wu (2012) concluded that for cone apex angles less than 20° the penetration resistance decreases as cone half-angles increase, then for a cone apex angles greater than 20° the penetration resistance increases. The decreasing contact area as the apex angle increases to 20° causes the cone resistance to decrease; however, at greater apex angles the increase in soil penetration resistance overtakes this trend (Lin and Wu 2012).

2.4.4 WU AND YAMAMOTO (2014)

Wu and Yamamoto investigated the effects pile tip shape can have on the soil behavior around underreamed piles. Finite Element Method (FEM) was used with a constitutive model for sand with particle crushing and joint elements. Results from this study demonstrate that soil experiences a smaller distributed area of stresses as the pile tip gets sharper; this smaller distributed area translates to smaller penetration resistances (Wu and Yamamoto 2014).

2.4.4 TOVAR-VALENCIA ET AL. (2021)

Tovar-Valencia et al. (2021) performed laboratory penetration experiments in a half-cylindrical calibration chamber on piles with conical (60° apex angle) and flat base (180° apex angle), where the penetration resistances and displacement and strain fields of these piles were examined. Results of the experiment determined that base resistance, displacement, and strain were dependent on the shape of the pile. In dense sand, the conical base pile had a 44% percent reduction in penetration resistance compared to that of the flat-base (180 °) pile base. It was

found that the magnitude of the radial and volumetric strains at the interface of the soil and pile is 30% - 40% greater at the corner of the flat-base compared to the conical base pile. This difference in radial and volumetric strain is thought to be the driving force for the difference in penetration resistance between the pile shapes (Tovar-Valencia et al. 2021).

2.4.5 DISCUSSION ON LITERATURE TRENDS

Figure 13 summarizes the trends seen in Browning (2005), Wu and Yamamoto (2014), Lin and Wu (2012), Lobo Guerrero and Vallejo (2007), and Tovar-Valencia (2021). Laboratory and field data from Browning (2005) summarizes tip resistance versus apex angle as a U-shape relationship with penetration resistance initially decreasing until around 90°, then increasing with increasing apex angles. DEM data from Lin and Wu (2012) displays a slight decrease in penetration resistance for apex angles less than 20°, then an increase in penetration resistance with increasing apex angle after. Results from Wu and Yamamoto (2014), Lobo Guerrero and Vallejo (2007), and Tovar-Valencia (2021) display a similar trend of increasing penetration resistance with probe apex angle. Additionally, the data from Tovar-Valencia in general, indicates that as relative embedment depth increases, the increase in normalized penetration resistance is smaller. In addition, the increase in penetration resistance with increasing apex angle appears to be greater in the denser sand. These comparisons highlight that although there has been a variety of experiments conducted which attempt to relate apex angle and penetration resistance, there is no consensus on the relationship. In addition, most studies focus on a relatively small range of apex angles, making it challenging to determine a trend for an entire range of possible apex angles given all other parameters are held constant.

Table 3. Apex angle literature review

Study	Method	Probe Diameter (cm)	Soil Type	Grain Size Distribution	Grain Size, mean (mm)	Density	Stress Type	Embedment (Normalized by Probe Diameter)	Surcharge
Browning (2005)	Lab	3.00	playground sand	Cu = 2.18 Cc = 0.85	0.40		Tip	0.60	
								1.00	
	Field	3.66	dense soil (values averaged over many sites)			Dense (Dr>66%)			
Lin and Wu (2012)	DEM (3D)	0.15	sandy loam over red clay				Tip		
Wu and Yamamoto (2014)	FEM combined w/ mixed incremental method	0.54 (also unique shape)	Toyoura Sand	Cu =1.21	0.20	Dense (Dr=90%)	Bearing	1.00	200 kPa
Lobo Guerrero and Vallejo (2007)	DEM (2D)	3.00	crushable sand		3.00		Tip	15.00	
Tovar-Valencia et al. (2021)	Lab	3.18	poorly graded, SP silica sand			Dense (Dr=90%)	Tip	0.05	
						Dense (Dr=90%)		0.10	
						Dense (Dr=90%)		1.00	
						Dense (Dr=90%)		2.00	
						Medium Dense (Dr=65%)		0.05	
						Medium Dense (Dr=65%)		0.10	
						Medium Dense (Dr=65%)		1.00	
						Medium Dense (Dr=65%)		2.00	

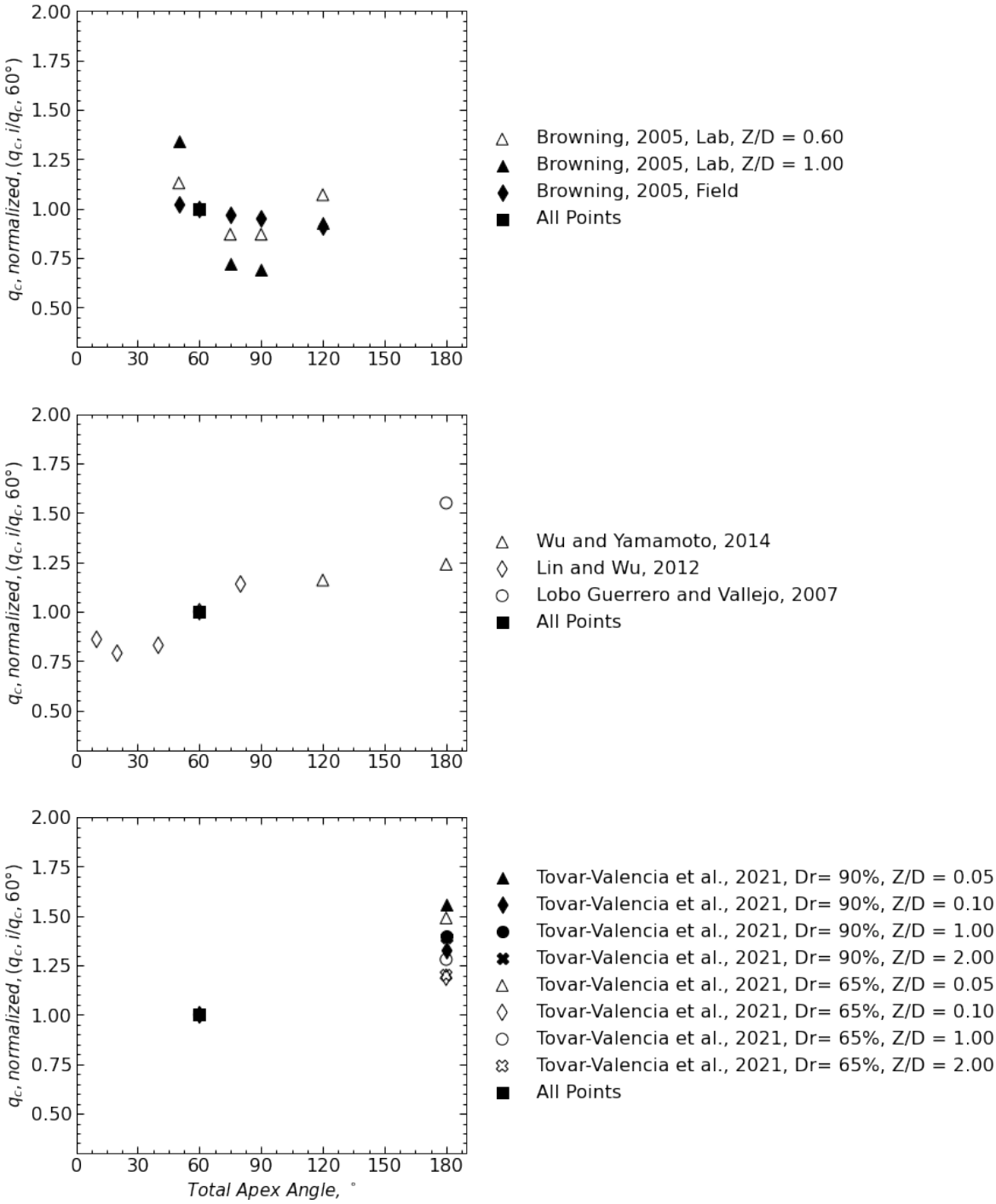

Figure 13. Normalized penetration resistance, $q_{c,normalized}$ ($q_{c,i}/q_{c,60°}$) versus apex angle, "All Points" indicates the normalized penetration resistance value for all data points shown in the plot's legend

2.5 SOIL DEFORMATION PATTERNS

Previous research has aimed to identify the interactions between soils and penetrometers. One method used to determine soil deformation patterns is image analysis which can aid in evaluating soil movements and strains over time. Figure 14 shows the soil deformation of a clay over time for a cone and a wedge. Through using soil imaging, it can be seen that the deformation of soil is considerably lower for the wedge compared to the cone probe tip.

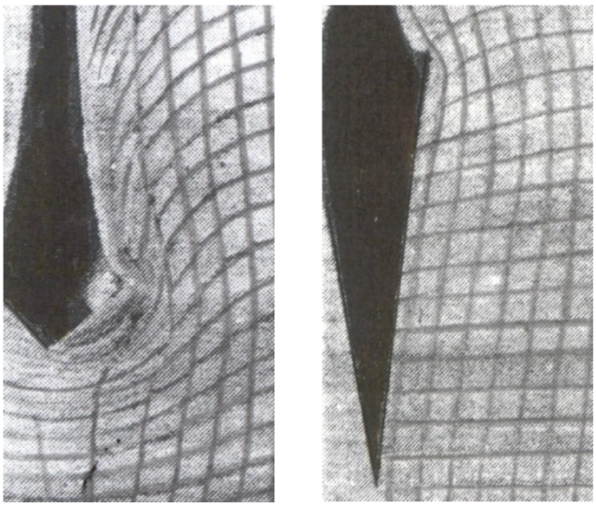

Figure 14. Soil Deformation of a cone (left) and a wedge (right) (Baligh and Scott 1975; Marchetti et al. 2001)

Similarly, Kobayashi & Fukagawa (2003), used X-ray radiography to evaluate the deformation of sand beneith tips with three different apex angles: 30°, 60°, and 180°. From the imaging results Kobayashi and Fukagawa concluded that the soil deformation of the 60° were somewhat smaller than for the 180° tip, thus implying former disturbs a smaller zone of soil around the penetrometer. Additionally, Kobayashi and Fukagawa (2003) concluded that this behavior is likely due to a blub-shaped soil failure beneath the probe, which, is more pronounced for more bluntly shaped tips, as shown in Figure 15. The soil deformations around the probe with an apex

angle of 30° were smallest. For this probe, no blub-shaped failure was formed (Kobayashi and Fukagawa 2003).

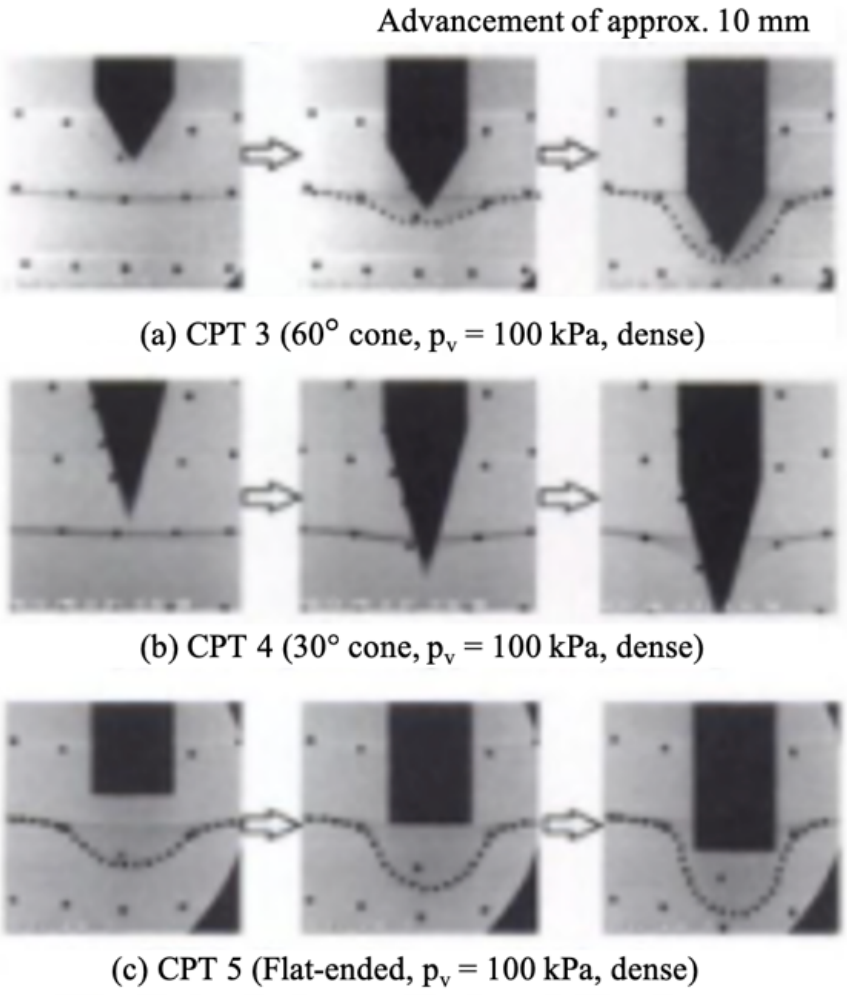

Figure 15. Soil deformation beneath probes of varying apex angles in dense sand (Kobayashi and Fukagawa 2003).
Soil deformation beneath probes of varying apex angles in dense sand (Kobayashi and Fukagawa 2003)

3 METHODS

3.1 BIO-INSPIRATION

As stated by DeJong et al. (2017), it should be acknowledged that "an assumption of inherent superiority of a biological analog in direct comparison to an existing engineered system is neither necessary nor required in bio-inspired design; the performance requirements and environmental constraints differ between the biological analog and the engineering design problem". For this research, the bio-inspired design process was used to help identify potential methods and geometries that should be evaluated for reduction of penetration resistance in soils. Although the environmental constraints between the biological analogs and the geotechnical application are not the same in the biological and engineering applications, the process was used to help generate ideas. Since the purpose of this research is to advance geotechnical engineering applications, a problem-driven approach was used. A problem-driven approach is often preferred when an engineering issue is first identified, then biological solutions are sought out to help achieve the goals set forward in the problem (DeJong et al. 2017).

The goal of this research is to identify and evaluate different geometries and methods to reduce penetration resistance in soils; particularly, this project focuses on altering apex angle and probe tip symmetry effects penetration resistance. The biological solutions that were evaluated to derive inspiration for reducing apex angle and altering probe symmetry are further discussed in the proceeding sections of this chapter.

3.1.1 PROBLEM ABSTRACTION

Problem Formulation

The engineering issue identified for this research is the need for reduction of penetration resistance in in-situ testing and construction applications. Examples of applications for these new probe geometries could prove useful in for performing cone penetration tests or other invasive in-situ tests or installing piles. Any geotechnical application in which a geotechnical element is penetrated into the soil, which can be at shallow or deep depths, could be benefitted by reductions in penetration resistance. Constraints for the current designs include designing a probe that would be compatible with machinery commonly used in industry, this is for ease of implementation in the field using current tools.

Problem Reframing

For this research, biological solutions were sought out by identifying animals and plants which penetrate a substrate.

3.1.2 RETRIEVAL

Biological Solution Search

Several biological systems or organisms that penetrate substrates include: honeybee stinger, mosquito stinger, wasp ovipositor, Sand Lance fish, plant roots, earthworms, and razor clams.

3.1.3 MAPPING AND TRANSFER

Biological Solution Definition

This research focuses on the "forms" description of the biological solutions. The forms in question are the apex angle and symmetry of natural penetrometers and their ability to influence the penetration resistance.

Principle Extraction

The principles extracted for this research include the use of a honey bee stinger or wasp ovipositor with an apex angle of about 30°, which is smaller than that typically used for geotechnical engineering applications as well as and an asymmetric tip (Ling et al. 2016; Cerkvenik et al. 2017). Figure 16 displays an SEM image of a honeybee stinger and Figure 7 displays an SEM image of a mosquito stinger; both of these are biological organisms whose principles were extracted for this research.

Principle Application

This research applies these principles through 3D DEM simulations to complete a study on the effects of apex angle and asymmetry on penetration resistance.

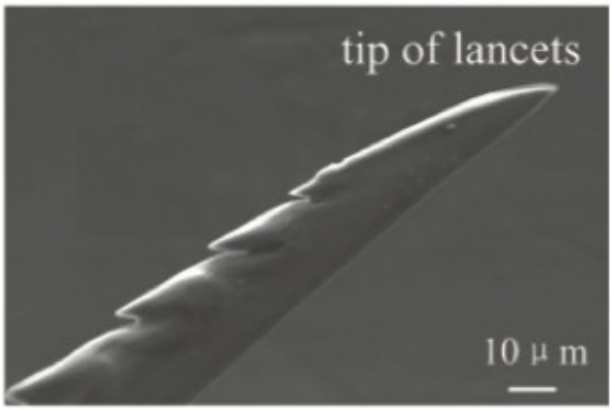

Figure 16. SEM image of a honeybee stinger (Ling et al. 2016)

3.2 DEM SIMULATON

Three dimensional simulations were performed using PFC3D Version 5.0.33 64 bit from Itasca Consulting Group, Inc.. PFC3D is a general framework distinct element modeling software. PFC3D was used to generate the vessels, particles, and symmetric probes. Rhinoceros Version 5.14 was used to draft the asymmetric probe geometries, which were then imported into PFC3D.

3.2.1 TESTING PLAN

A testing plan was developed focusing on altering two main parameters of the conical tips considered: tip geometry, consisting of the apex angle and tip symmetry, and the confinement conditions imposed on the soil specimen. Two simulation chambers were developed; one to simulate shallow penetration (referred to as the unconfined simulation, Figure 2) and one to simulate deep penetration (referred to as the confined simulation, Figure 3). An example of soil failure mechanisms in shallow and deep penetration conditions is displayed in Figure 17.

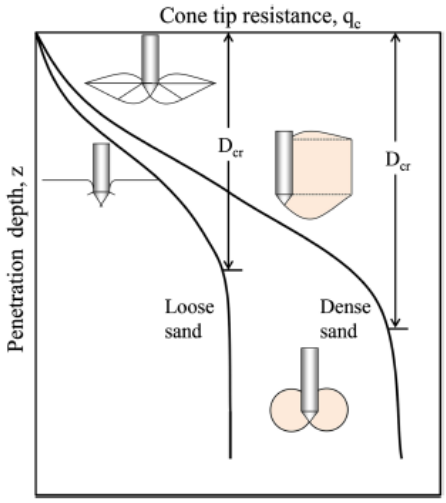

Figure 17. Visual representation of failure mechanisms for different phases of cone penetration with depth (Kim et al. 2016)

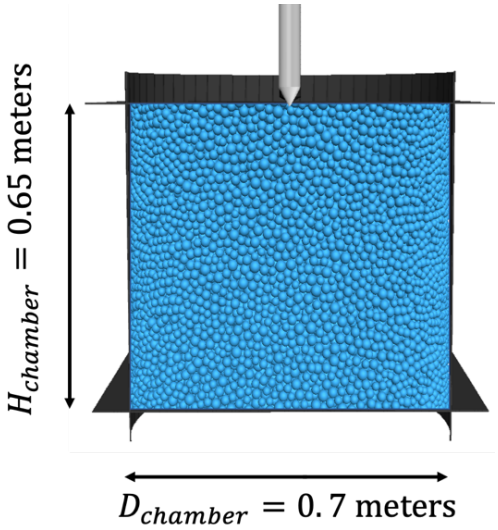

Figure 18. Schematic of unconfined specimen, note that a gravitational acceleration of 9.81 m/s^2 is included in this simulation

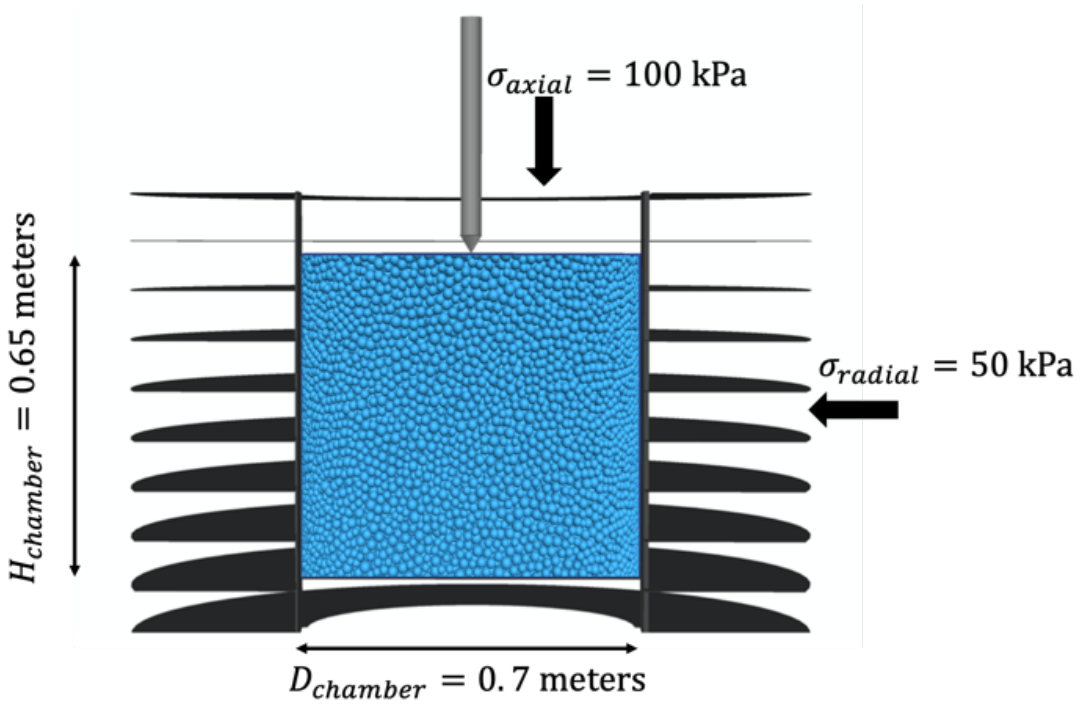

Figure 19. Schematic of confined specimen, note that no gravitational acceleration is included in this simulation

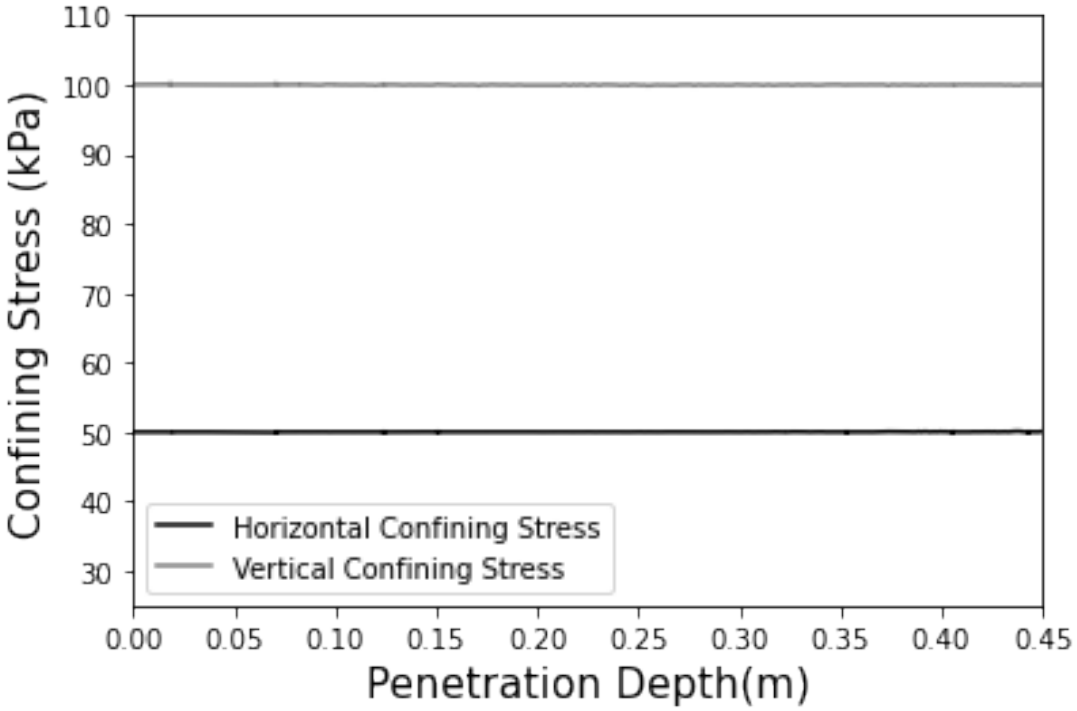

Figure 20. Horizontal and vertical stresses throughout penetration for the confined vessels

Figure 18 displays the unconfined specimen, while Figure 19 displays a confined specimen. To simulate shallow penetration, the particles were generated, and no confinement stress was applied to the granular assembly. The particles were allowed to settle under gravity (g = 9.81 m/s^2) which was maintained throughout the simulation. In the unconfined specimen the chamber bottom and radial walls are rigid. In this configuration, the soil failure mechanism during penetration can reach the soil surface due to the small overburden pressures. Thus, the particles are able to move to the surface of the specimen, which is expressed as soil heave, as shown schematically for the smaller penetration depth in Figure 17.

To simulate deep penetration, the particles were generated in the virtual calibration chamber and then confined to a vertical stress of 100 kPa applied by a rigid top plate and a radial stress of 50 kPa applied by six rings surrounding the vessel these stresses are held constant throughout penetration as illustrated in Figure 20. No gravitational acceleration is applied in these simulations. In this specimen, the failure within the soil does not reach the soil surface, creating the local soil failure and flow around the penetrometer's tip, characteristic of deep penetration conditions. A schematic of such failure mechanism is shown in Figure 17 at greater penetration depths.

The confined and unconfined specimens were chosen so that the soil failure mechanisms could be examined for both shallow and deep penetration conditions. For example, the unconfined specimen did not have a top plate or confining stress, therefore the soil failure mechanisms were allowed to return to the surface, similar to what would happen in the physical world. The confined specimen was confined under a vertical stress of 100 kPa and had a top plate so that soil particles could not move beyond the vessel, enforcing a similar condition to what is expected during confined penetration. Additionally, a horizontal stress of 50 kPa was applied to the vessel.

Probes with varying tip apex angles were simulated, these apex angles include: 15°, 30°, 45°, 60°, 90°, 120°, 150°, and 180°. The symmetric probe tips are displayed in Figure 21. These angles were chosen because they cover a wide range of angles and encompass current geotechnical engineering standard in probe angles as well as bio-inspired probe angles. For example, an apex angle of 60° is typically used in CPT probes, while a 180° or "flat-tip" is typically used in piles. A 30° apex angle is a similar tip angle to that of a honeybee or wasp stinger.

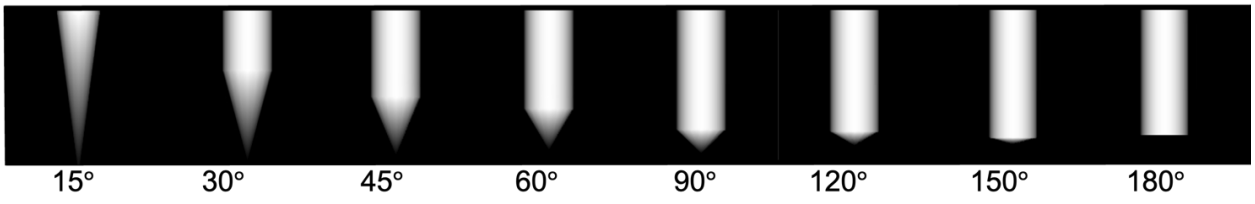

Figure 21. Symmetric probe tips

Tip symmetry was varied for the probes with apex angles of 30° and 60°. For each asymmetric geometry an "alpha factor" was defined such that the probe tips had an "alpha factor" between 0 and 1. *Equation (1*) describes how alpha factor is calculated and Figure 22 illustrates an example calculation of the alpha factors.

$$\alpha = \frac{Half\ Apex\ Angle\ 2}{Half\ Apex\ Angle\ 1}$$ *Equation (1)*

Figure 22. Visual representation of alpha factor

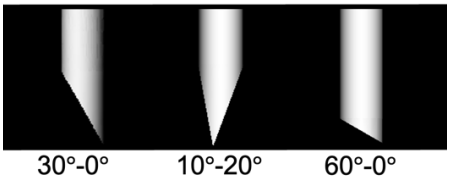

Figure 23. Asymmetric probe tips

A total of 22 DEM simulations were performed as part of this research. The complete testing matrix for unconfined and confined specimens can be found in Table 4 and Table 5, respectively.

Table 4. Unconfined numerical simulations matrix

Simulation ID	Probe Geometry	Total Apex Angle, *degrees*	Half Apex Angle 1, degrees	Half Apex Angle 2, *degrees*
US15	Symmetric	15	7.5	7.5
US30		30	15	15
US45		45	22.5	22.5
US60		60	30	30
US90		90	45	45
US120		120	60	60
US150		150	75	75
US180		180	90	90
UA30-0	Asymmetric	30	30	0
UA20-10		30	20	10
UA60-0		60	60	0

Table 5. Confined numerical simulations matrix

Simulation ID	Probe Geometry	Total Apex Angle, *degrees*	Half Apex Angle 1, degrees	Half Apex Angle 2, *degrees*
CS15	Symmetric Apex	15	7.5	7.5
CS30		30	15	15
CS45		45	22.5	22.5
CS60		60	30	30
CS90		90	45	45
CS120		120	60	60
CS150		150	75	75
CS180		180	90	90
CA30-0	Asymmetric Apex	30	30	0
CA20-10		30	20	10
CA60-0		60	60	0

3.2.2 SIMULATION CONFIGURATION AND PARAMETERS

The parameters for the DEM simulations are discussed herein, which were the same for the shallow and confined specimens except for when otherwise specified. A soil grain distribution curve was created for a granular material to ensure reasonable run times. A scaling factor was applied to the soil grain distribution curve to decrease computational time. Particle scaling multipliers are commonly used in DEM simulations for this purposes (Arroyo et al. 2011; Butlanska et al. 2014; Chen et al. 2021; 2020; M. O. Ciantia, O'Sullivan, and Jardine 2019; Matteo Oryem Ciantia et al. 2016; Khosravi, Martinez, and DeJong 2020; Sadek, Tekeste, and

Naderi 2017; Zeng and Chen 2016; Zhang et al. 2019). Although the increase in particle size can cause larger than typical oscillations in penetration resistances, average tip resistance values have been shown to be relatively independent of particle sizes as long as the probe to diameter size ratio is greater than about 3.0 (Khosravi, Martinez, and DeJong 2020). For the particles simulated in this study, the mean particle diameter (D_{50}) is 14.3 mm, coefficient of uniformity is 1.21 and the coefficient of curvature is 0.97. The grain size distribution of the simulated soil is shown in Figure 24. Based on these values, this soil is poorly graded according to the USCS methodology, ASTM standard D2487.

The calibration chamber used in both the confined an unconfined simulations is cylindrical in shape with a diameter of 0.7 meters and a height 0.65 meters. The probe used in all simulations has a diameter of 0.044 meters and the tip of the probe was penetrated in the sample to a depth of 0.45 meters. It is important to consider the distance between the probe and vessel boundaries to prevent boundary effects from impacting simulation results. Typical values for chamber diameter to probe diameter ratios range from 6 to 16.9 for 3D DEM simulations (Table 2, Arroyo et al., 2011; Butlanska et al., 2014; Sadek et al., 2017). The chamber diameter to probe diameter ratio used for these simulations is 15.9. Additionally, the ratio of probe to particle diameter is important to limit because once the probe to particle mean diameter ratio becomes too small the behavior of the particles around the tip of the probe begin to no longer represent expected soil behavior. Typical ranges of probe diameter to mean particle diameter ratio for 3D DEM simulations are from 2.7 to 5 (Table 2, Arroyo et al., 2011; Butlanska et al., 2014; Sadek et al., 2017). The probe diameter to mean particle diameter ratio for these simulations is 3.1.

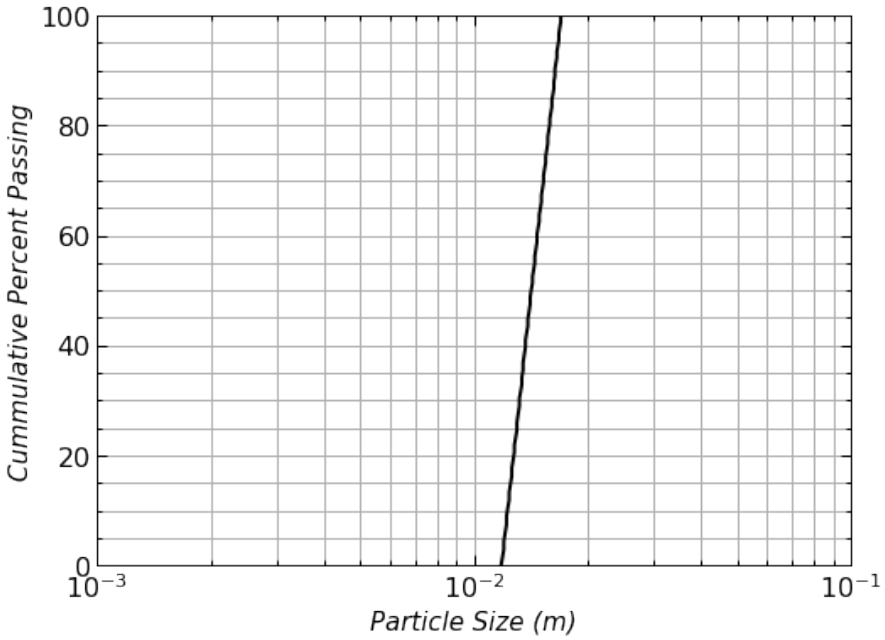

Figure 24. Soil grain distribution curve

The particles in the simulation were assigned a linear contact model with rolling resistance. This model and simulation parameters have been shown to reproduce the behavior of sub-rounded to sub-angular particles. The soil friction angle is 35.9°. Examples of the soil behavior in triaxial compression and CPT testing can be seen in Figure 25 and Figure 26, respectively (Chen et al. 2021). The behavior of the soil in Figure 25 is consistent triaxial compression results for a granular material; there is an increase in deviatoric stress with increasing confining stress and a decrease in dilation with increasing confining stress. Additionally, Figure 26 produces expected CPT tip penetration resistance for the tested confining stresses, the soil behavior type chart shows results consistent with the behavior of granular materials; as the confining stress increases the soil moves from being sand like dilative to sand like contractive. The linear contact model with rolling resistance is dependent on input parameters such as normal stiffness, k_n, shear stiffness, k_s, sliding and rolling friction coefficients μ and μ_{rr} respectively. The parameters used in the simulations can be found in Table 6 and Table 7 for the unconfined and confined

simulation parameters, respectively. A detailed description of the calibration procedure employed to determine these parameters can be found in Kuei et al. (2020) and Chen et al. (2021).

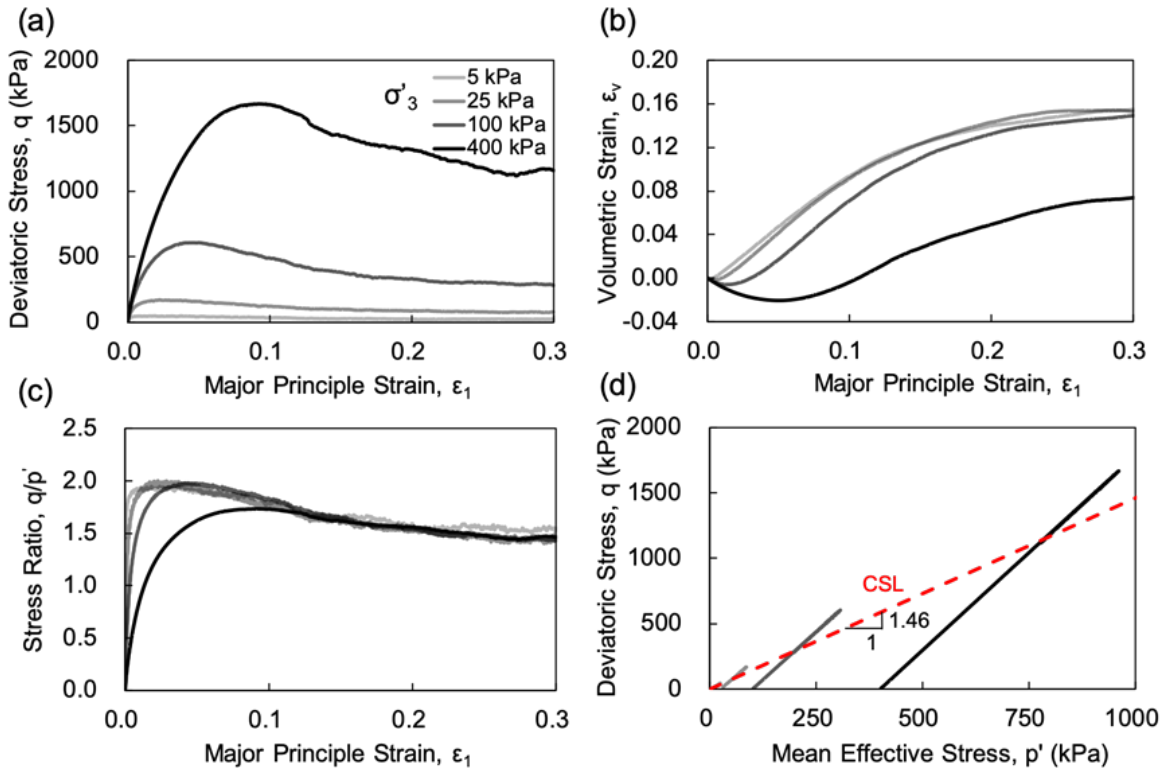

Figure 25. "Results of triaxial compression tests at isotropic confining pressures of 5, 25, 100, and 400 kPa. Evolution of (a) deviatoric stress ($q = \sigma_1' - \sigma_3'$), (b) volumetric strain, and (c) stress ratio (q / p') with major principal strain and (d) stress paths in the $q - p'$ plane. CSL is the critical state line." (Chen et al. 2021)

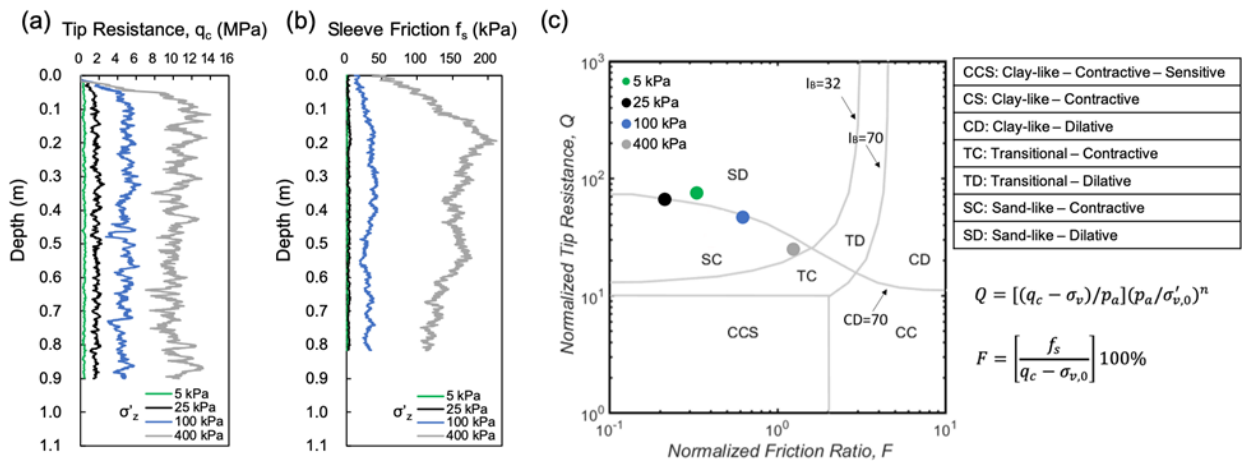

Figure 26. "Signatures of (a) tip penetration resistance and (b) sleeve friction with depth, and (c) soil behavior type classification based on penetration resistance measurements." (Chen et al. 2021)

3.2.4 UNCONFINED SPECIMEN

The unconfined specimen was generated in two main stages: chamber and particle generation and gravity loading. In the vessel and particle generation stage, the vessel and 106,000 particles were generated. Next, the particles were allowed to settle under gravity. Figure 27 displays the radial and vertical stress distributions throughout the unconfined specimen. As expected, there is a vertical gradient in the stress distributions corresponding to the unit weight of the simulated soils. The initial void ratio and porosity of the sample were 0.59 and 0.37, respectively. Finally, the probe was inserted into the vessel at a penetration rate of 0.000002 m/s until the tip of the probe reached 0.45 meters. This penetration rate is slower than what is used for the confined specimen because any penetration rate faster than this did not meet the quasi-static state condition and the overlap between the particles and the probe would be too large, causing numerical instabilities. The average inertial number for the penetration phase had an average inertial value of 1.9×10^{-14} and maximum inertial value of 8.8×10^{-8}. According to O'Sullivan 2011, the inertial number should be significantly less than one to ensure quasi-static

penetration; additionally, recommendations from Janda and Ooi, 2016 suggest inertial numbers below 1×10^{-2} for quasi-static penetration. Based on these recommendations, the simulations can be considered to be in a quasi-static state. The overlap at the end of cone penetration remained smaller than 1% of the particles' radius, for 99% of the particles.

Table 6. DEM simulation parameters for unconfined simulations

Input Parameter	*Symbol*	*Value*
Shear Stiffness	k_s	*1.12E+06*
Normal Stiffness	k_n	*1.67E+06*
Normal to Shear Stiffness Ratio	k_n / k_s	*1.5*
Sliding Friction Coefficient	μ	*0.4*
Rolling Friction Coefficient	μ_{rr}	*0.4*
Ball-Wall Friction Coefficient	μ'	*0.0*
Probe-Particle Friction Coefficient		*0.3*
Particle Density (kg/m^3)	G_s	*2650*
Local Damping	β	*0.1*

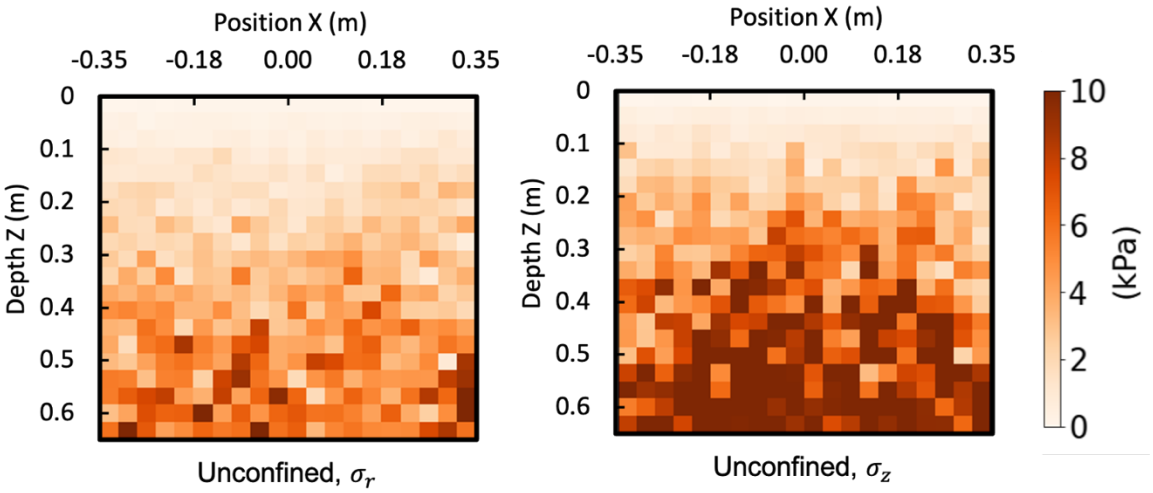

Figure 27. Stress plots for radial and vertical stresses in unconfined specimen

3.2.3 CONFINED SPECIMEN

The confined specimen was generated in three main stages: chamber and particle generation, specimen confinement, and addition of the radial rings. In the chamber and particle generation stage, the vessel and approximately 106,000 particles were generated. The initial void ratio and

porosity of the sample were 0.59 and 0.37, respectively. The specimen was then confined to a vertical stress of 100 kPa using only the top walls while a single cylindrical radial wall applied a radial stress of 50 kPa. These stresses lead to a K_o value of 0.5, typical for sandy soils (Robertson 2016). Next, the cylindrical wall was substituted by six rings to maintain a uniform radial stress throughout the simulation. Each of these rings can move independently and was controlled by a servo-control to enforce a constant stress of 50 kPa. Finally, the probe was inserted into the vessel at a penetration rate of 0.20 m/s until the tip of the probe reached 0.45 meters in depth from the specimen's surface. The average inertial number for the penetration phase had an average inertial value of $3.3 \times 10^{-4}$and maximum inertial value of 8.8×10^{-3}. According to the recommendations from O'Sullivan (2011) and Janda and Ooi (2016) provided in the preceding section, these simulations can be considered to be quasi-static. The overlap at the end of cone penetration remained smaller than 1% of the particles' radius, for 99% of the particles.

Table 7. DEM simulation parameters for confined simulations

Input Parameter	*Symbol*	*Value*
Shear Stiffness	k_s	*1.10E+06*
Normal Stiffness	k_n	*1.65E+06*
Normal to Shear Stiffness Ratio	k_n / k_s	*1.49*
Sliding Friction Coefficient	μ	*0.4*
Rolling Friction Coefficient	μ_{rr}	*0.4*
Ball-Wall Friction Coefficient	μ'	*0.1*
Probe-Particle Friction Coefficient		*0.3*
Particle Density (kg/m^3)	G_s	*2650*
Local Damping	β	*0.1*

3.2.5 PROBE GENERATION

Symmetric probes were generated using PFC's built-in wall generation command. Asymmetric probes were generated using Rhinoceros 3D, a computer-aided design software that is compatible with PFC. Asymmetric probes were then imported into PFC and assigned the same parameters and coefficients as the symmetric probes, included in Tables 6 and 7.

3.3 MODEL VERIFICATION

Model verification was performed by comparing q_c values for a specimen confined to 100 kPa with a 60° apex angle to the results from Chen et al. (2021). In Chen et al. (2021), the particles were set to model the behavior of a coarse-grained cohesionless soil, which was calibrated by Kuei et al. (2020). The q_c values obtained in this verification simulation have an average difference of 1.1% in comparison to those obtained by Chen et al. (2021). Although penetration rate, local damping, and stiffness values are slightly different between both studies, the q_c values are within range of what is expected for the repetition of the same CPT simulation in DEM (Khosravi, Martinez, and DeJong 2020). Table 8 below compares the parameters used in Chen et al. (2021) and in this study.

Table 8. Parameters comparison (Chen et al. 2021)

Input Parameter	*Symbol*	*Chen et al., 2021*	*This study*
Shear Stiffness (N/m)	k_s	**0.96E+06*	*1.10E+06*
Normal Stiffness (N/m)	k_n	**1.44E+06*	*1.65E+06*
Normal to Shear Stiffness Ratio	k_n/k_s	*1.5*	*1.49*
Probe sleeve-particle friction coefficient		*0.1*	*0.3*
Probe tip-particle friction coefficient		*0.3*	*0.3*
Sliding Friction Coefficient	μ	*0.4*	*0.4*
Rolling Friction Coefficient	μ_{rr}	*0.4*	*0.4*
Ball-Vessel Friction Coefficient	μ'	*0.1*	*0.1*
Particle Density (kg/m^3)	G_s	*2650*	*2650*
Local Damping	β	*0.0*	*0.1*
Scale Factor		*4.897*	*4.897*
Penetration Rate (m/s)		*0.02*	*0.2*

** stiffness determined calculated for a particle with a diameter equal to D_{50}*

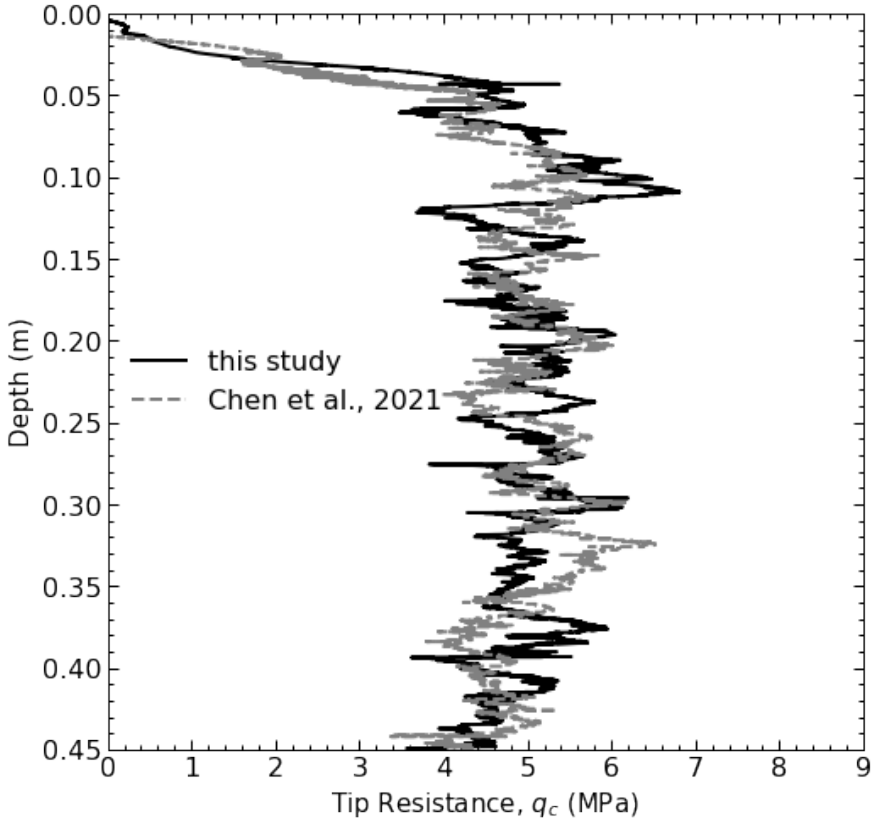

Figure 28. Tip resistance verification

Although the probe- sleeve particle friction coefficient varies between simulation, which can affect the sleeve resistance, the tip resistance remains unaffected. In addition to the comparison

of q_c values to Chen et al. (2021), the average tip stress is consistent with what is typically seen for sands at similar confining stresses (Mayne 2007).

3.4 POST-PROCESSING

3.4.1 CENTER OF SURFACE AREA CORRECTION

It was necessary to perform a center of surface area corrections for the probes with different apex angles. If the center of surface area correction was not done, the soil stress gradient could influence the comparisons of penetration resistance at a given depth. This correction was only implemented for the simulations on unconfined specimens due to the stress gradient caused by the gravitational acceleration. For example, if the center of surface area tip correction was not done, the soil stress at the depth of the tip of the 180° probe would be significantly less than the stress at the tip depth of the 15° probe. This increase in stress can be seen by the stress gradient in Figure 27.The center of surface area is defined as the point along the conical tip's height where half of the tip's surface area is above, and half of the surface area is below. Figure 29 displays an example of the center of surface area correction being applied. This correction was also done for both the symmetric and asymmetric geometries for unconfined penetration conditions. No center of surface area correction was done for confined penetration since the stresses are uniform throughout the sample and are not dependent on depth. As such, the results discussed throughout this thesis are in terms of the depth of the center of surface area of the probe for the unconfined specimen and in terms of tip depth for the confined specimens.

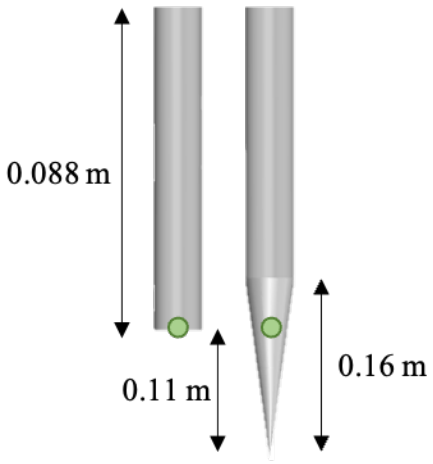

Figure 29. Example center of surface area correction

3.4.2 Z/D RATIO

Z/D ratio is the ratio of center of surface area penetration depth to probe diameter. Z/D ratios are used to describe normalized depths for the probes penetrated into the unconfined vessel.

3.4.3 MEASUREMENT SPHERES

To measure stresses around the probe measurement, spheres 0.033 meters in diameter were assembled throughout the vessel. The ratio of measurement sphere diameter to particle D_{50} is 2.3. The ratio of measurement sphere volume to mean particle volume is 12.3, which is sufficiently large to provide significant measurement of stresses within the sample. An example of the assembly can be seen in Figure 30. These measurement spheres average the stresses of the particles within each sphere, these measurements are used to produce spatial maps of stresses, as shown in Figure 24 and in Chapter 4.

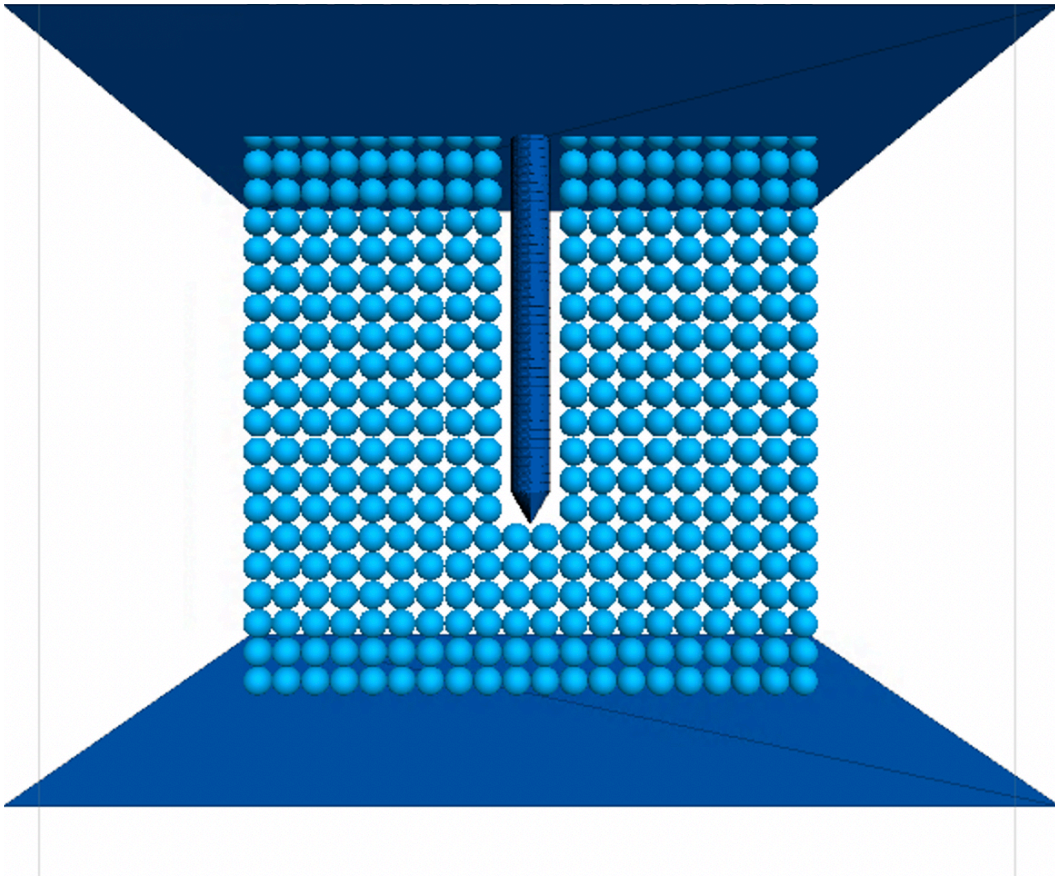

Figure 30. Schematic of measurement spheres

Data recorded from the measurement spheres was used to develop stress maps. Figure 31 and Figure 32 display the vertical and radial stresses across 8 depths for the 15° probe in the confined specimen to show the degree to which the stresses surrounding the probe oscillate in time. Although there is some variation in stress measurements throughout the penetration process, the oscillations tend to be small, and the stresses are generally increasing and moving downward with the probe.

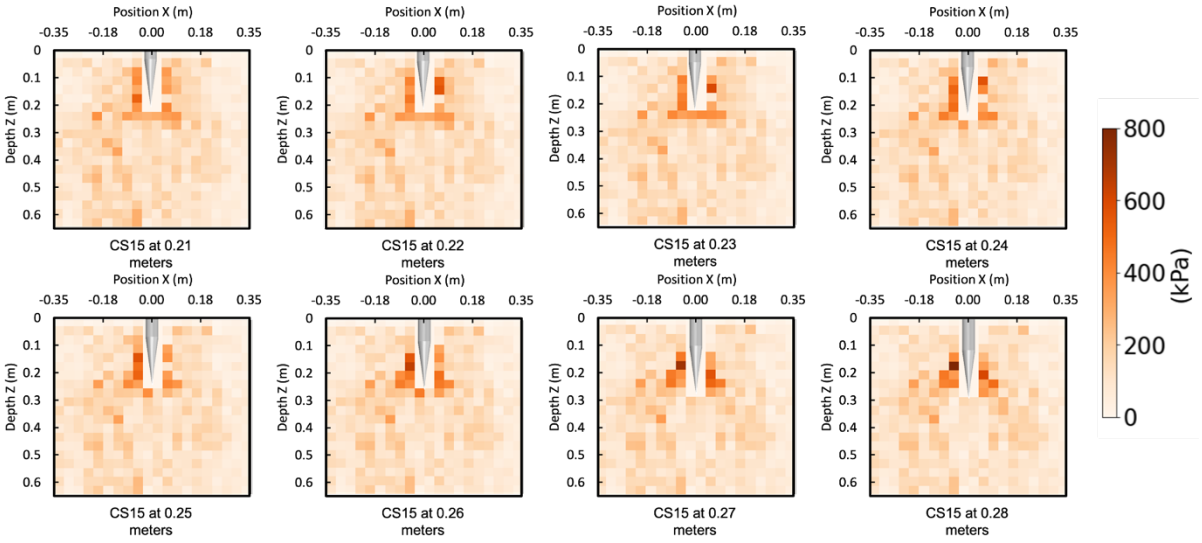

Figure 31. Vertical stress of CS15 at varying penetration depths

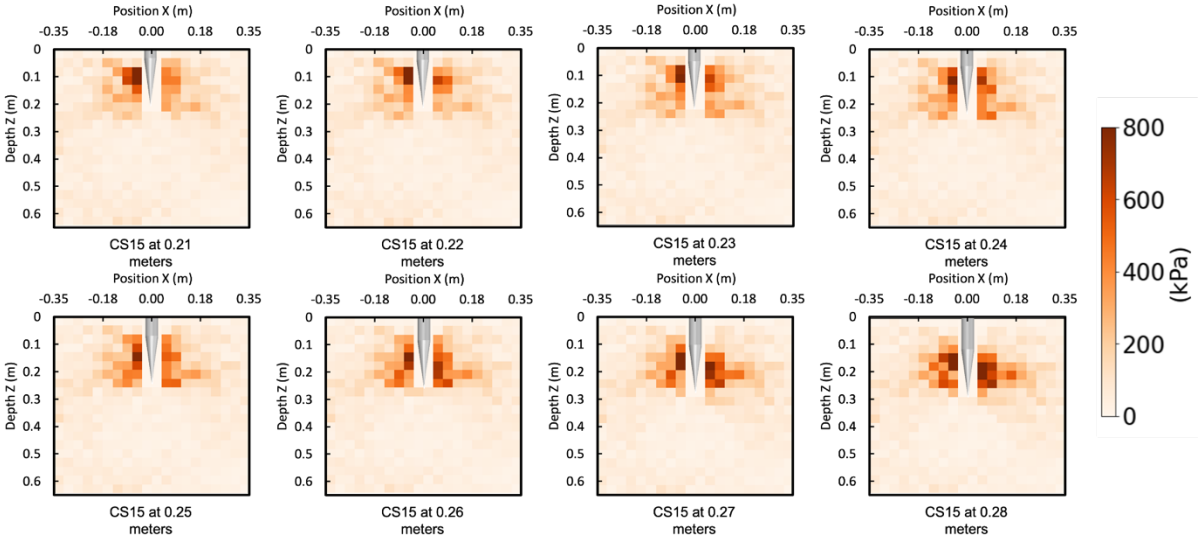

Figure 32. Radial stresses of CS15 at varying penetration depths

4 RESULTS

This section describes the results from the unconfined and confined simulations at global, meso-scale, and micro-scale. As previously described, the unconfined simulations are intended to model shallow penetration conditions, while the confined simulations are intended to model deep penetration conditions. The presented global results describe the tip penetration resistance as a function of depth and the average tip resistance as a function of tip apex angle. Meso-scale results describe the soil behavior and the interactions between the soil and the probe at a spatial scale consistent with the Representative Elementary Volume (REV). This is done by monitoring stresses in measurement spheres, as described in Chapter 3. Micro-scale results are a description of the behavior individual particles. These include force chains, incremental displacements, and total displacements.

A description of the simulation naming convention is described in Figure 33 and the testing matrix is broken down in Table 4 and Table 5. The naming convention is such that the first letter indicates whether a confined or unconfined specimen was tested (C or U). The second letter indicates whether the simulated probe had a symmetric or asymmetric tip (S or A). Finally, the number indicates the tip apex angle in degrees, with names for simulations on symmetric probes including only one number (e.g., 30 for a 30° apex angle) and names for with simulations on asymmetric probes including two numbers, each indicating a half apex angle (e.g., 30-0 indicating a half apex angles of 30° and 0°). In this chapter, the results of the simulations on symmetric probes are first described for both unconfined and confined specimens. Then, the simulation results of the simulations on asymmetric probes are provided.

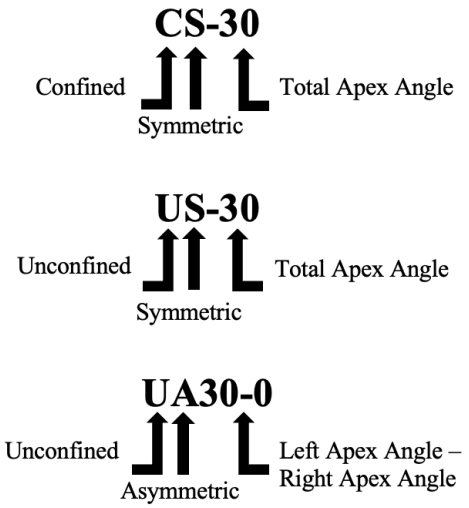

Figure 33. Example of simulation naming convention

4.1 SIMULATIONS ON SYMMETRIC PROBES

4.1.1 GLOBAL RESULTS

During the unconfined simulations, the q_c values were recorded as the probe is penetrated into the specimen. Figure 34 shows profiles of q_c versus center of surface area depth for unconfined simulations with symmetric probes. The q_c values increase linearly with depth, likely due to the increase in overburden stress with depth. This linear increase in effective stress is due to gravity and can be seen in Figure 27. Stress plots for radial and vertical stresses in unconfined specimen The results show that the probes with greater tip apex angles generated greater tip resistance values throughout the penetration process.

Figure 35 displays q_c versus depth profiles for the confined symmetric probes. The penetration resistance for all probes increases rapidly at shallow depths, then reaches a near constant value; the near constant value is achieved due to the constant stress applied to the specimen. The tip resistance reaches a constant value sooner for the obtuse tip angles, this is because it takes a

shorter distance for the entire probe to be within the simulation vessel. The probes with greater tip apex angles are seen to mobilize a greater average tip resistance values throughout the penetration process.

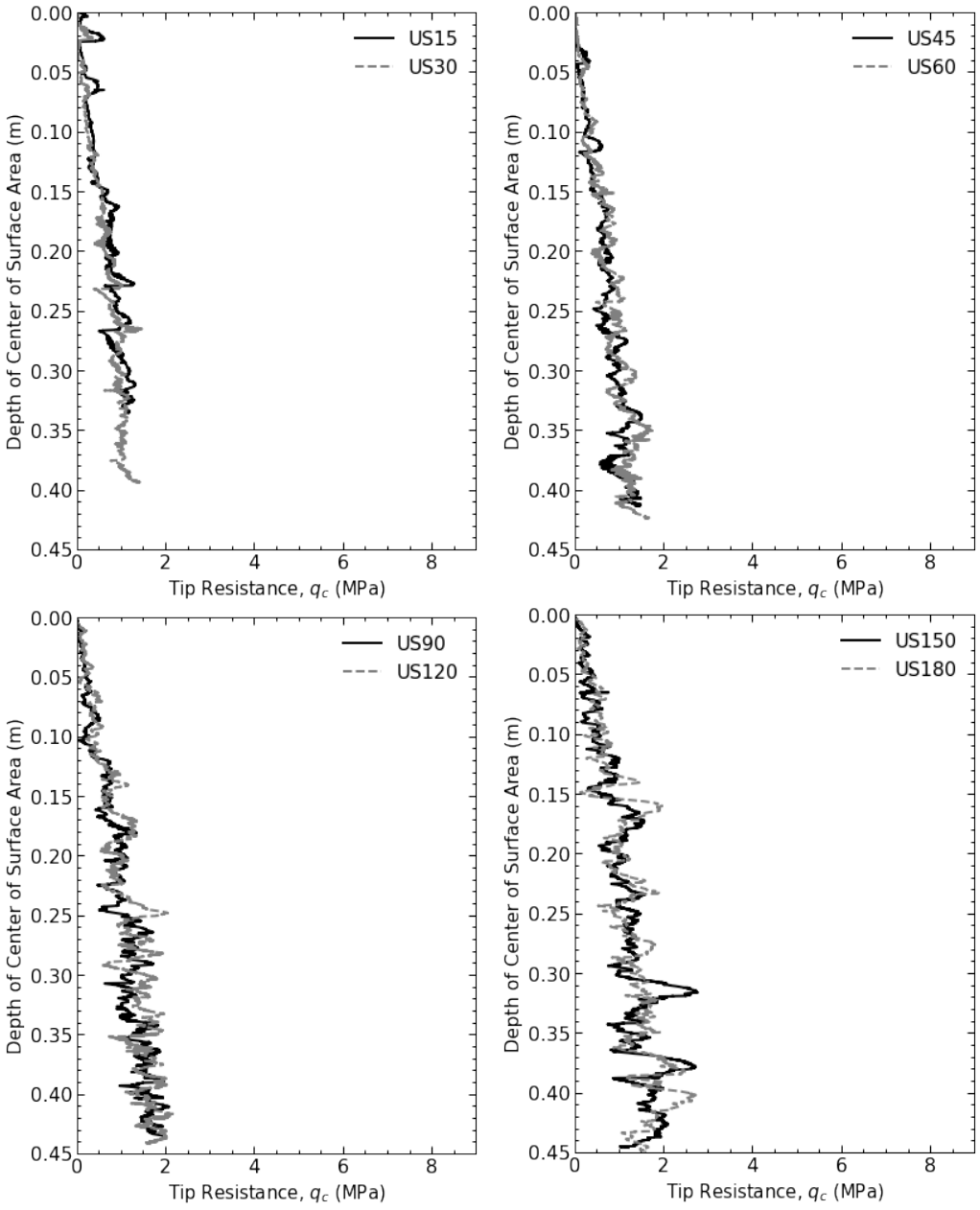

Figure 34. q_c versus center of surface area depth for symmetric probes in an unconfined vessel

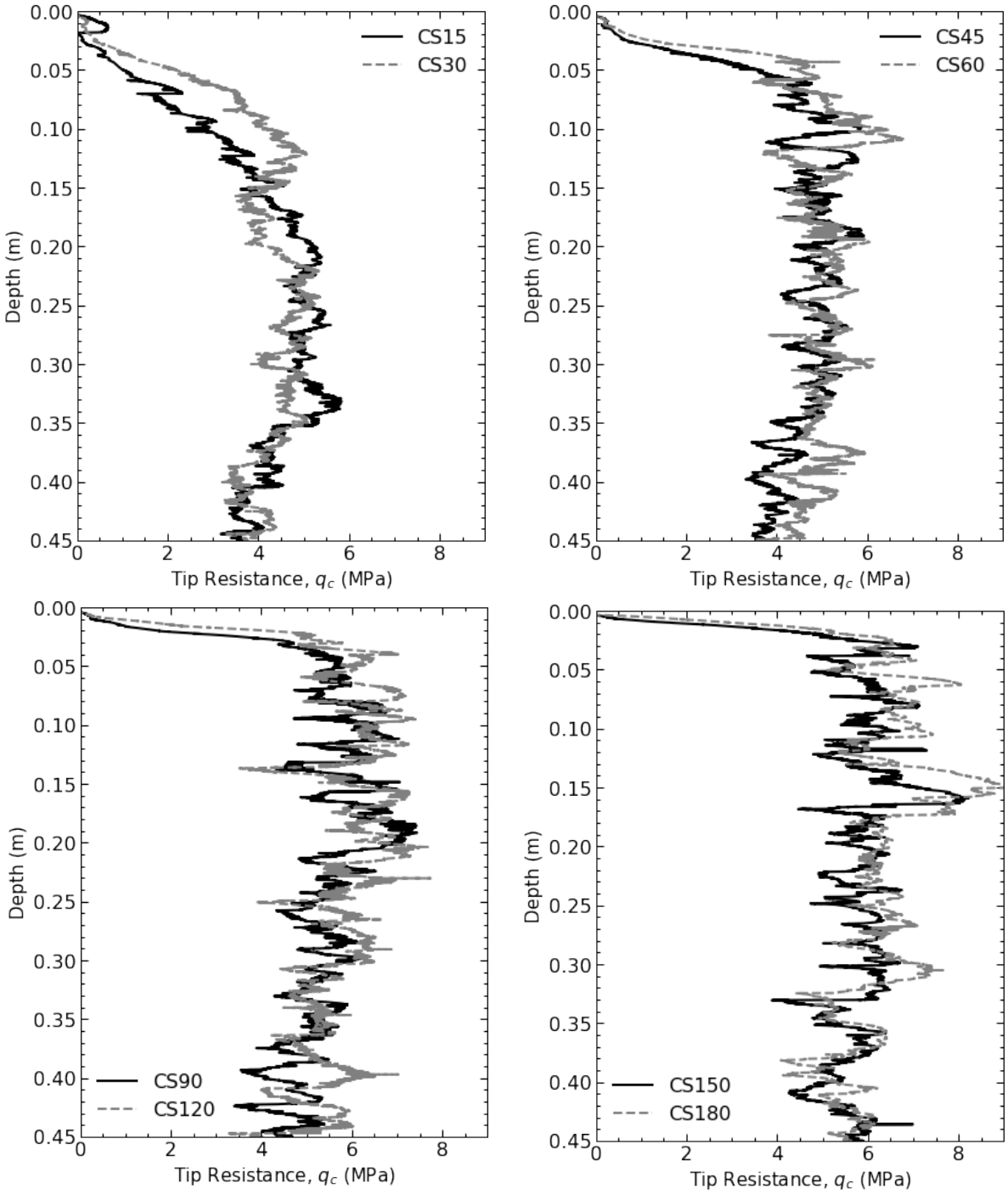

Figure 35. q_c versus depth profiles for symmetric probes in a vessel confined to 100 kPa

The penetration resistance tends to increase as the tip apex angle increases, with the smallest penetration resistances for the 30° and 15° total apex angles for the unconfined and confined

specimens, respectively. Figure 36 displays the relationship between penetration resistance and apex angle for the symmetric probes in both unconfined and confined conditions. The top set of plots illustrate the average tip penetration resistance averaged a depth of 0.044 meters (1x probe diameter) of penetration. The averaged tip penetration resistance was calculated by summing the value of penetration resistance across the 0.044 meters and dividing the sum of the penetration resistance by the number of data points across the 0.044 meters. For the confined simulations the tip resistance values are averaged over the last 0.044 meters of penetration while the unconfined simulations the tip resistance values are averaged at Z/D ratios of 2 and 7. As expected, the unconfined simulations have significantly lower average tip resistances compared to the confined specimen. The bottom set of plots illustrate the same results as the plots above, but the q_c is normalized by the q_c of the 60° probe at either the end of penetration or at the specified Z/D ratio for the confined and unconfined specimens, respectively. The calculation of the normalized q_c value or $q_{c,norm}$ is described in *Equation (2*).

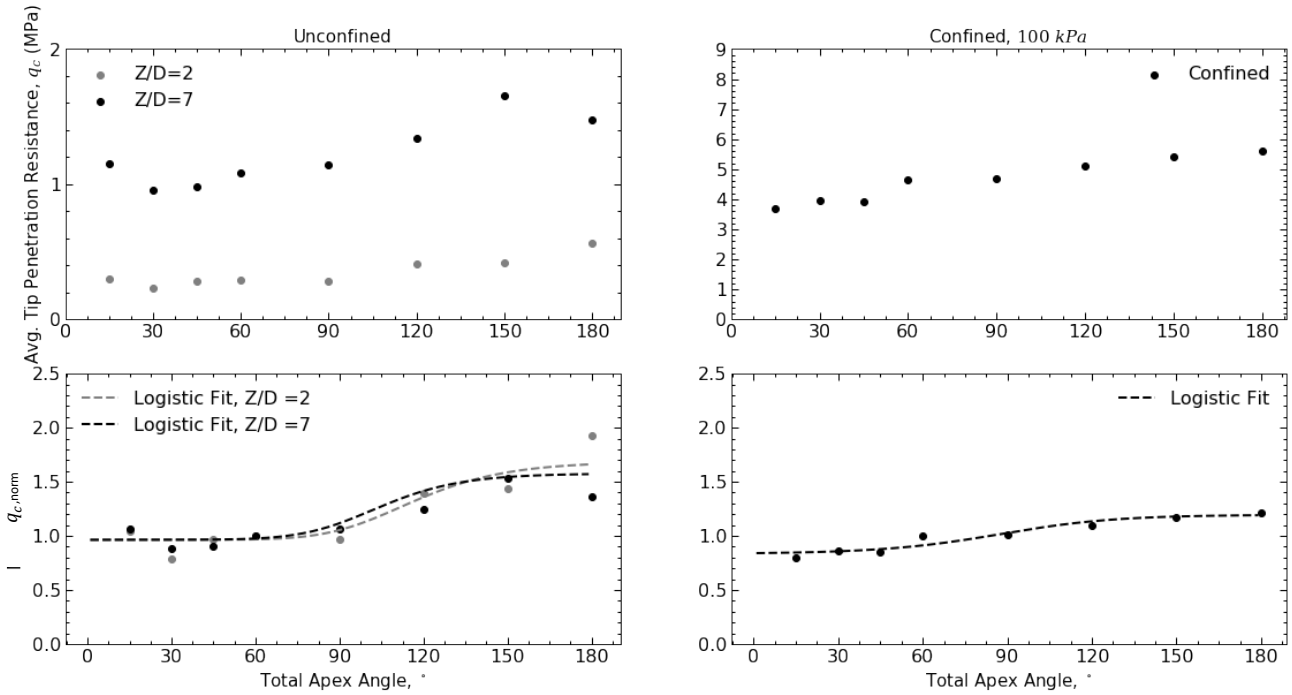

Figure 36. Penetration resistance and $q_{c,norm}$ versus apex angle for symmetric probes

$$q_c, \text{norm} = \frac{average\ q_c}{average\ q_c\ of\ 60°\ probe} \qquad \textit{Equation (2)}$$

It was found that a logistic relationship can fit the relationship between $q_{c,norm}$ and apex angle. The equation used in the logistic fit relationship can be found in *Equation (3*).

$$q_{c,norm} = q_{c,min} + (q_{c,max} - q_{c,min})\left(\frac{1}{\left(1+e^{-k(x-90°)}\right)}\right)^a \qquad \textit{Equation (3)}$$

where $q_{c,min}$ is the average of minimum $q_{c,norm}$ values, $q_{c,max}$ is the average of maximum $q_{c,norm}$ values, k and a are parameter that controls the shape of the curve, and x is the total apex angle, in degrees. The a-parameter dictates the location of the rise in the relationship within the x-axis; the higher the value of the a-parameter larger the x-axis value at which the relationship increases. The k-parameter controls the rigidness of the curve; as the as k-parameter decreases, the curvature of the s-curve increases. The values of the shape parameters used in Figure 31 displayed in Table 9.

Table 9. Shape parameter values for confined, unconfined Z/D = 2, and unconfined Z/D = 7

Specimen	*k*	*a*
Confined	*0.05*	*0.9*
Unconfined Z/D ratio = 2	*0.05*	*3*
Unconfined Z/D ratio = 7	*0.06*	*2*

4.1.2 MESO-SCALE AND MICRO-SCALE RESULTS OF UNCONFINED SPECIMENS

State of Stresses and Force Chains

Figure 32 shows a spatial map of radial stress magnitudes for simulations with probes of varying apex angle. These results correspond to a normalized depth, Z/D of 2. The stress maps show that as the total probe tip apex angle increases, the radial stresses of greater magnitude tend to move from the sides and shoulder of the probe tip to below the tip. Throughout the unconfined simulations, the data is evaluated at two distinct depths ratios of 2 and 7 to further examine the soil behavior throughout different stages of the penetration process. Figure 38 display the radial stress maps for Z/D of 7 for probes of varying apex angles. The radial stress increases as the probe penetrates further into the vessel, as shown in comparing Figures 32 and 33. For a Z/D of 7, the probes with obtuse apex angles tend to develop the highest radial stresses, while those with right and acute angles tend to generate lower radial stress values. These trends may reflect the greater penetration resistances mobilized by the probes with obtuse apex angles, as shown in Figure 31.

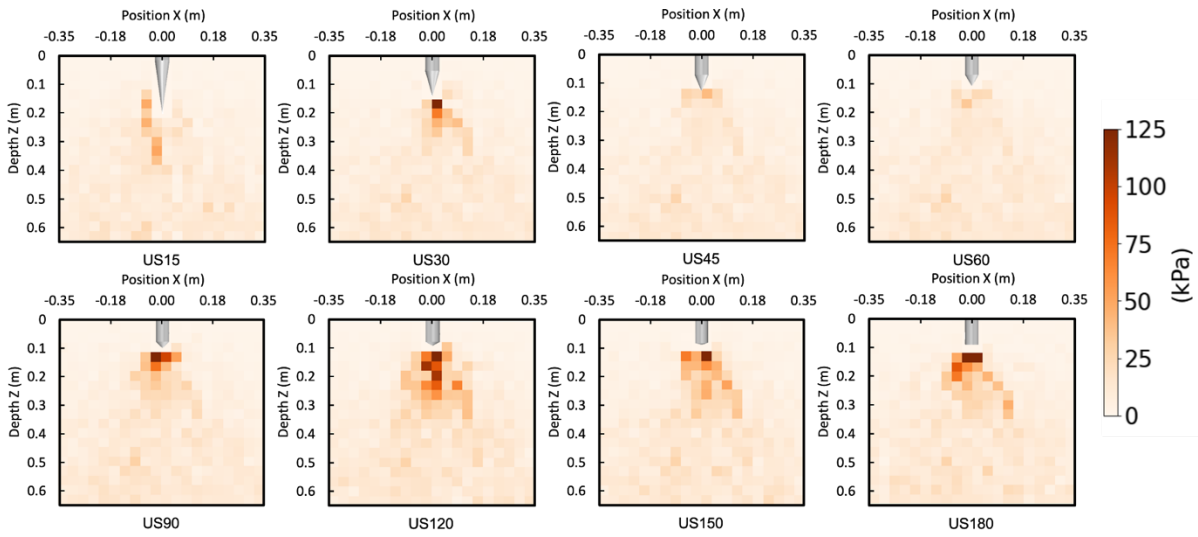

Figure 37. Radial stress generated by symmetric probes in unconfined simulations at a Z/D ratio =2

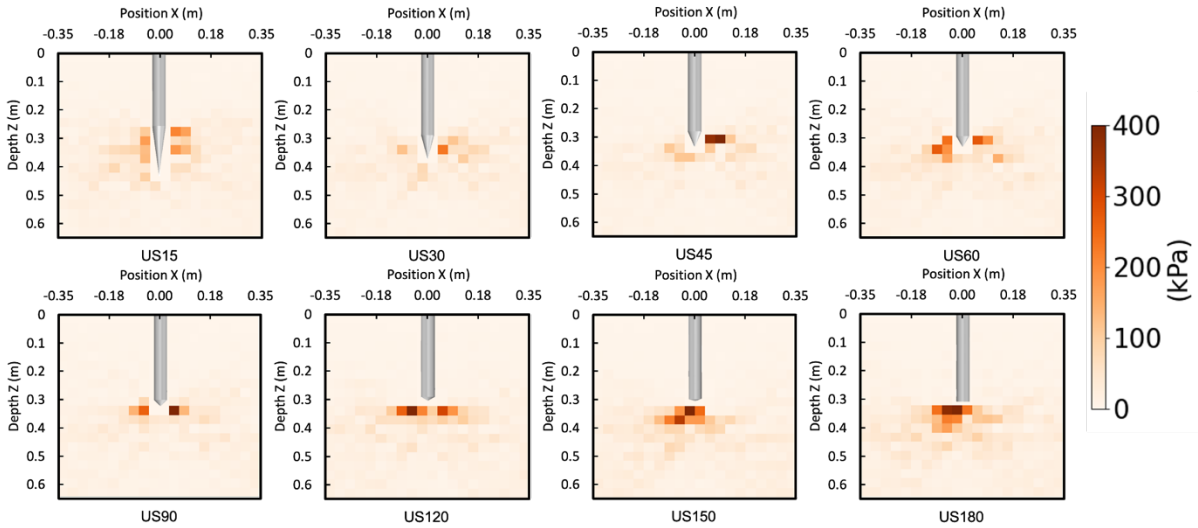

Figure 38. Radial stress generated by symmetric probes in unconfined simulations at a Z/D ratio =7

Figure 39 and Figure 40 display maps of normalized radial stresses for Z/D ratios of 2 and 7, respectively, for the probes of varying apex angles. The horizontal stresses are normalized by the q_c values mobilized at the corresponding depths to highlight the differences in the location and distribution of the highly stressed soil zones. Similar to the non-normalized radial stress plots, the radial stresses normalized by q_c plots see an increase in value as the probe is penetrated

further into the vessel. For both Z/D of 2 and 7, the obtuse apex angles tend to develop the greatest radial stresses/q_c values, while the right and acute angles tend to have smaller values.

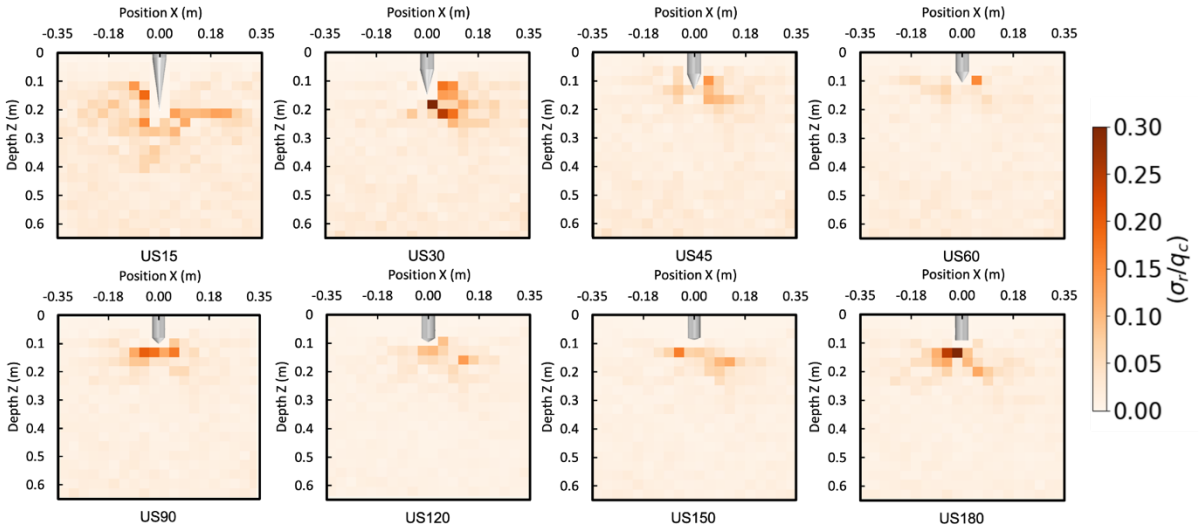

Figure 39. Radial stress generated by symmetric probes in unconfined simulations at a Z/D ratio =2 normalized by q_c

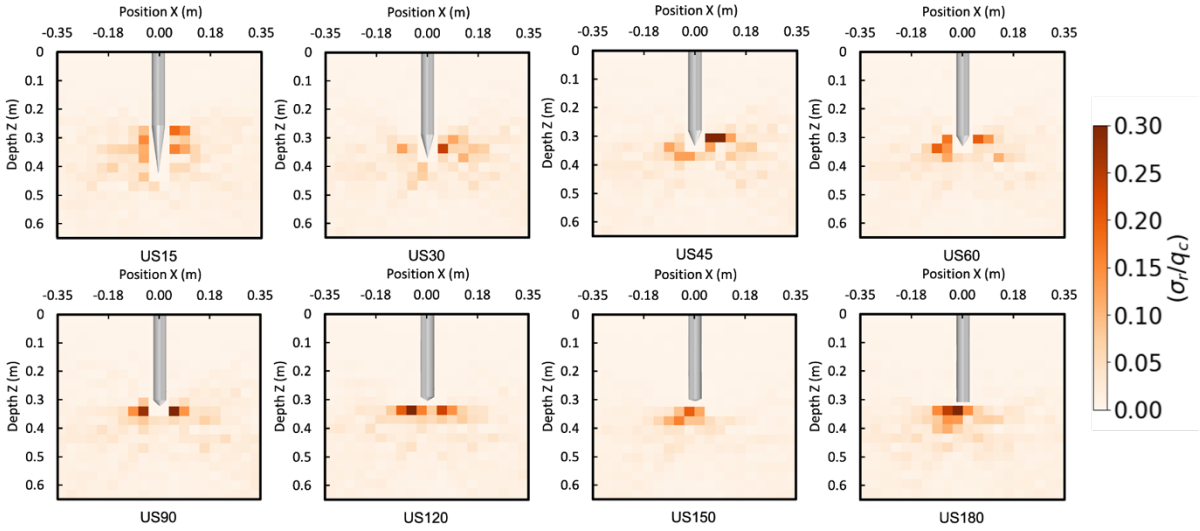

Figure 40. Radial stress generated by symmetric probes in unconfined simulations at a Z/D ratio = 7 normalized by q_c

Figure 41 and Figure 42 display vertical stresses maps for Z/D of 2 and 7, respectively, for the simulations with probes of varying apex angles. For all apex angles, the vertical stress is

concentrated at the tip of the probe. At a Z/D ratio of 2, the 120° probe experienced the highest concentration of vertical stress below the tip. At a Z/D ratio of 7, the 150° probe experienced the highest concentration of vertical stresses below the tip. Overall, as the tip apex angle increases, the vertical stress within the soil increases. In a similar manner as previously described for the radial stresses, these trends may also be a reflection of the greater penetration resistances mobilized by the probes with obtuse apex angles as shown in Figure 31.

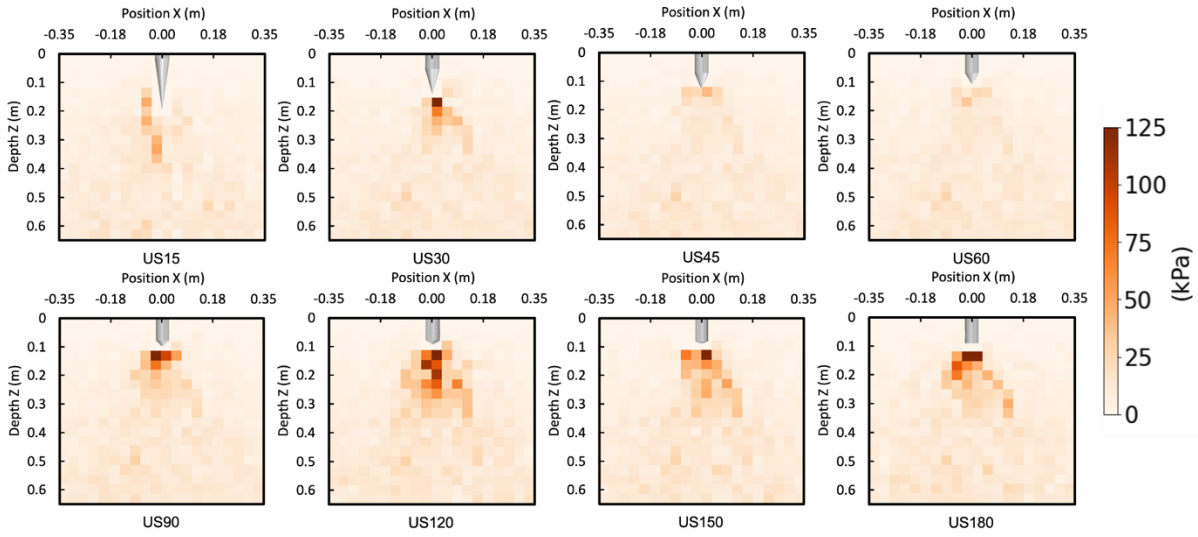

Figure 41. Vertical stress generated by symmetric probes in unconfined simulations at a Z/D ratio =2

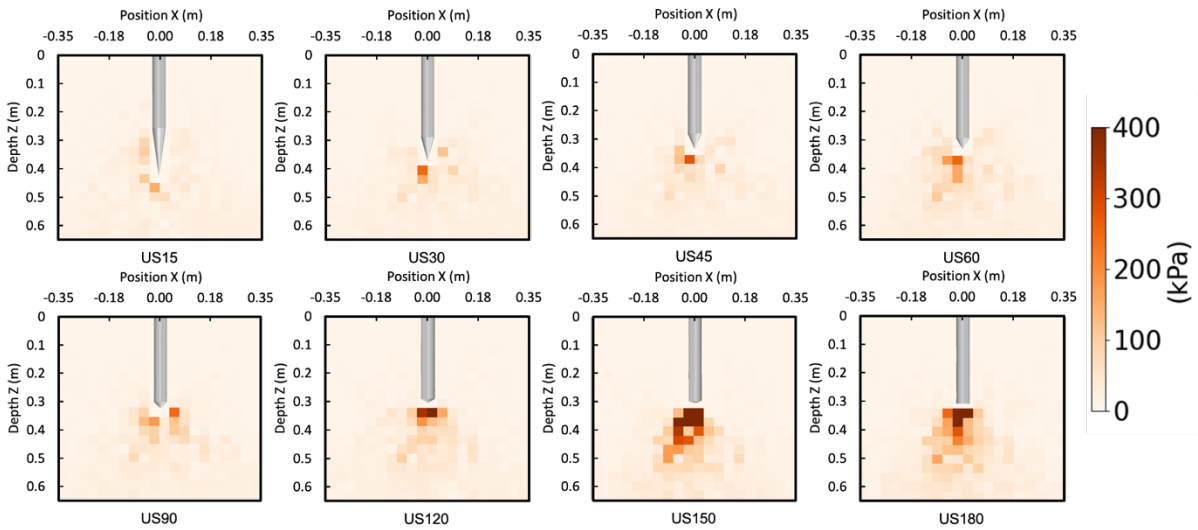

Figure 42. Vertical stress generated by symmetric probes in unconfined simulations at a Z/D ratio =7

Figure 43 and Figure 44 display vertical stresses normalized by q_c for Z/D ratios of 2 and 7, respectively. As the probe is penetrated from a Z/D of 2 to 7, the normalized vertical stress generally increases. The normalized vertical stress is concentrated below the tip of the probe for the right and obtuse apex angles, while for the acute apex angles the normalized vertical stress is seen both below the tip and along the sides of the probe.

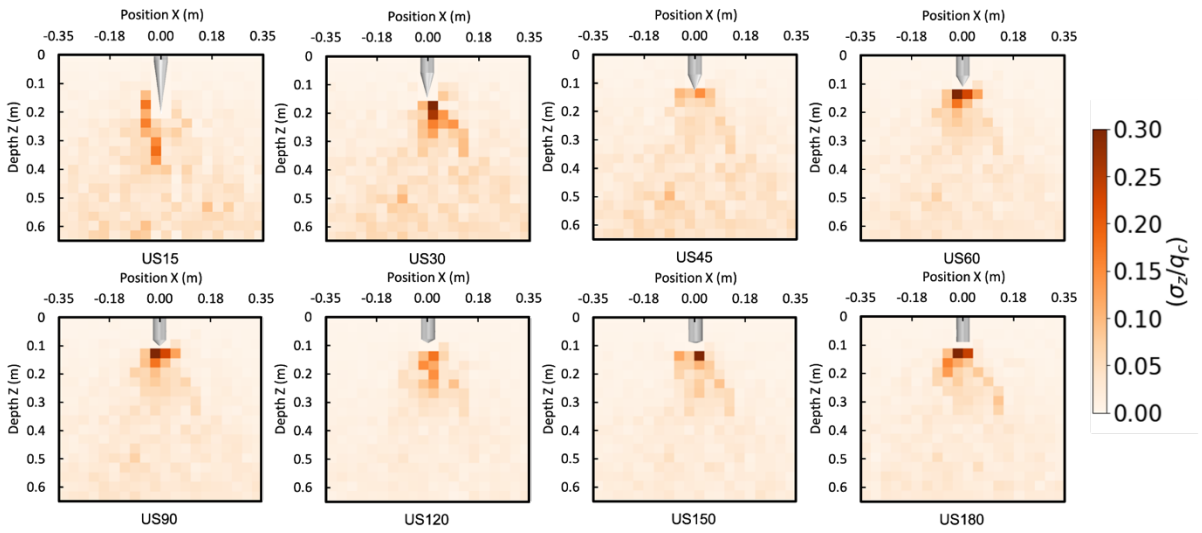

Figure 43. Vertical stress generated by symmetric probes in unconfined simulations at a Z/D ratio = 2 normalized by q_c

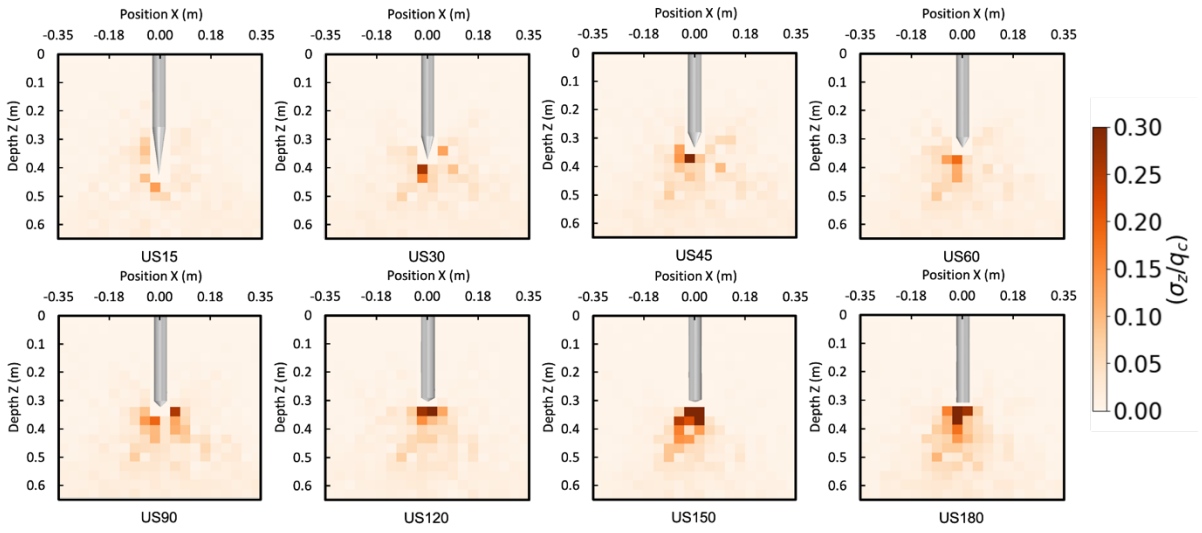

Figure 44. Vertical stress generated by symmetric probes in unconfined simulations at a Z/D ratio = 7 normalized by q_c

Figure 45 and Figure 46 display ratio of radial to vertical stresses for Z/D ratios of 2 and 7, respectively, for the unconfined specimen with probes of varying apex angles. Greater values of radial to vertical stress ratio are concentrated around the sides of the tip. Additionally, the simulations on probes with acute apex angles show slightly greater magnitude of normalized radial stresses and the zones where the ratios are greater than one also appear to be larger for the

probes with acute angles. As the probe progresses from a Z/D ratio of 2 to 7 the concentration of normalized stress moves downward.

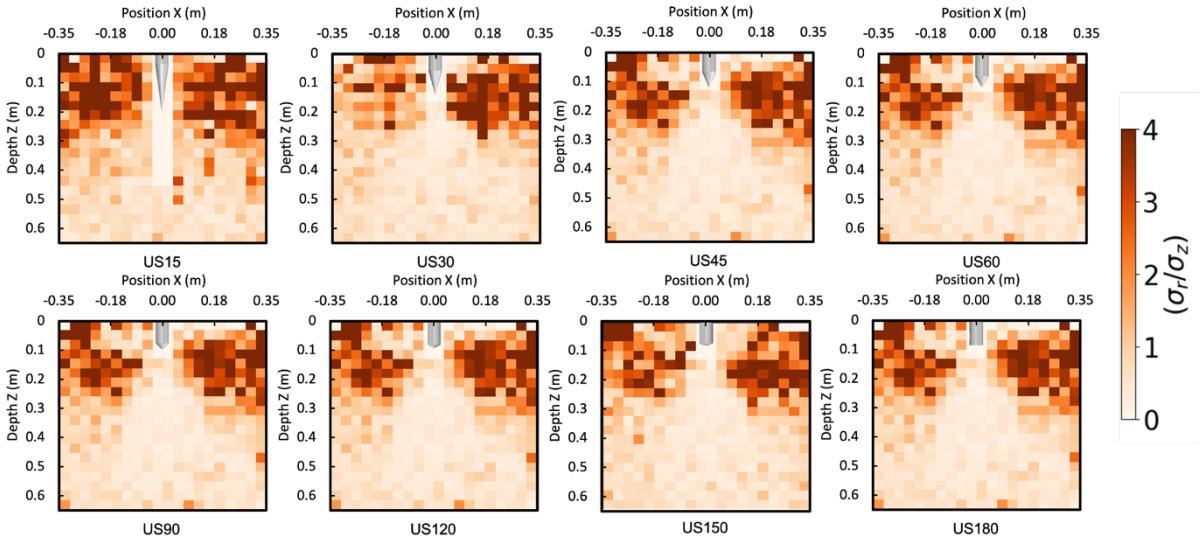

Figure 45. Normalized radial stress by vertical stress plots of symmetric probes in an unconfined vessel, at a Z/D ratio = 2

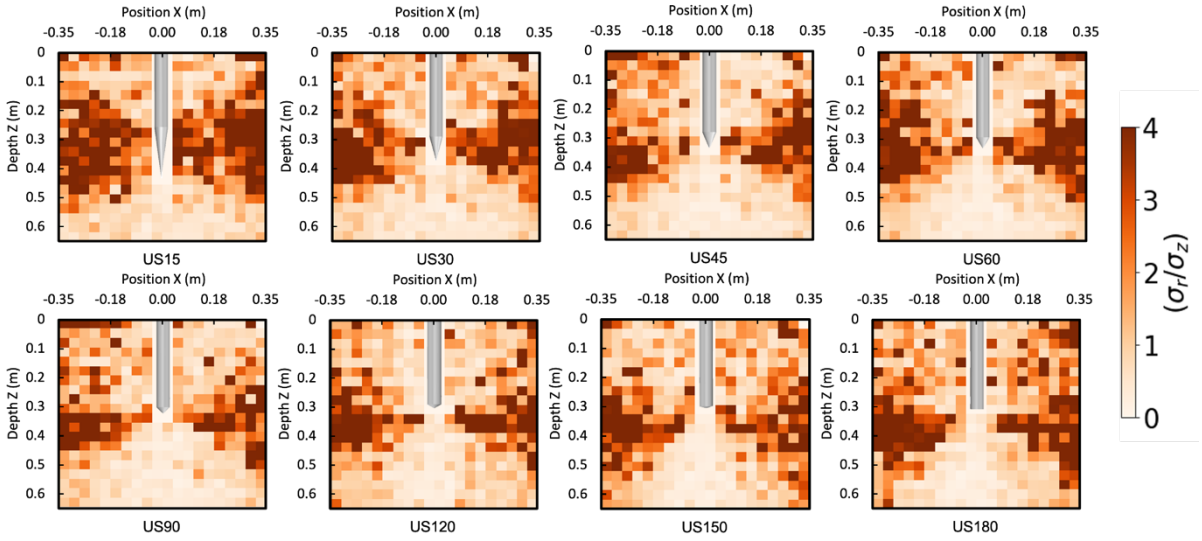

Figure 46. Normalized radial stress by vertical stress, for symmetric probes in an unconfined vessel, at a Z/D ratio = 7

Figure 47 and Figure 48 display the stress state maps for Z/D ratios of 2 and 7, respectively, for the unconfined specimens with probes of varying apex angles. A stress state map represents the

relative magnitudes and orientation of the major and minor principal soil stresses for a given penetration depth. Within each figure, the major and minor principal stresses are divided by the same normalizing value. Within each cross, the longer line represents the major principal stress, and the shorter line represents the minor principal stress. Stress state maps help visually represent the relationship between major and minor principal stresses. The figures show that as the probe is penetrated the minor principal stress along the probe sides rotates from its initial horizontal orientation to a more vertical orientation. The length and orientation of the crosses below the probes' tips are dependent on their apex angle. As the total apex angle of the probe increases, the length of the crosses tend increase, in agreement with the results shown in Figures 32 to 39. The crosses with greatest length are located near the shoulder of the tip the probes with acute apex angles and directly below the tip for the more obtuse apex angles. Near the tips of the probes with obtuse apex angles, crosses of greater length are developed; this indicates stresses with greater magnitudes being developed below the tip, which may be a reflection of the greater penetration resistances mobilized, as shown in Figure 31.

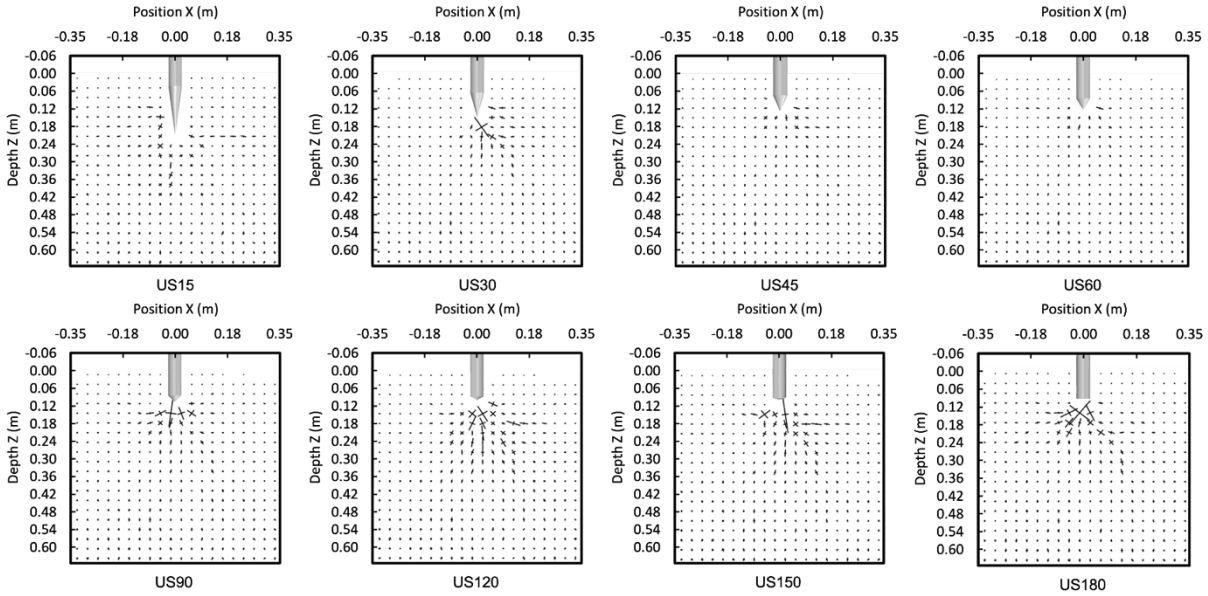

Figure 47. Stress state maps of symmetric probes in an unconfined vessel, at a Z/D ratio =2

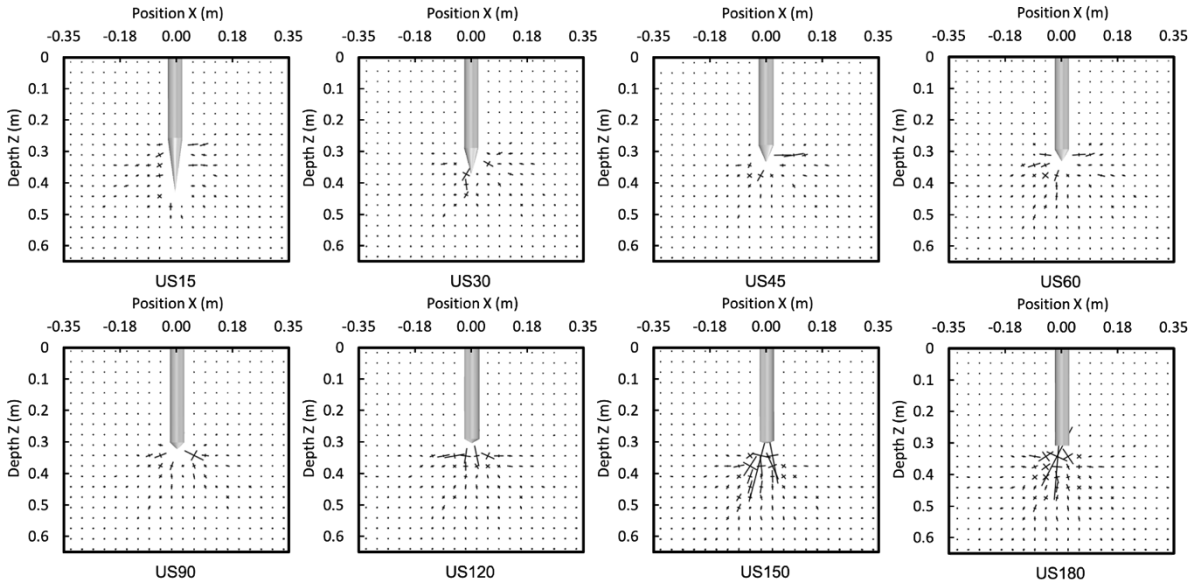

Figure 48. Stress state maps of symmetric probes in an unconfined vessel, at a Z/D ratio =7

In general, the contact forces between particles increase as the total probe apex angle increases and as the probe is penetrated further into the specimen; these contact forces between particles can be displayed through force chains. Figure 49 and Figure 50 display the force chain maps for

Z/D ratios of 2 and 7, respectively, for the unconfined specimen with probes of varying apex angles. The thickness and color of the lines correspond to the magnitude of the interparticle contact forces. As shown, the probes with acute total apex angles tend to generate force chains extending out horizontally while the probes with right and obtuse apex angles develop force chains extending downward. Additionally, the magnitude and color of the force chains indicate that the forces below the tip of the probe are greater for the right and obtuse total apex angles compared to the acute total apex angles at Z/D of 2 and 7.

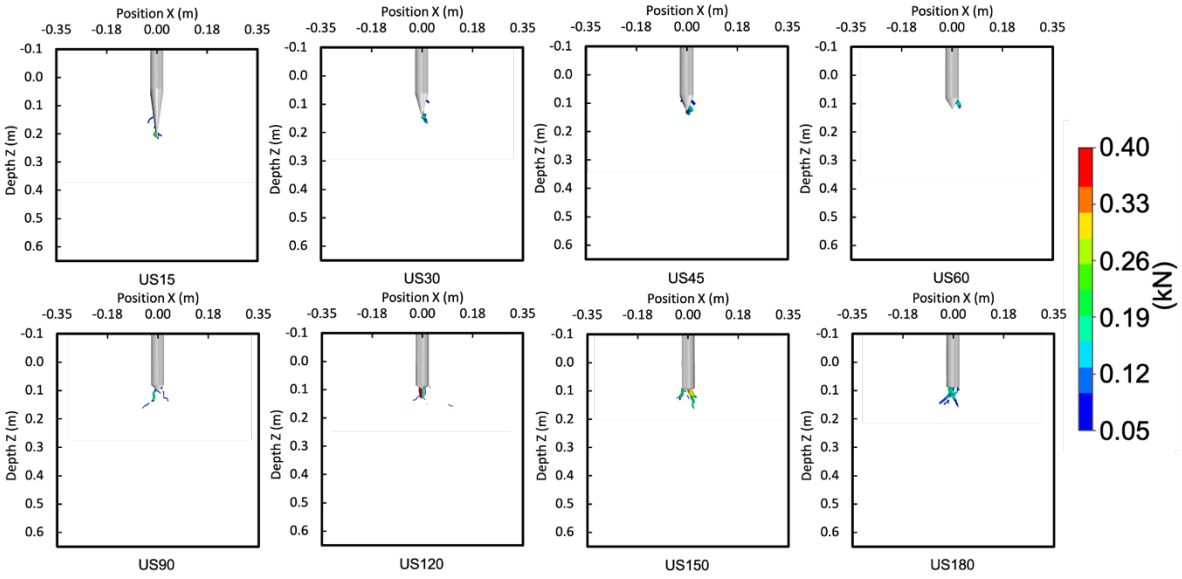

Figure 49. Force chain of symmetric probes in an unconfined vessel, at a Z/D ratio =2

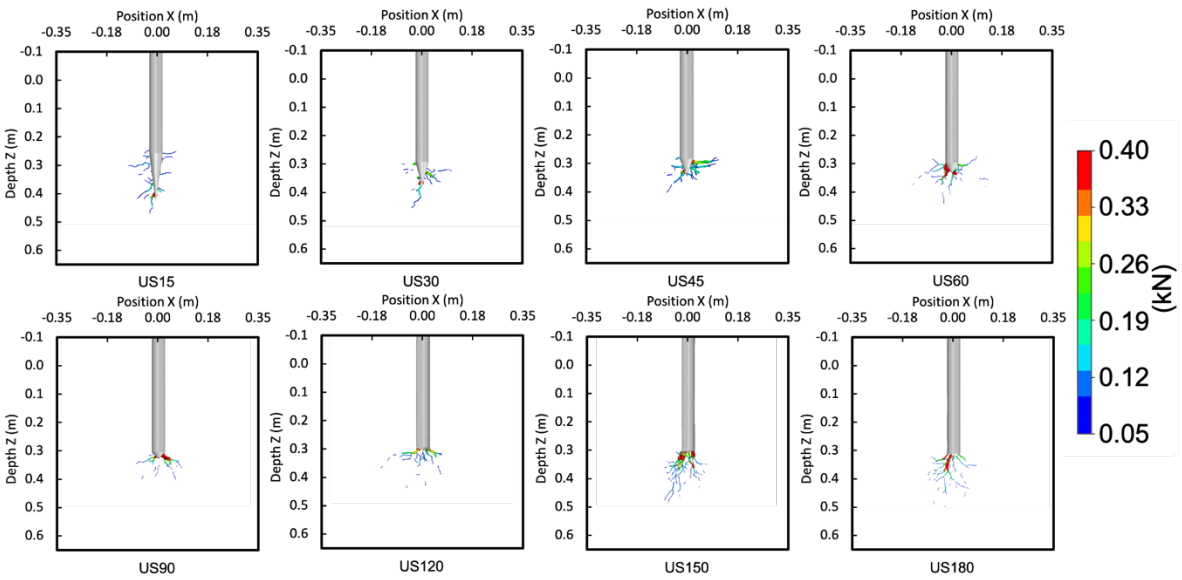

Figure 50. Force chain of symmetric probes in an unconfined vessel, at a Z/D ratio =7

Deformations of the granular assembly

Figure 51 and Figure 52 present spatial vector maps of incremental particle displacements for penetration ranges of Z/D of 0 to 2 and 5 to 7, respectively. In the figures, the magnitude of the vector as well as the color corresponds to the magnitude of displacement. Incremental displacement plots allow for the failure mode of the soil to be examined. The results show that a larger zone of soil is disturbed near the surface of the vessel as the total apex angle of the probe increases. The incremental displacement for both simulations shows that as the apex angle of the probe increases, so does the magnitude of the incremental particle displacements. As the apex angle of the probe increases, the displacements near the probe tip transition from being

perpendicular to parallel with the probe displacement, this is seen for both simulations.

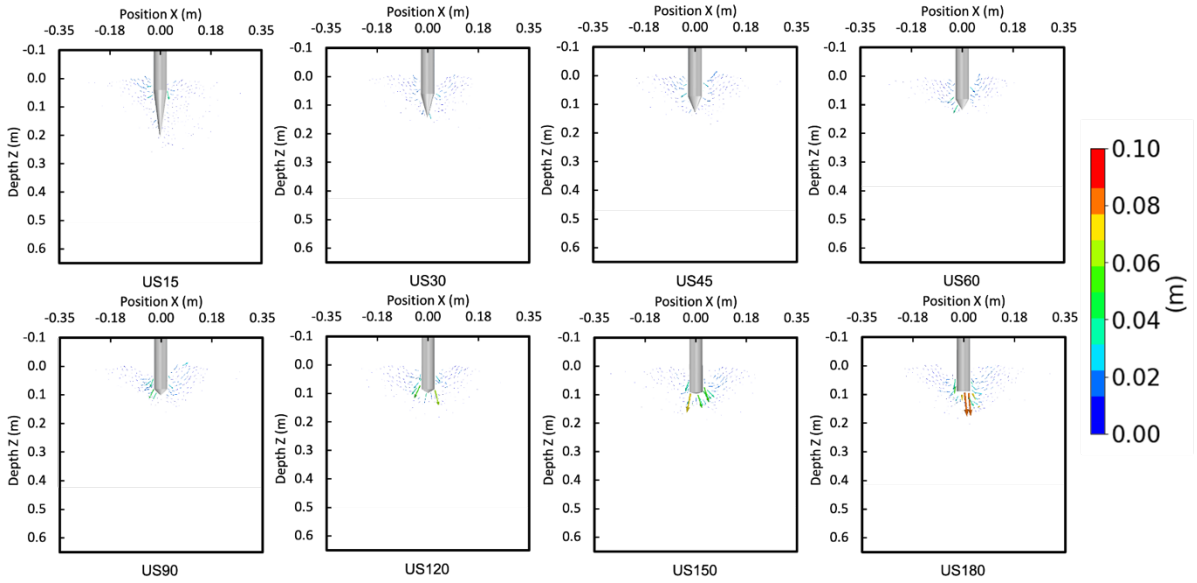

Figure 51. Incremental displacement plot of symmetric probes in an unconfined simulation, from a Z/D ratio of 0-2

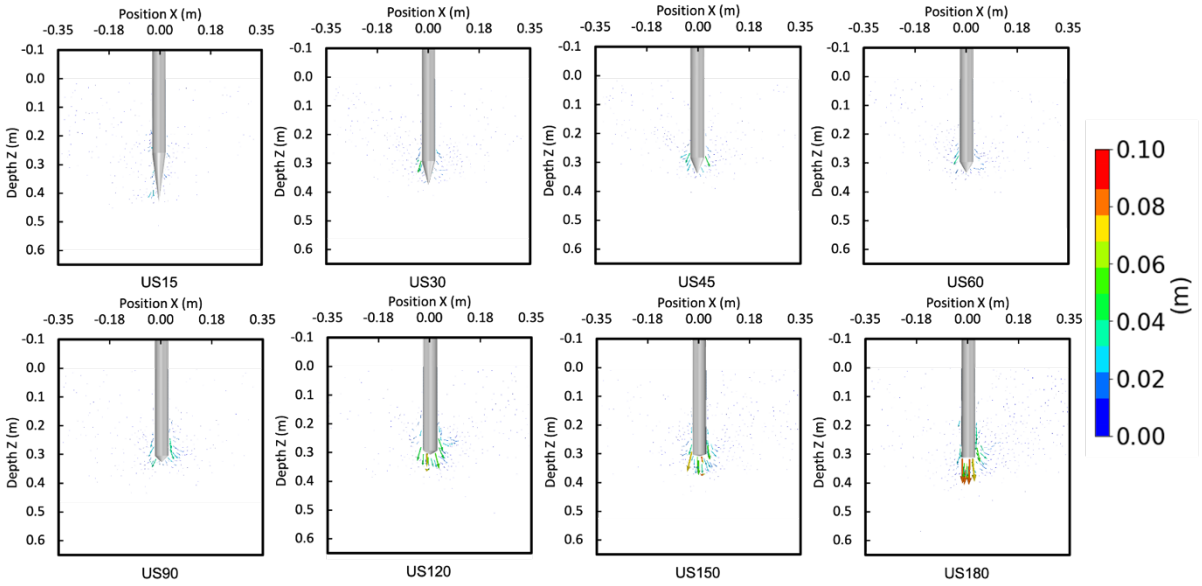

Figure 52 Incremental displacement plot of symmetric probes in an unconfined vessel from a Z/D ratio of 5-7

Maps of particle displacement allow for examination of individual soil displacements which provide insight regarding the interactions between the particles and the probe. Figure 53 and Figure 54 display the total displacement plots for Z/D ratios of 2 and 7, respectively, for an unconfined specimen with probes of varying apex angles. Total displacement indicates particle displacements from the beginning of the sounding to the specified penetration Z/D. In Figure 53 the deformations of particles up to the surface is visible, this soil heave agrees with the expected behavior of soil in the physical world and indicating that shallow penetration conditions are being properly simulated. Through examining total particle displacements, the largest magnitude of particle displacements is seen under the tip of the 180° probe. The smallest particle displacements near the probe tip are seen for the 15° and 30° probes. Similar to the incremental displacement plots, increasing soil heave is seen with increasing probe apex angle. Along with the increase in soil heave, the divot near the location of insertion of the probe tip increases with probe apex angle.

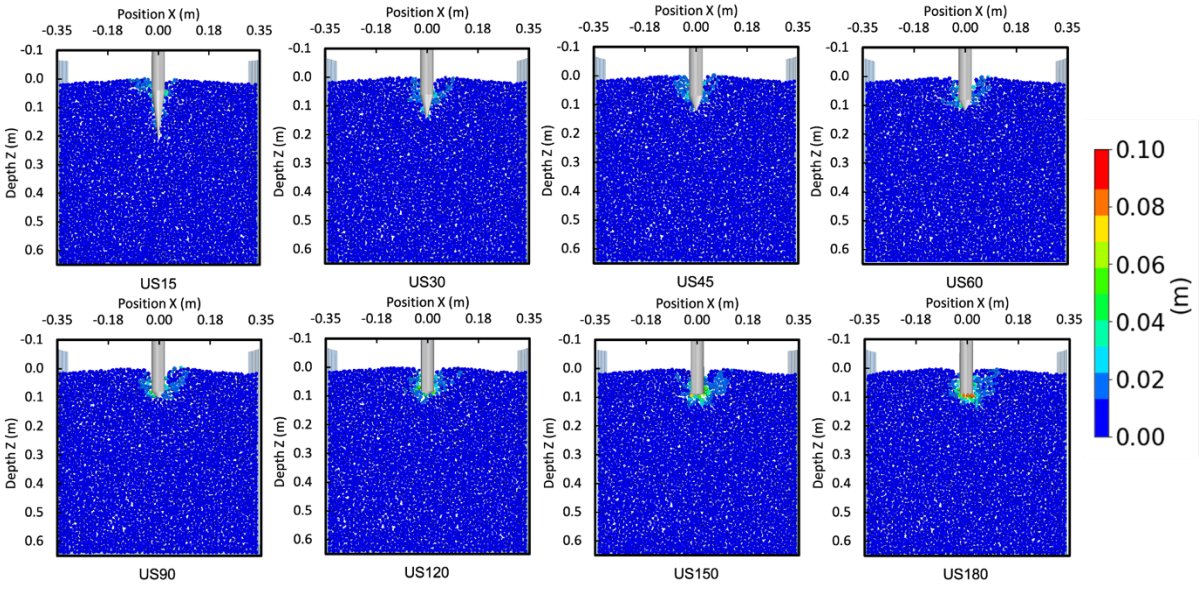

Figure 53. Total displacement plot of symmetric probes in an unconfined vessel from a Z/D ratio of 0-2

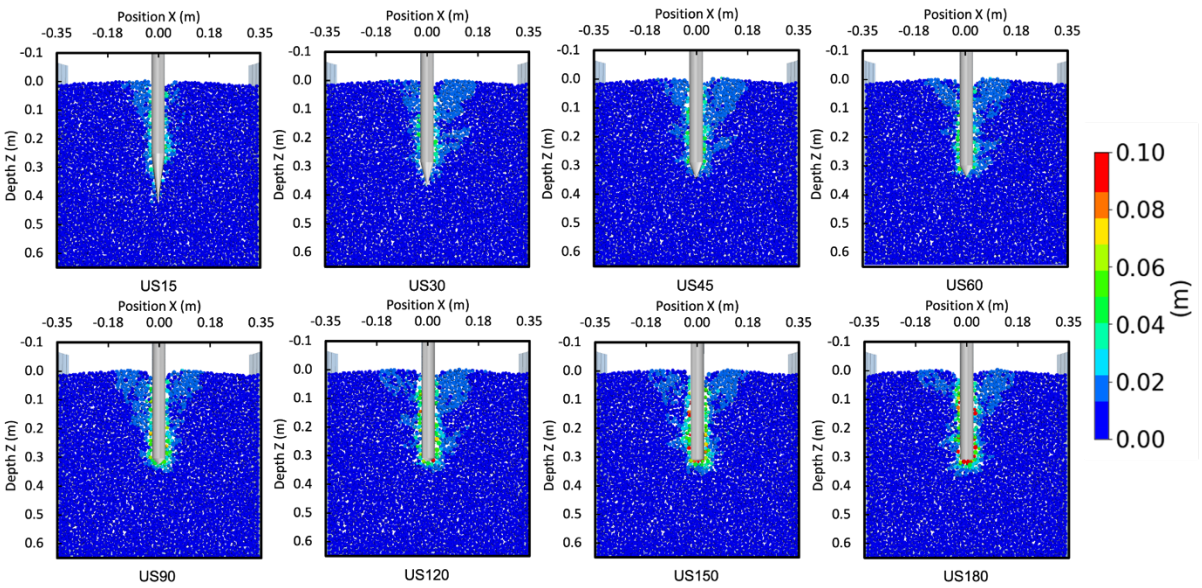

Figure 54. Total displacement plot of symmetric probes in an unconfined vessel from a Z/D ratio of 0-7

DISCUSSION

Simulations on unconfined specimens allow for the behavior of particles surrounding probes at shallow penetration depths to be investigated. All penetration depths reported for these simulations were corrected for center of surface area, as shown in Figure 26. Z/D ratios of 2 and 7 were investigated for the shallow symmetric probes. In general, the results for the Z/D of 2 and 7 are consistent with one another. The penetration resistance was observed to increase as the tip apex angle was increased. The penetration resistance may be slightly smaller for the 30° compared to that of the 15° apex angle because of either numerical variations or a significantly larger total surface area to contribute to the penetration resistance. The probes with acute total apex angles tend to push the contacting particles radially away. As the tip apex angle is increased, the more particles tend to become trapped beneath the probe, resulting in greater stresses and particle displacements at this location. The horizontal and vertical stresses below the

probes with right and obtuse total apex angles tend to be greater compared to the probe tips with acute apex angles, which is also expressed in the relative magnitudes and orientations of major and minor principal stresses.

4.1.3 MESO-SCALE AND MICRO-SCALE RESULTS OF CONFINED SPECIMENS

State of Stresses and Force Chains

Similar to the unconfined specimens, as the total probe tip apex angle increases the radial stresses of greater magnitude tend to move from the sides of the tip and shoulder to locations below the probe tip. Figure 55 and Figure 56 display radial stresses and normalized radial stresses, respectively, for the confined specimen with probes of varying apex angles. The stress is Figure 51 are normalized q_c by dividing the radial stress values by q_c value at the end of penetration. The results indicate that greater radial stresses are developed below the tip for probes with apex angles 60° and larger while probes with apex angles smaller than 60° develop smaller radial stresses near the tip and larger radial stresses around the tip shoulder.

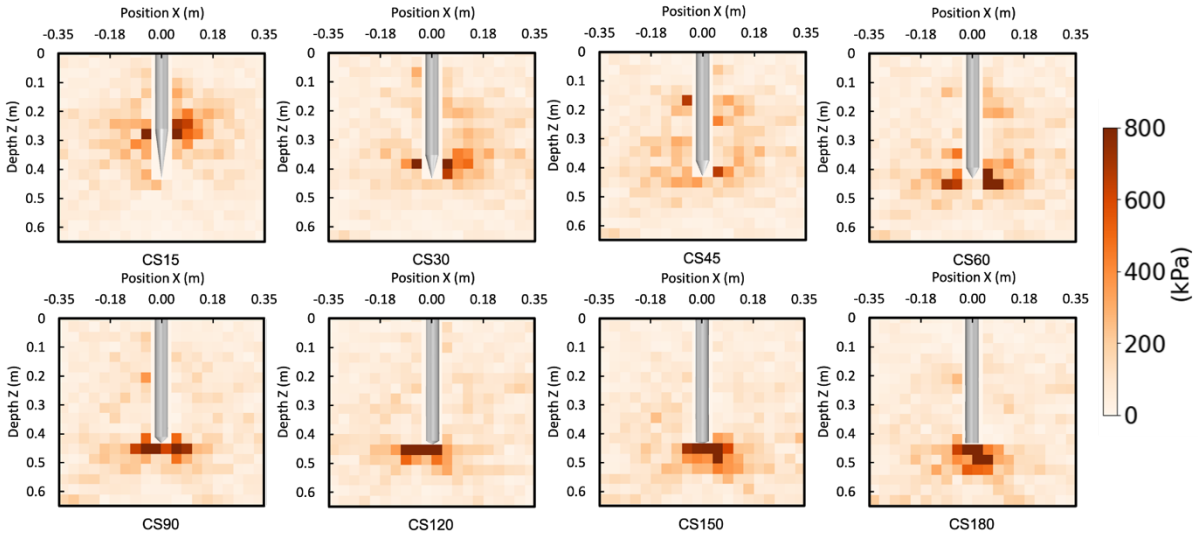

Figure 55. Radial stress of symmetric probes in a confined vessel

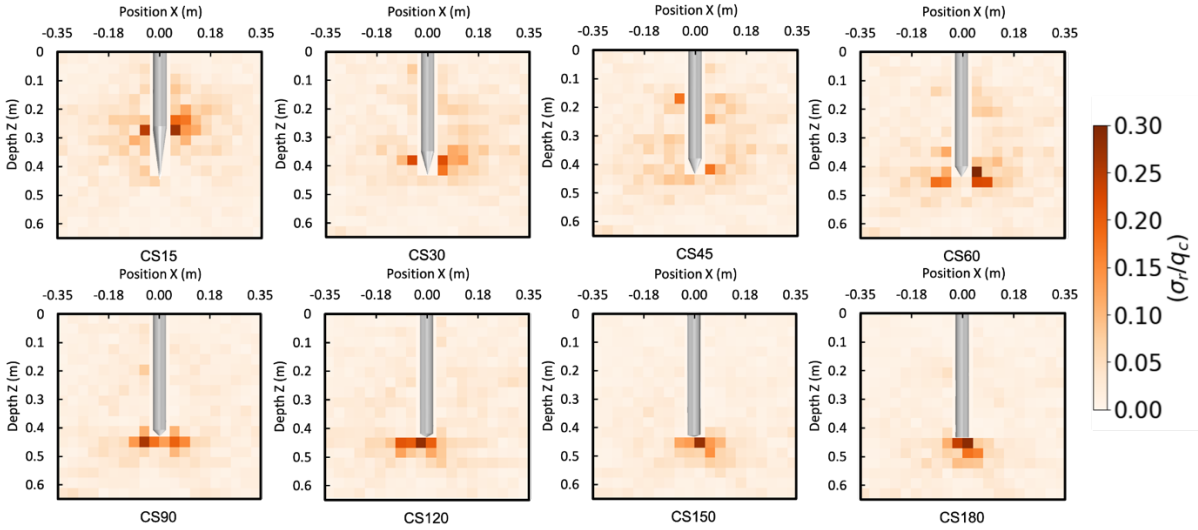

Figure 56. Normalized radial stress of symmetric probes in a confined vessel

Figure 57 and Figure 58 display vertical stress and normalized vertical stress, respectively, for the confined specimen with probes of varying apex angles. In a similar fashion as described for the radial stresses, greater magnitude of stresses are developed at the tip of the probe for the right and obtuse angles, while probes with acute angles have a smaller magnitude of vertical stress near the tip of the probe.

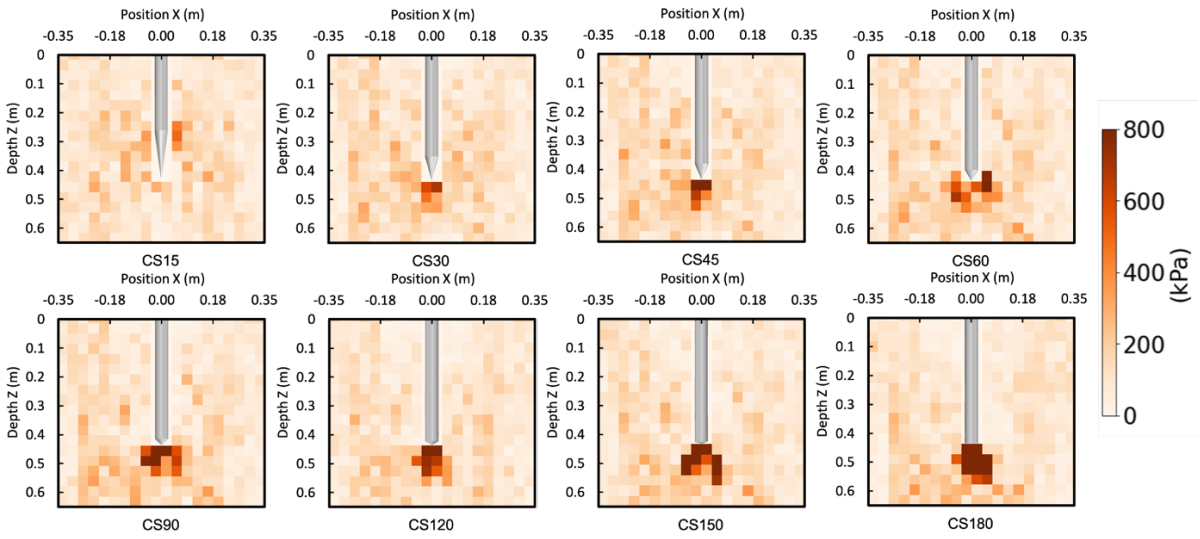

Figure 57. Vertical stress of symmetric probes in a confined vessel

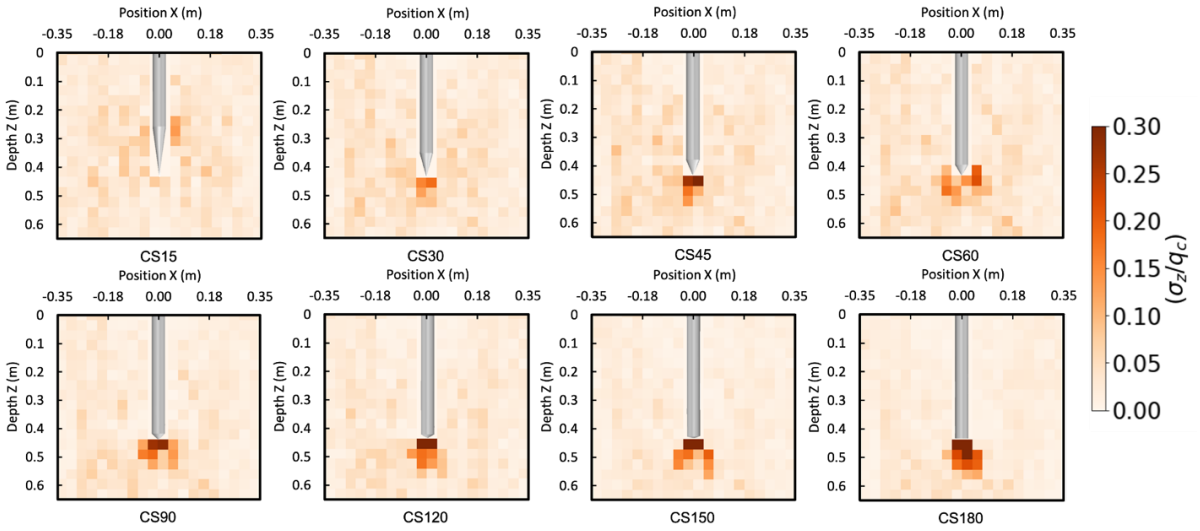

Figure 58. Normalized vertical stress of symmetric probes in a confined vessel

Probes with smaller apex angles tend to have greater radial/vertical stress ratios near the cone shoulder, while probes with larger apex angles tend to develop greater radial/vertical stresses near the probe tip, as shown in Figure 59 The normalized stress magnitude is smaller near the tip of the probe for acute angles and is slightly greater for the right and obtuse angles. For all probes the radial/vertical stress ratio increases near the probe indicating that the penetration of the probe increases radial stresses beyond what is imposed by the radial confining rings (i.e., $K_0 = 0.5$).

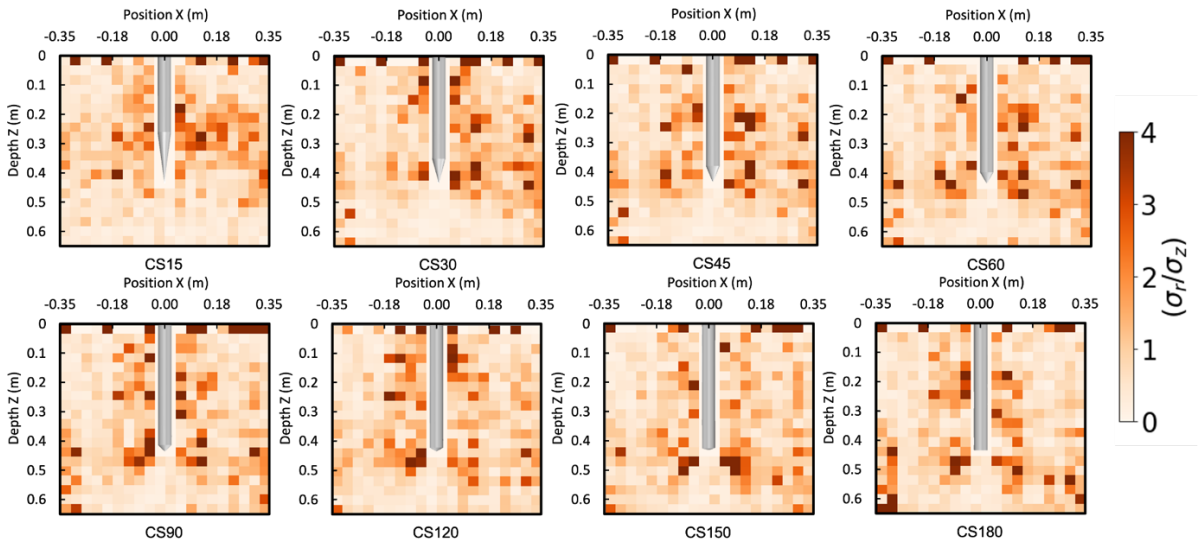

Figure 59. Normalized radial stress by vertical stress plots of symmetric probes in a confined vessel

As the probe is penetrated, the minor principal stress rotates from its initial horizontal orientation at locations around the probe shaft and tip shoulder to a more vertical orientation, indicating a change in the stress states at those locations. Figure 60 displays stress state maps for a confined specimen of probes with varying apex angles. A stress state map visually represents the relative magnitudes of the major and minor stresses as well as their orientation. This plot displays the stress state maps at the end of penetration. Within each figure, the major and minor principal stresses are divided by the same normalizing value. The plots show that the magnitude and orientation of the cross is dependent on the total probe apex angle. A greater change in principal stresses magnitude is seen near the tip of probes with total apex angles of 60° and greater. The trends observed in the stress state maps complement the behavior seen in the horizontal and vertical stress maps, with greater stresses being developed beneath the probes with the right and obtuse apex angles. The obtuse probes have larger crosses under the probe tip with their long side oriented in the vertical direction. The 15° and 30° probes have large crosses in the radial

direction near the cone shoulder, indicating that the radial stress magnitude is larger than the vertical stress magnitude.

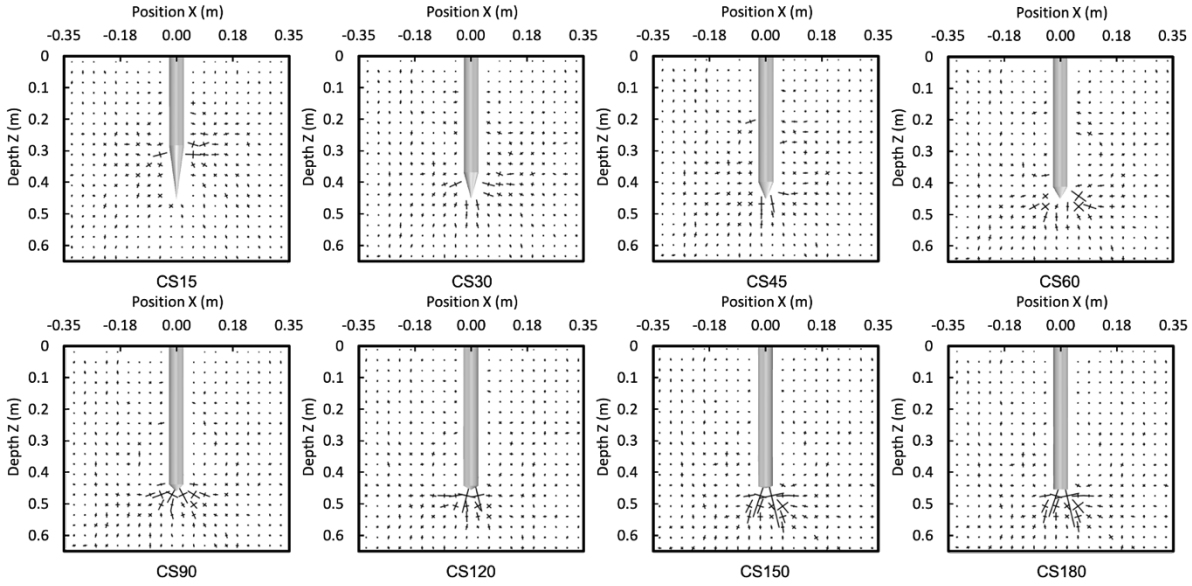

Figure 60. Stress state maps of symmetric probes in a confined vessel

In general, as the total probe apex angle increases the magnitude of the interparticle forces increase, and the forces move from being radially distributed along the tip of the probe to the forces being vertically distributed below the probe. Figure 61 displays force chains for simulations with probes of varying apex angles. Probes with 150° and 180° apex angles generate the greatest contact forces. While the right and obtuse apex angles seem to have higher contact forces near the probe tip, there are nearly almost no contact forces above 0.05 kN on the shaft of the probe. Comparatively, the probes with acute apex angles tend to have smaller contact forces near the tip and more contact forces along the probe shaft.

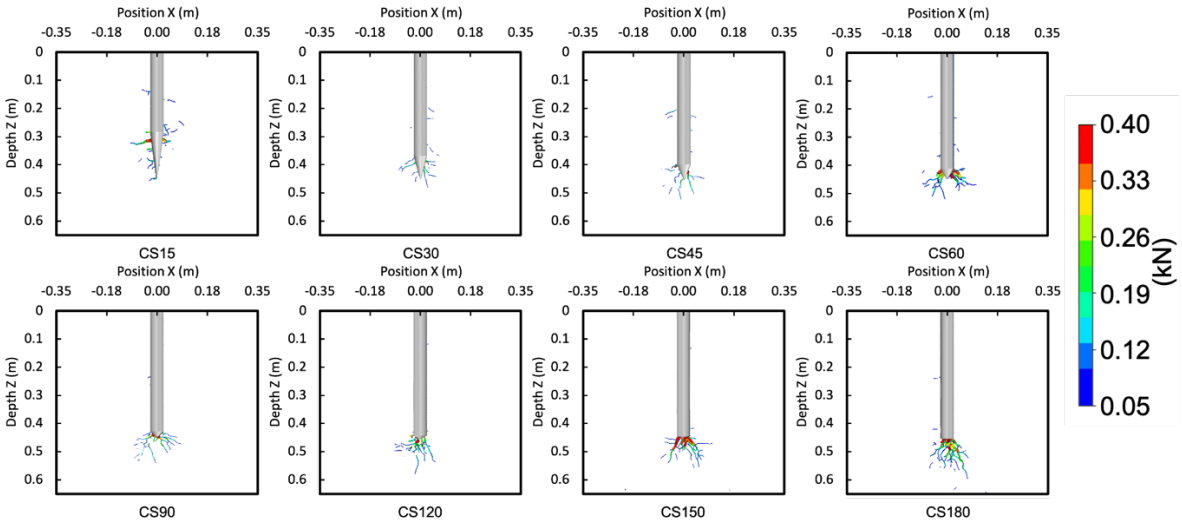

Figure 61. Force chain plots of symmetric probes in a confined vessel

Deformations of the granular assembly

The particles surrounding probes with smaller apex angles fan out to either side of the probe, and typically have small magnitudes of displacement in comparison to the particles surrounding probes with obtuse apex angles. This is similar to what was seen during the unconfined incremental displacement plots. Figure 62 displays incremental displacement plots for the simulations on confined specimens. The incremental displacements shown correspond to the last 0.088 meters (2x probe diameter) of probe penetration. The magnitude of the vector as well as the color corresponds to the magnitude of displacement. As the apex angle increases, there is a greater number of particles moving downward, rather than out to the side of the probe. The large magnitude of the displacement vector of the 150° and 180° probes indicate that particles remained trapped underneath the probe for the majority of the 0.088 meters of penetration. The behavior of the particle displacements for Figure 62 show that a deep penetration mechanisms is

achieved; the particle displacements move out to the side below the probe tip and there is no soil heave near the top of the vessel.

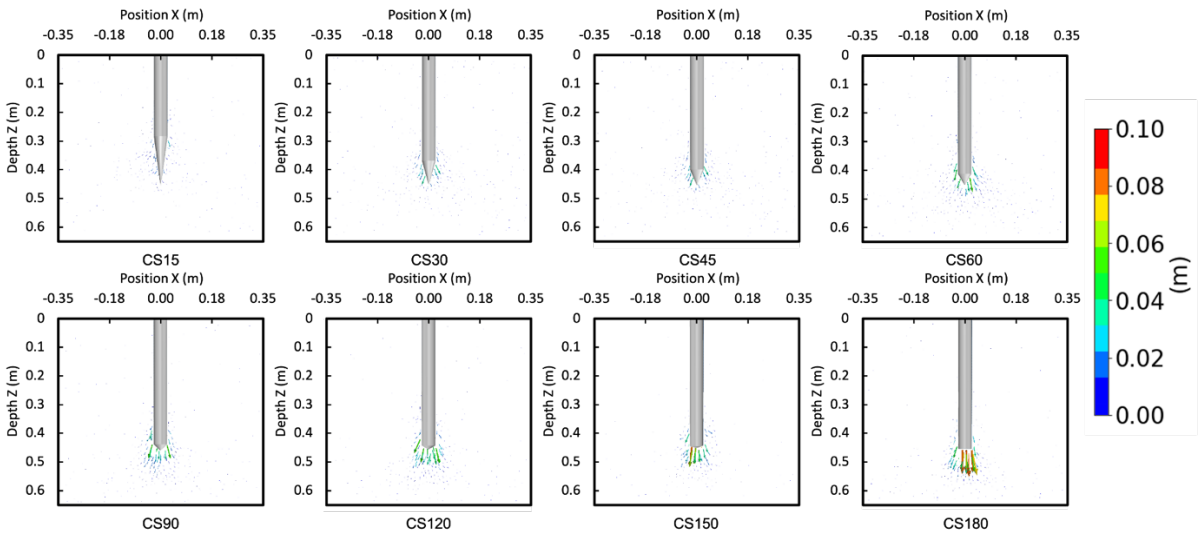

Figure 62. Incremental displacement vector plots of symmetric probes in a confined vessel

As the probe apex angle increases, the magnitude of total particle displacement increases below the probe tip. Additionally, the number of particles displaced around the probe tip increases at total probe apex angle increases. Figure 63 displays the total particle displacement at the end of 0.45 meters of penetration for the confined specimen. There is a bulb-type displacement below the probes with apex angles greater or equal than 60°, while below the tip of the 45°, 30°, and 15° probes there is minimal particle displacement. It is observed that for the 180° probe soil particles are transferred as far as 0.43 meters.

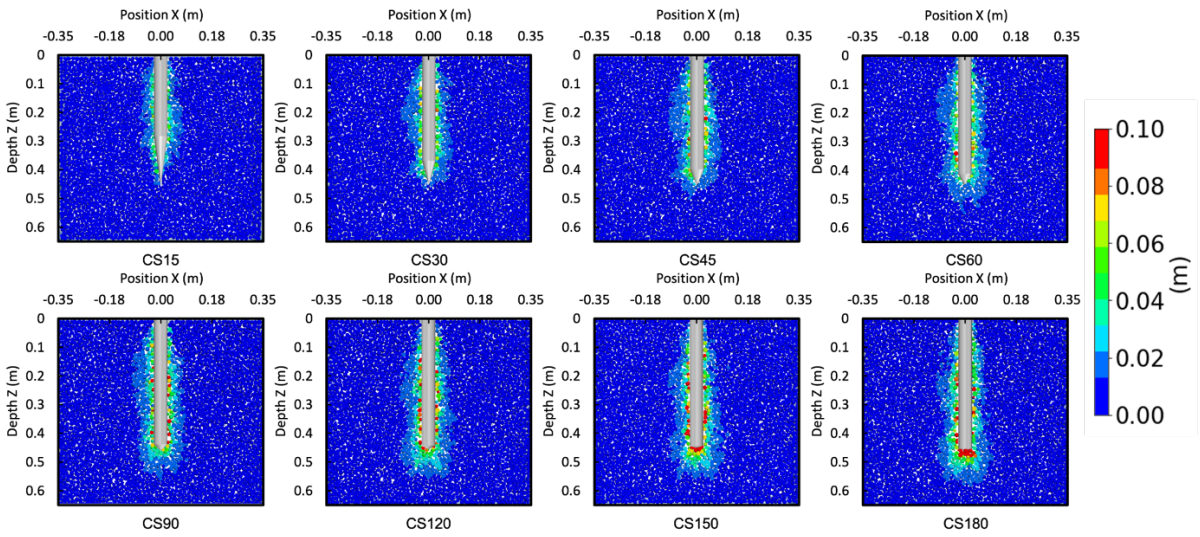

Figure 63. Total particle displacement plots of symmetric probes in a confined vessel

DISCUSSION

The larger penetration resistance mobilized by probes with greater apex angles may be explained by the failure mechanism of the soil around the probe during deep penetration. In confined specimens, the soil below the probe for the larger apex angles becomes trapped under the probe and is unable to move to the side, out of the way of the path of the probe, thus increasing contact forces, stresses, and penetration resistance. Additionally, it is seen that greater vertical stresses are developed beneath probes with greater total apex angles. However, similar magnitudes of horizontal stress were developed for the probes with different apex angles.

4.2 SIMULATIONS ON ASYMMETRIC PROBES

4.2.1 GLOBAL RESULTS

As the probes are penetrated into the unconfined specimen, the q_c value increase with depth, likely due to the increase in effective stress with depth, as shown in Figure 64. The depth shown is the figure is corrected for the center of surface area. The results indicate that q_c increases as the

total apex angle increases. In addition, as the alpha value increases from 0 to 0.5 (defined in Equation 1 and Figure 19), the penetration resistance increases. Similar to the asymmetric confined specimens, asymmetric probes with total apex angles of 30° have similar tip resistances, while the probe with a 60° total apex angle has a greater magnitude of tip resistance.

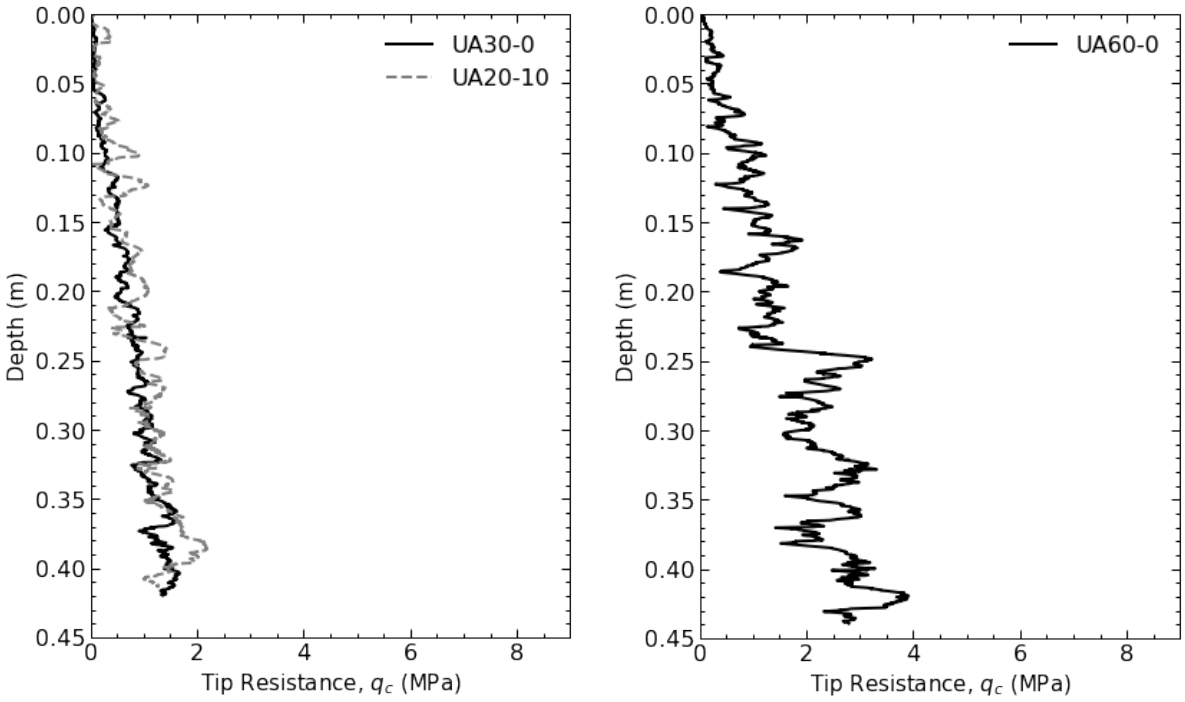

Figure 64. q_c versus depth profiles of asymmetric probes in an unconfined vessel

Similar to the simulations on symmetric probes, the penetration resistance for all probes in confined specimens increases rapidly at shallow depths, then reaches a near constant value; the near constant value is achieved due to the constant stress applied to the specimen. Figure 65 displays the tip resistance versus depth for the asymmetric probes in the confined vessel. The penetration resistances of asymmetric probes with total apex angles of 30° have similar tip resistances, indicating a negligible effect of the alpha parameter. The probe with a 60° total apex angle generates much greater magnitudes of tip resistance. In addition, the tip resistance reaches

a constant value sooner for the tips with a total angle of 60°, likely because it takes a shorter distance for the entire probe to be embedded in the specimen.

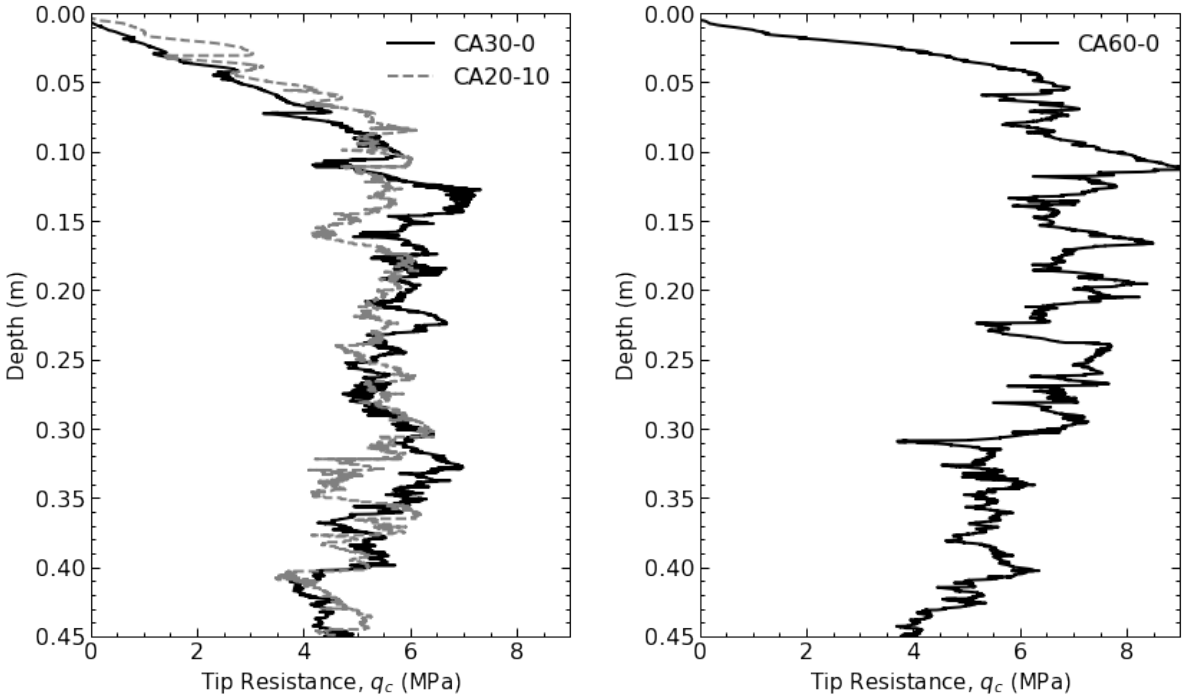

Figure 65. q_c versus depth profiles of asymmetric probes in a confined vessel

Horizontal and vertical forces on asymmetric probe tips

Vertical and horizontal and forces were measured on the asymmetric probe tips throughout the penetration process. Figure 66 and Figure 67 display vertical tip resistance versus depth for simulations on unconfined and confined specimens, respectively. These force measurements map directly with the q_c profiles presented in Figure 64 and Figure 65. The horizontal forces allow for the balance of forces on either side of the probe to be evaluated, allowing for insight into the magnitude of bending moment that would be imposed on the tips. This is important because the probe in DEM is modeled as a rigid body, meaning that the probe itself will not bend or deform due to unbalanced forces applied to it. Figure 66 and Figure 67 display horizontal unbalanced tip

resistance versus depth for the unconfined and confined asymmetric specimens, respectively. The unbalanced horizontal force is defined as the absolute value of the difference in horizontal forces acting on the sides for each probe. The unbalanced horizontal forces are displayed for both the X and Y planes. The X plane is defined as the plane with the angled sides of the asymmetric tips while the Y plane is defined as the plane with the vertical sides of the tip. Since the 30°- 0° probe only has one angled tip the values are only of the recorded 30° angled side. As shown, the horizontal forces are smaller for the probe sides that have smaller half-apex angles, leading to the unbalanced Q_x forces shown in Figures 63 and 64. For all the probes, the unbalanced Q_y values are close to zero. The closer the symmetry of the probe, the closer the probe is to having balanced horizontal forces.

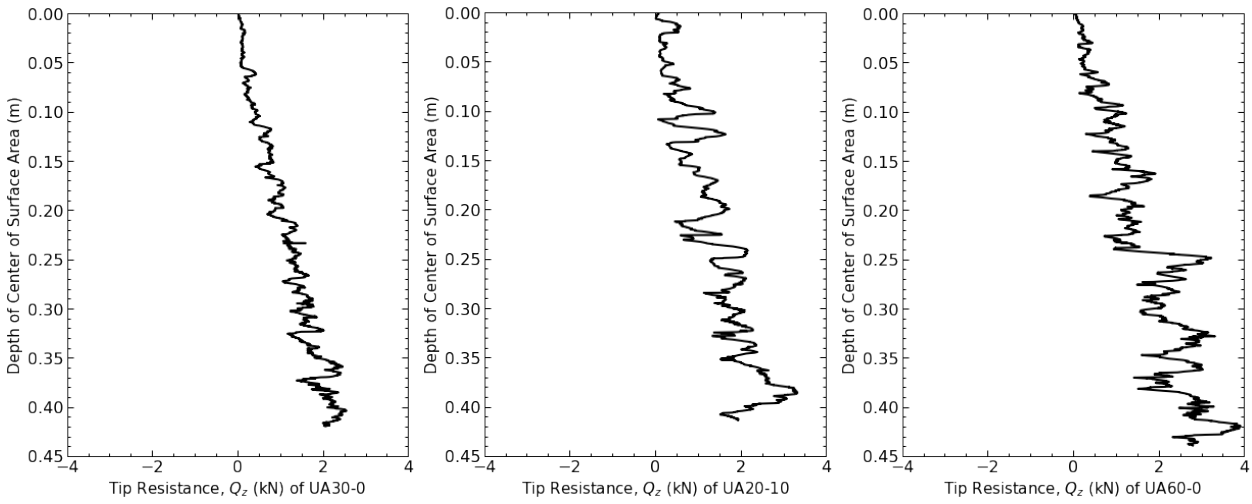

Figure 66. Vertical tip resistances, Q_z, versus depth of center of surface area of asymmetric probes in an unconfined vessel

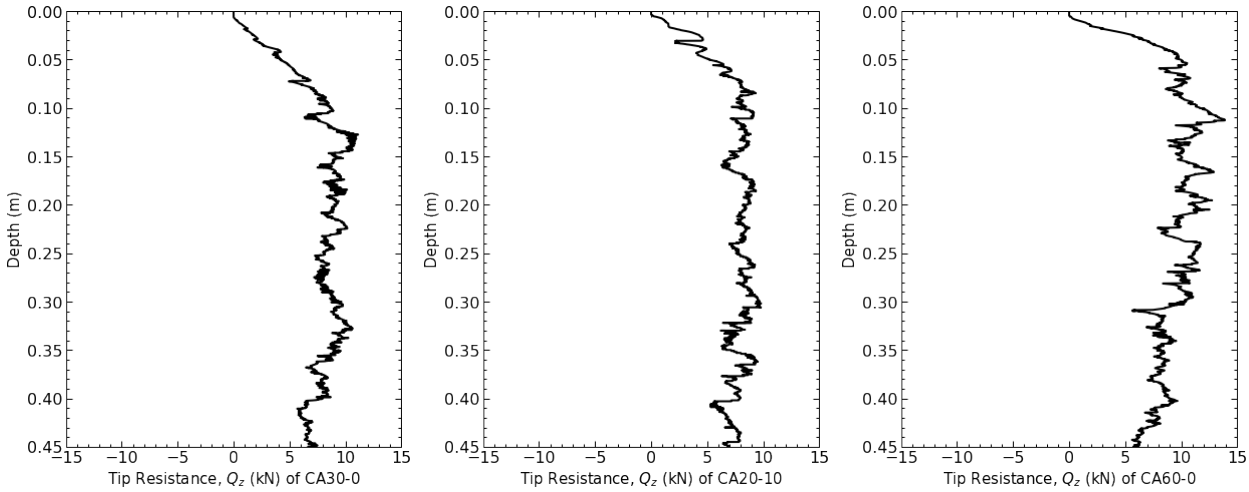

Figure 67. Vertical tip resistances, Q_z, versus depth of asymmetric probes in a confined specimen

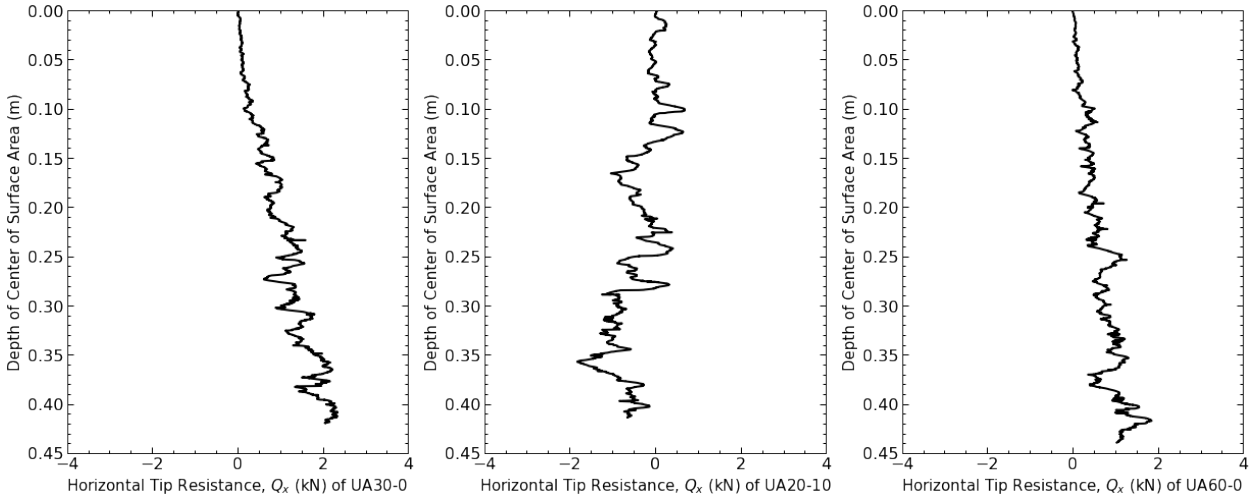

Figure 68. Horizontal tip resistances, Q_x, versus depth of center of surface area of asymmetric probes in an unconfined specimen

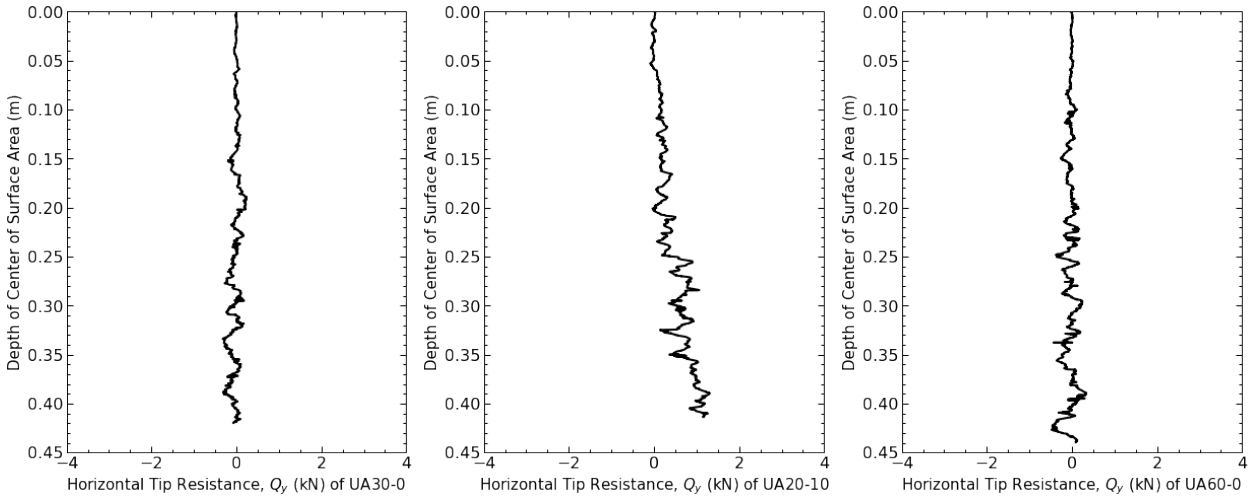

Figure 69. Horizontal tip resistance, Q_y, versus depth of center of surface area of asymmetric probes in an unconfined vessel

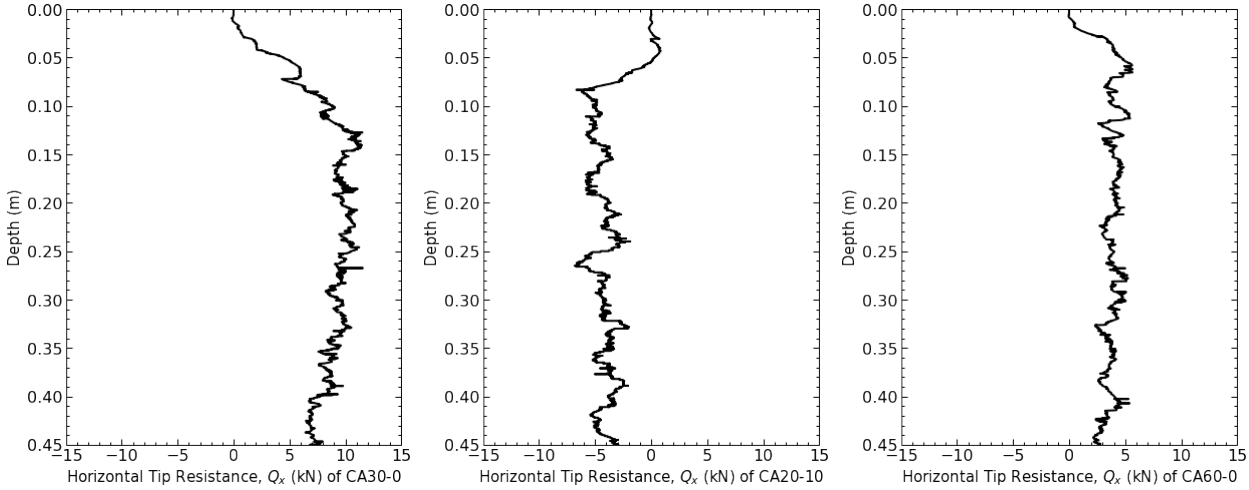

Figure 70. Horizontal tip resistances, Q_x, versus depth of asymmetric probes in a confined vessel

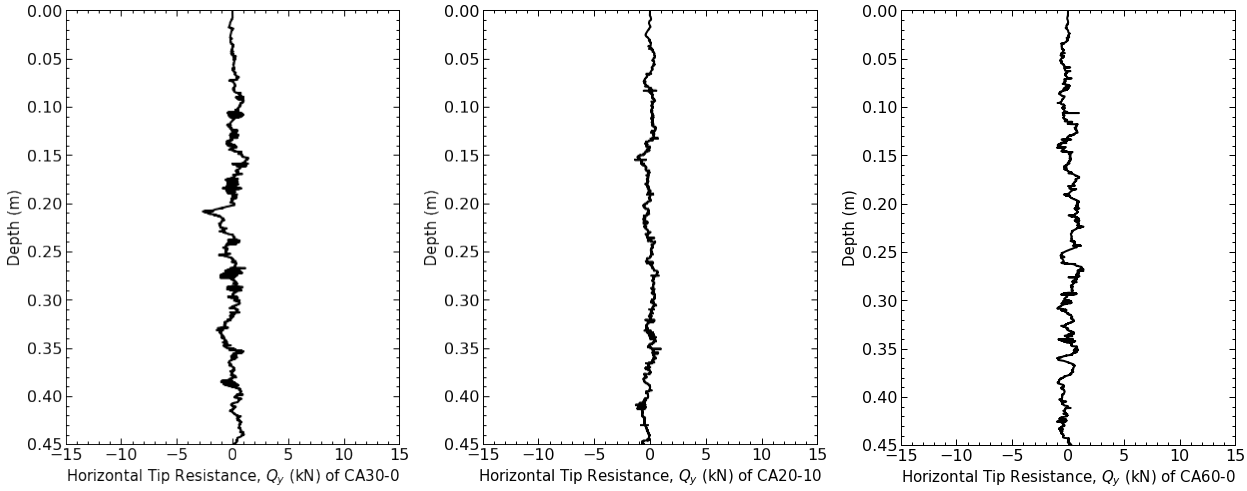

Figure 71. Horizontal tip resistances, Q_y, versus depth of asymmetric probes in a confined vessel

Penetration resistance as a function of apex angle

A lower average tip penetration resistance is seen for the symmetric probes compared to the asymmetric probe tips for the unconfined specimens. Figure 72 plots the average tip penetration resistance over 0.044 m, or 1 probe diameter, at Z/D ratios of 2 and 7, against total apex angle. The symmetric probe produces the smallest overall average tip penetration resistances for both Z/D ratios of 2 and 7. A probe with an alpha value of 1 produces the smallest penetration resistance, followed by the probes with an alpha value of 0, and the highest penetration resistance is mobilized by probes with an alpha value of 0.5 for the 30° total apex angle probes.

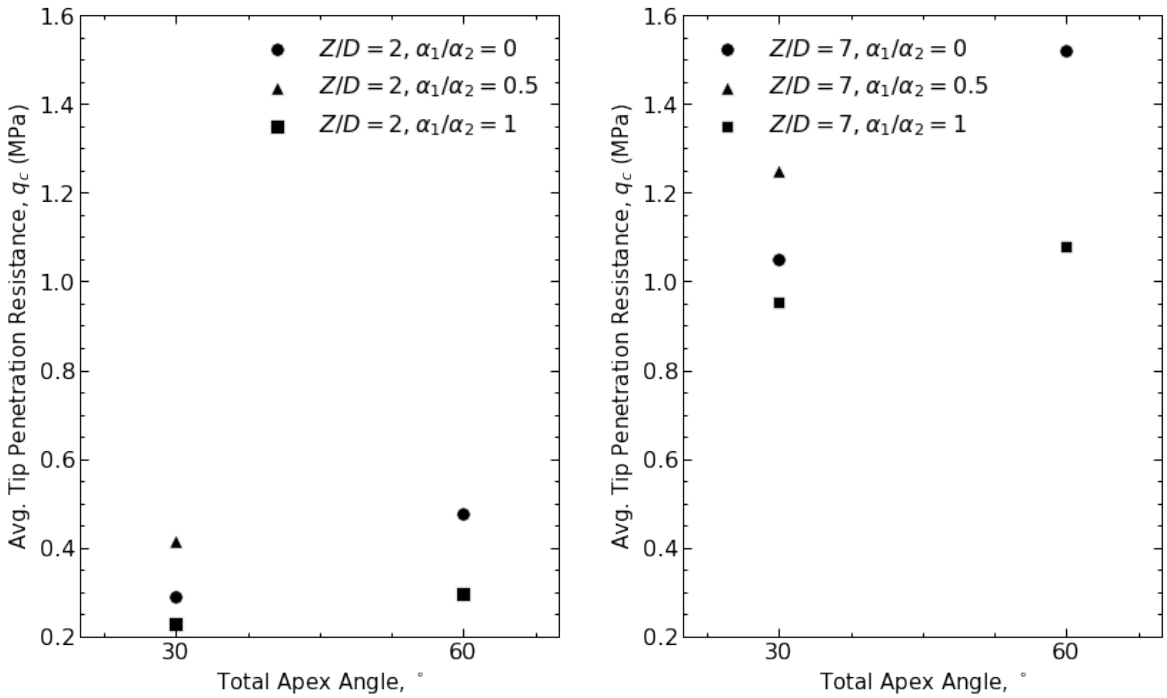

Figure 72. Tip penetration resistance versus total apex angle for varying alpha values of probes in unconfined vessels at Z/D ratios= 2 and 7, respectively

For the confined specimens, the symmetric tip produces an overall smaller average tip penetration resistance compared to the asymmetric probe tips, in a similar fashion as described for the unconfined specimens. Figure 73 plots the average tip penetration resistance over the last

0.044 m, or 1 probe diameter of penetration, against total apex angle for confined specimens. Different alpha values represent the shape of the probe tip and is described in *Equation (1)* and Figure 22. The probes with an alpha value of 1 produces the lower penetration resistance, followed by the probes with an alpha value of 0, while the probes with an alpha value of 0.5 for 30° total apex angle generated the greatest q_c values.

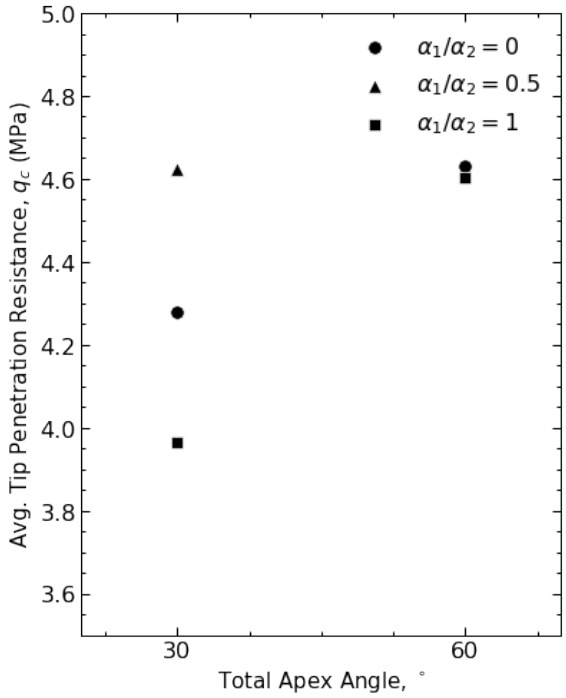

Figure 73. Tip penetration resistance versus total apex angle for varying alpha values of probes in a confined vessel

4.2.2 MESO- AND MICRO-SCALE RESULTS OF UNCONFINED SPECIMENS

Figure 74 displays the individual particle displacements for the asymmetric probes in a confined vessel at the end of 0.45 meters of penetration. This illustrates the particle displacements by varying the color of the particle to represent the magnitude of the particle displacement. As shown, the majority of the particle displacements occur on the side of the probe with the largest half-angle. Particles near the tip of the probes with total apex angles of 30° tend to be pushed off

to the side of the probe, while particles near the tip of the probe with half apex angles of 60° and 0° are pushed downward, beneath the probe. This concentration of displacements below the probe may contribute to a greater development of stresses below the probe, leading to a greater tip penetration resistance overall. This greater development of stresses below the probe can be seen in Figure 75. The force chain maps illustrate greater forces on the side of probe with the largest half apex angle. The largest force chains are seen for the probe with half apex angles of 60° and 0. Figure 75 displays the force chains developed for the asymmetric probes at the end of penetration in the unconfined vessel. These observations are in close agreement with the particle displacements shown in Figure 74.

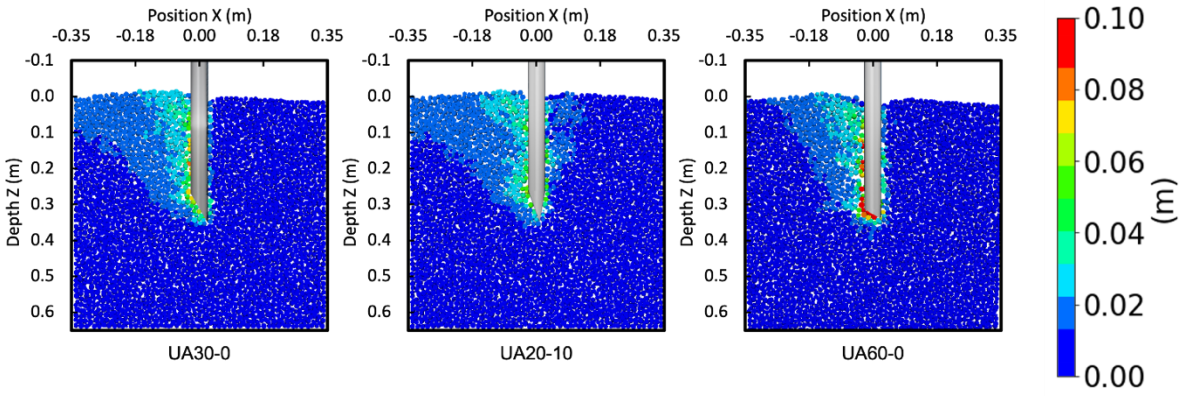

Figure 74. Total particle displacements of asymmetric probes in an unconfined vessel at a Z/D ratio = 7

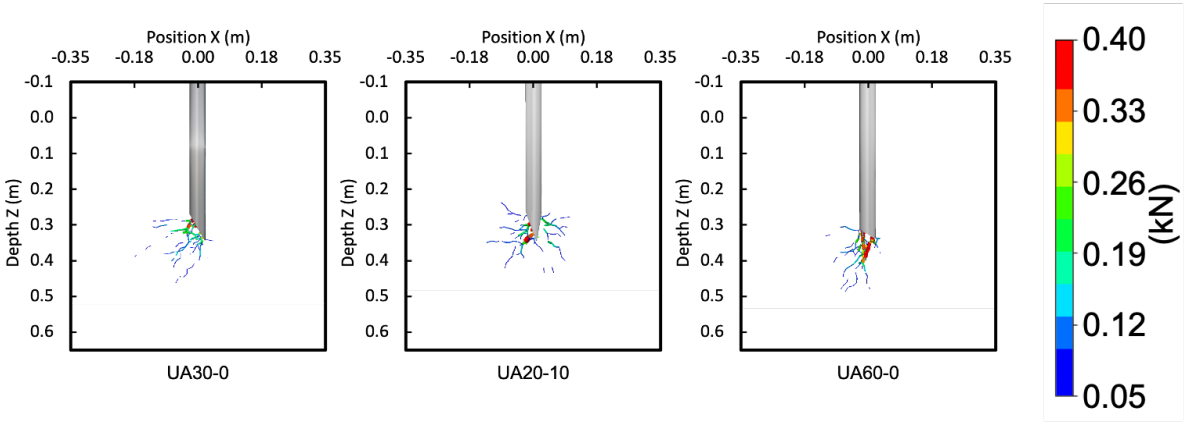

Figure 75. Force chain of unconfined asymmetric probes in an unconfined vessel at a Z/D ratio = 7

DISCUSSION

Larger displacements and stresses are developed on the side of the probe with the largest half apex angle. Similar to the behavior of the symmetric probes, the probes with apex angles of 30°, for an alpha value of 0.5 or 0, produced a smaller penetration resistance compared to the probe with an apex angle of 60° with an alpha value of 0.

4.2.3 MESO- AND MICRO-SCALE RESULTS OF CONFINED SPECIMENS

Figure 76 displays the individual particle displacements for the simulations with asymmetric probes in a confined vessel at the end of 0.45 meters of penetration. Greater particle displacements are developed on the side of the probe with the larger half apex angle. Larger magnitude displacements are developed for the probe with half apex angles of 60° and 0° with particles near the base of the probe being displaced downward. This downward displacement of particles may contribute to the trapping of particles under the probe, which may lead to greater stresses generated at the tip of the probe. The probe with half apex angles of 30° and 0° has minimal particle displacements on the 0° side of the probe. Figure 77 displays the force chains developed at the end of penetration in the confined vessel. As shown, the force chains illustrate

greater forces developed on the side of the tip with a greater half apex angle for all the probes, in a similar fashion as shown for the simulations on the unconfined specimens. These results are in agreement with the particle displacement maps shown in Figure 71.

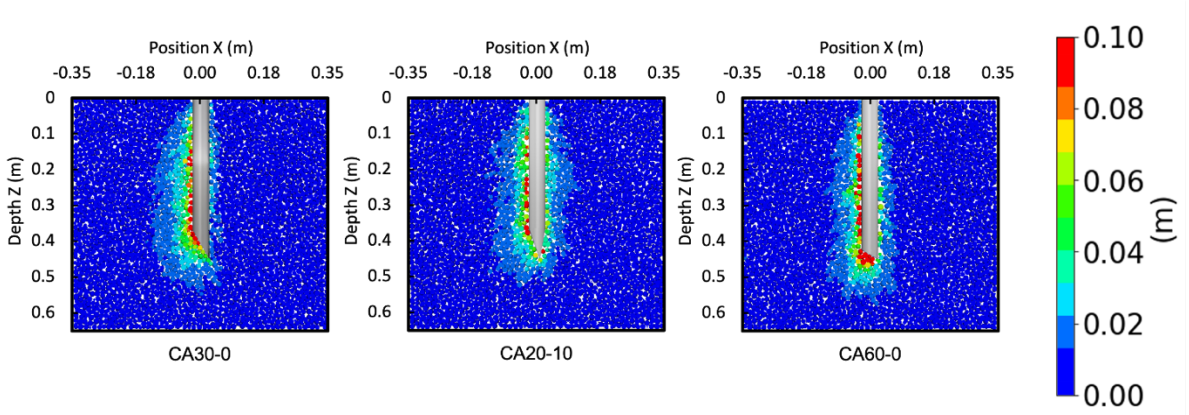

Figure 76. Particle displacement plots of asymmetric probes in a confined vessel

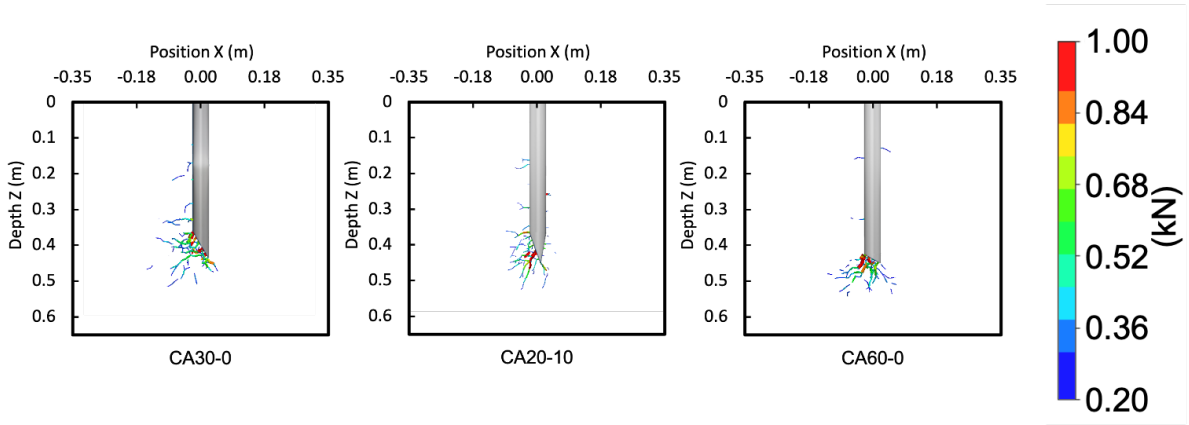

Figure 77. Force chain of asymmetric probes in a confined vessel

DISCUSSION

The behavior of the asymmetric probes is similar during both confined and unconfined penetration. Greater displacements and stresses are developed on the side of the probes with the largest half apex angle. Similar to the behavior of the symmetric probes, the probes with an apex angle of 30°, for an alpha value of 0.5 or 0, produces a lower penetration resistance compared to

the 60° probe with an alpha value of 0. Overall, the use of an asymmetric tip provides an increase in penetration resistance.

5 CONCLUSIONS

This research investigated bio-inspired methods to reduce penetration resistance for geotechnical soil exploration and construction activities using DEM simulations. It was hypothesized that altering apex angle and probe symmetry may have an effect on tip penetration resistance. A testing plan was developed focusing on altering two main parameters: apex tip geometry, consisting of the cone apex angle as well as the tip symmetry, and the confinement conditions imposed on the soil specimen. Confinement conditions imposed on the specimen were meant to simulate shallow and deep soil behavior. Performing and analyzing the results of these simulations has led to the following main takeaways:

- Reduction of the conical tip apex angle can reduce the penetration resistance mobilized in sandy soils. However, the results imply that there is not a simple relationship between penetration resistance and tip apex angle because other factors such as the confining stresses and the soil type and properties likely play an important role in this relationship.
- For the simulations performed in unconfined specimens, the smallest penetration resistance was generated by the symmetric probe with a 30° apex angle. For the simulations ran in confined specimens, the smallest penetration resistance was generated by the symmetric probe with a 15° apex angle.
- The reduction in penetration resistance for probes with smaller apex angle was more pronounced in the unconfined specimens, which model shallow penetration conditions. The penetration resistance for a probe with a 30° tip was 35% smaller than for a 180° (flat) tip for the unconfined simulations, at a Z/D = 7; for the confined simulations, this reduction was 29%.

- Symmetric probes with smaller apex angles developed greater radial and vertical soil stresses at locations around the sides of the tip and at the tip shoulder, while probes with larger apex angles develop greater radial and vertical soil stresses directly below the probe's tip. The same trends were observed for the induced interparticle contact forces.
- Under unconfined conditions, symmetric probes generate greater soil heave with increasing probe tip apex angle. Additionally, as apex angle increases, larger particle displacements below the tip of the probe are seen.
- Under confined conditions, the penetration of symmetric probes generate greater magnitude of particle displacements below the tip of the probe with increasing total apex angle.
- The stress state plots indicate that as the total probe apex angle of the symmetric probe increases, the magnitude of the interparticle forces increases, and the forces move from being radially distributed along the tip of the probe to the forces being vertically distributed below the probe.
- Large stresses are generated during penetration of the symmetric probes with greater apex angles, particularly at locations beneath the tip. This is likely due to particles becoming "trapped" underneath the probe as it is inserted into the vessel.
- Asymmetric probe tips resulted in either increases or negligible changes in the mobilized penetration resistance. Symmetric probes mobilized the smallest penetration resistance, followed by the most asymmetric probes, while the probe with an alpha factor of 0.5 mobilized the greatest penetration resistance.
- Greater particle displacements and force chains of larger magnitude are observed on the side of asymmetric probes with the larger half-apex angle, indicating a greater

development of stresses. This behavior was seen for both confined and unconfined conditions.

It is noted here typical ranges of penetration resistance for varying conditions to provide context on the significance of differences observed in q_c values.:

- As CPT moves from penetrating sand to clay q_c can vary over 3 orders of magnitude (Robertson 2013).
- As the relative density of a sand increases from 40% to 90% the magnitude of penetration resistance can increase by a factor of 3.5 to 1.7, respectively for uncemented and unaged quartz sands (Robertson and Campanella 1983).
- As the OCR of a clay increases from 1 to 8 the penetration resistance can increase by a factor of 4.7 to 9 depending on clay type (Drnevich, Mayne, and Kemper 1988).
- As overburden stresses vary from a 50 kPa to 400 kPa in uncemented and unaged quartz sands the penetration resistance of a CPT increase by a factor of 4.3 to 1.7, respectively (Robertson and Campanella 1983; Baldi et al. 1992).

RECOMMENDATIONS FOR FUTURE RESEARCH

Altering apex angle to reduce penetration resistance has many possible benefits within geotechnical engineering applications. With regards to in-situ testing, a reduction in penetration resistance will allow for the use of smaller rigs to complete soundings, thus reducing financial and environmental impacts of soil exploration. In addition, the use of smaller rigs can reduce challenges associated with accessing sites in congested urban or forested areas or sites with limited access roads. DEM proved useful in modeling soil behavior and isolating probe geometry effects; therefore, it can be a useful tool in the investigation of additional bio-inspired strategies, this will be elaborated further below. The following provides recommendations for further research:

- Employ a lower coefficient of friction for the sleeve of the probe to allow for more realistic sleeve resistance measurements. The friction coefficient of 0.3 used in this study produces larger sleeve resistance values compared to what would be seen for CPT probes used in the field and sandy soils. This change would allow for both tip penetration resistances and sleeve resistances to be evaluated.
- Test additional asymmetric tip geometries. Only three asymmetric geometries were simulated in this research. Testing additional geometries would allow for relationships between alpha value and penetration resistance to be better defined.
- Perform simulations on probes with other shapes or motion sequences not evaluated in this research to explore whether these can result in further reductions in tip resistances. Such simulations could consider barbed geometries, use of reciprocal motion, or a combination of various bio-inspired strategies.

- Evaluate the effect of conical tip apex angle in sandy soil of varying densities and in different soil types, including clays and silts.
- Evaluate the effect of soil behavior of various tip geometries under greater confining stresses and evaluate the influence of the tip apex angle on the crushing of particles.
- Perform experimental tests using the geotechnical centrifuge or field tests in a site with uniform or known soil properties to verify the trends reported in this thesis (Chen et al. 2022).

REFERENCES

Ai, Jun, Jian-Fei Chen, J. Michael Rotter, and Jin Y. Ooi. 2011. "Assessment of Rolling Resistance Models in Discrete Element Simulations." *Powder Technology* 206 (3): 269–82. https://doi.org/10.1016/j.powtec.2010.09.030.

Arroyo, M., J. Butlanska, A. Gens, F. Calvetti, and M. Jamiolkowski. 2011. "Cone Penetration Tests in a Virtual Calibration Chamber." *Géotechnique* 61 (6): 525–31. https://doi.org/10.1680/geot.9.P.067.

Baldi, G., R. Bellotti, V. Ghionna, M. Jamiolkowski, and E. Pasqualini. 1992. "Design Parameters for Sands from CPT." *Proceedings of the Second European Symposium on Penetration Testing* 2: 425–38.

Baligh, M.M., and R.F Scott. 1975. "Quasi Static Deep Penetration in Clays." *ASCE* 101 (No. GT11): 1119–33.

Bizzarro, Joseph J., Ashley N. Peterson, Jennifer M. Blaine, Jordan P. Balaban, H. Gary Greene, and Adam P. Summers. 2016. "Burrowing Behavior, Habitat, and Functional Morphology of the Pacific Sand Lance (Ammodytes Personatus)." *Fishery Bulletin* 114 (4): 445–60. https://doi.org/10.7755/FB.114.4.7.

Browning, John. 2005. "Cone Tip Angle Effects on Cone Penetration Testing." Master's Thesis, Raleigh: North Carolina State University.

Butlanska, Joanna, Marcos Arroyo, Antonio Gens, and Catherine O'Sullivan. 2014. "Multi-Scale Analysis of Cone Penetration Test (CPT) in a Virtual Calibration Chamber." *Canadian Geotechnical Journal* 51 (1): 51–66. https://doi.org/10.1139/cgj-2012-0476.

Cerkvenik, Uroš, Bram van de Straat, Sander W. S. Gussekloo, and Johan L. van Leeuwen. 2017. "Mechanisms of Ovipositor Insertion and Steering of a Parasitic Wasp."

Proceedings of the National Academy of Sciences 114 (37): E7822–31. https://doi.org/10.1073/pnas.1706162114.

Chang, Ching, and Sao-Jeng Chao. 1994. "Discrete Element Analysis for Active and Passibe Pressure Distribution on a Retaining Wall."

Chen, Yuyan, Ali Khosravi, Alejandro Martinez, and Jason DeJong. 2021. "Modeling the Self-Penetration Process of a Bio-Inspired Probe in Granular Soils." *Bioinspiration & Biomimetics*, April. https://doi.org/10.1088/1748-3190/abf46e.

Chen, Yuyan, Ali Khosravi, Alejandro Martinez, Jason DeJong, and Dan Wilson. 2020. "Analysis of the Self-Penetration Process of a Bio-Inspired In Situ Testing Probe." In *Geo-Congress 2020*, 224–32. Minneapolis, Minnesota: American Society of Civil Engineers. https://doi.org/10.1061/9780784482834.025.

Chen, Yuyan, Alejandro Martinez, and Jason DeJong. 2022. "Alteration of the Stress State around a Bio-Inspired Probe Enables Self- Penetration."

Ciantia, M. O., C. O'Sullivan, and R. J. Jardine. 2019. "Pile Penetration in Crushable Soils: Insights from Micromechanical Modelling." *Proceedings of the XVII European Conference on Soil Mechanics and Geotechnical Engineering*, no. Geotechnical Engineering, foundation of the future: 5247–66. https://doi.org/10.32075/17ECSMGE-2019-1111.

Ciantia, Matteo Oryem, Marcos Arroyo, Joanna Butlanska, and Antonio Gens. 2016. "DEM Modelling of Cone Penetration Tests in a Double-Porosity Crushable Granular Material." *Computers and Geotechnics* 73 (March): 109–27. https://doi.org/10.1016/j.compgeo.2015.12.001.

Cortes, D D, and S John. 2018. "Earthworm-Inspired Soil Penetration," 7.

Cundall, P A, and O D L Strack. 1979. “A Discrete Numerical Model for Granular Assemblies,” 19.

DeJong, Jason T., Matthew Burrall, Daniel W. Wilson, and J. David Frost. 2017. “A Bio-Inspired Perspective for Geotechnical Engineering Innovation.” In *Geotechnical Frontiers 2017*, 862–70. Orlando, Florida: American Society of Civil Engineers. https://doi.org/10.1061/9780784480472.092.

Del Dottore, Emanuela, Alessio Mondini, Ali Sadeghi, Virgilio Mattoli, and Barbara Mazzolai. 2016. “Circumnutations as a Penetration Strategy in a Plant-Root-Inspired Robot.” In *2016 IEEE International Conference on Robotics and Automation (ICRA)*, 4722–28. Stockholm, Sweden: IEEE. https://doi.org/10.1109/ICRA.2016.7487673.

———. 2017. “An Efficient Soil Penetration Strategy for Explorative Robots Inspired by Plant Root Circumnutation Movements.” *Bioinspiration & Biomimetics* 13 (1): 015003. https://doi.org/10.1088/1748-3190/aa9998.

Dorgan, Kelly M. 2015. “The Biomechanics of Burrowing and Boring.” *Journal of Experimental Biology* 218 (2): 176–83. https://doi.org/10.1242/jeb.086983.

Drnevich, Vp, Pw Mayne, and Jb Kemper. 1988. “Profiling OCR in Stiff Clays by CPT and SPT.” *Geotechnical Testing Journal* 11 (2): 139. https://doi.org/10.1520/GTJ10960J.

Gidmark, Nicholas J., James A. Strother, Jaquan M. Horton, Adam P. Summers, and Elizabeth L. Brainerd. 2011. “Locomotory Transition from Water to Sand and Its Effects on Undulatory Kinematics in Sand Lances (Ammodytidae).” *Journal of Experimental Biology* 214 (4): 657–64. https://doi.org/10.1242/jeb.047068.

Helms, Michael, Swaroop S. Vattam, and Ashok K. Goel. 2009. “Biologically Inspired Design: Process and Products.” *Design Studies* 30 (5): 606–22. https://doi.org/10.1016/j.destud.2009.04.003.

Huang, Sichuan, Yong Tang, Hosain Bagheri, Dongting Li, Alexandria Ardente, Daniel Aukes, Hamidreza Marvi, and Junliang (Julian) Tao. 2020. “Effects of Friction Anisotropy on Upward Burrowing Behavior of Soft Robots in Granular Materials.” *Advanced Intelligent Systems* 2 (6): 1900183. https://doi.org/10.1002/aisy.201900183.

Khosravi, A., A. Martinez, and J.T. DeJong. 2020. “Discrete Element Model (DEM) Simulations of Cone Penetration Test (CPT) Measurements and Soil Classification.” *Canadian Geotechnical Journal* 57 (9): 1369–87. https://doi.org/10.1139/cgj-2019-0512.

Kim, Hyunbin, and Seong-Wan Park. 2020. “DEM Simulation for Shear Behavior in Unsaturated Granular Materials at Low-Stress State.” *Computers and Geotechnics* 122 (June): 103551. https://doi.org/10.1016/j.compgeo.2020.103551.

Kobayashi, T., and R. Fukagawa. 2003. “Characterization of Deformation Process of CPT Using X-Ray TV Imaging Technique.”

Kong, X. Q., and C. W. Wu. 2009. “Measurement and Prediction of Insertion Force for the Mosquito Fascicle Penetrating into Human Skin.” *Journal of Bionic Engineering* 6 (2): 143–52. https://doi.org/10.1016/S1672-6529(08)60111-0.

Kuei, Kevin Charles. 2019. “Pile Dynamics and Shearing Behavior of Granular Soils.” Davis, CA: University of California Davis.

Lin, Jia, and Wei Wu. 2012. “Numerical Study of Miniature Penetrometer in Granular Material by Discrete Element Method.” *Philosophical Magazine* 92 (28–30): 3474–82. https://doi.org/10.1080/14786435.2012.706373.

Ling, Jintian, Lelun Jiang, Keyun Chen, Chengfeng Pan, Yan Li, Wei Yuan, and Liang Liang. 2016. “Insertion and Pull Behavior of Worker Honeybee Stinger.” *Journal of Bionic Engineering* 13 (2): 303–11. https://doi.org/10.1016/S1672-6529(16)60303-7.

Lobo-Guerrero, Sebastian, and Luis E. Vallejo. 2007. “Influence of Pile Shape and Pile Interaction on the Crushable Behavior of Granular Materials around Driven Piles: DEM Analyses.” *Granular Matter* 9 (3–4): 241–50. https://doi.org/10.1007/s10035-007-0037-3.

Mak, T. W., and L. H. Shu. 2004. “Use of Biological Phenomena in Design by Analogy.” In *Volume 3a: 16th International Conference on Design Theory and Methodology*, 2004:167–76. Salt Lake City, Utah, USA: ASME. https://doi.org/10.1115/DETC2004-57303.

Marchetti, S., P. Monaco, G. Totani, and M. Calabrese. 2001. “The Flat Dilatometer Test (DMT) in Soil Investigations A Report by the ISSMGE Committee TC16.” Encyclopedia of Earth Sciences Series. Cham: Springer International Publishing. https://doi.org/10.1007/978-3-319-73568-9_174.

Martinez, Alejandro, Jason DeJong, Idil Akin, Ali Aleali, Chloe Arson, Jared Atkinson, Paola Bandini, et al. 2021. “Bio-Inspired Geotechnical Engineering: Principles, Current Work, Opportunities and Challenges.” *Géotechnique*, April, 1–48. https://doi.org/10.1680/jgeot.20.P.170.

Mayne, Paul W. 2007. “Cone Penetration Testing State-of-Practice,” 137.

Mcdowell, G. R., O. Falagush, and H.-S. Yu. 2012. “A Particle Refinement Method for Simulating DEM of Cone Penetration Testing in Granular Materials.” *Géotechnique Letters* 2 (3): 141–47. https://doi.org/10.1680/geolett.12.00036.

Mishra, Anand Kumar, Francesca Tramacere, Roberto Guarino, Nicola Maria Pugno, and Barbara Mazzolai. 2018. “A Study on Plant Root Apex Morphology as a Model for Soft Robots Moving in Soil.” Edited by Josh Bongard. *PLOS ONE* 13 (6): e0197411. https://doi.org/10.1371/journal.pone.0197411.

O’Hara, Kyle B., and Alejandro Martinez. 2020. “Monotonic and Cyclic Frictional Resistance Directionality in Snakeskin-Inspired Surfaces and Piles.” *Journal of Geotechnical and Geoenvironmental Engineering* 146 (11): 04020116. https://doi.org/10.1061/(ASCE)GT.1943-5606.0002368.

O’Sullivan, Catherine. 2011. *Particulate Discrete Element Modelling*. Vol. 4. Spon Press.

Purdy, C., A.J. Raymond, J.T. DeJong, and A. Kendall. 2020. “Life Cycle Assessment of Site Characterization Methods. In Geo-Congress 2020.” *Geo-Congress 2020: Geo-Systems, Sustainability, Geoenvironmental Engineering, and Unsaturated Soil Mechanic*, 80–89.

Qian, Yu, Seung Jae Lee, Erol Tutumluer, Youssef M. A. Hashash, Debakanta Mishra, and Jamshid Ghaboussi. 2013. “Simulating Ballast Shear Strength from Large-Scale Triaxial Tests: Discrete Element Method.” *Transportation Research Record: Journal of the Transportation Research Board* 2374 (1): 126–35. https://doi.org/10.3141/2374-15.

Robertson. 2013. “Cone Penetration Test (CPT) Quality Control (QC).” Presented at the Webinar #10, Online. http://www.greggdrilling.com/wp-content/uploads/2017/08/greggdrilling_webinars_dorgP_BbwRyg.pdf.

———. 2016a. “Estimating Ko in Sandy Soils Using the CPT,” 5.

Robertson, and Campanella. 1983. “Interpretation of Cone Penetration Tests. Part I: Sand.” *Canadian Geotechnical Journal* 20 (4): 718–33. https://doi.org/10.1139/t83-078.

Robertson, P.K. 2016. “Cone Penetration Test (CPT)-Based Soil Behaviour Type (SBT) Classification System — an Update.” *Canadian Geotechnical Journal* 53 (12): 1910–27. https://doi.org/10.1139/cgj-2016-0044.

Sadek, Mohammad A., Mehari Tekeste, and Mojtaba Naderi. 2017. “Calibration of Soil Compaction Behavior Using Discrete Element Method (DEM).” In *2017 Spokane, Washington July 16 - July 19, 2017*. American Society of Agricultural and Biological Engineers. https://doi.org/10.13031/aim.201700777.

Shin, H., and J. C. Santamarina. 2011. “Open-Mode Discontinuities in Soils.” *Géotechnique Letters* 1 (4): 95–99. https://doi.org/10.1680/geolett.11.00014.

Sturm, Alexander Patrick. 2019. “On the Liquefaction Potential of Gravelly Soils: Characterization, Triggering and Performance,” 541.

Tao, Junliang (Julian), Sichuan Huang, and Yong Tang. 2020. “SBOR: A Minimalistic Soft Self-Burrowing-out Robot Inspired by Razor Clams.” *Bioinspiration & Biomimetics* 15 (5): 055003. https://doi.org/10.1088/1748-3190/ab8754.

Tovar-Valencia, Ruben D., Ayda Galvis-Castro, Rodrigo Salgado, and Monica Prezzi. 2021. “Effect of Base Geometry on the Resistance of Model Piles in Sand.” *Journal of Geotechnical and Geoenvironmental Engineering* 147 (3): 04020180. https://doi.org/10.1061/(ASCE)GT.1943-5606.0002472.

Wensrich, C.M., and A. Katterfeld. 2012. “Rolling Friction as a Technique for Modelling Particle Shape in DEM.” *Powder Technology* 217 (February): 409–17. https://doi.org/10.1016/j.powtec.2011.10.057.

Winter, A G, V, R L H Deits, D S Dorsch, A H Slocum, and A E Hosoi. 2014. “Razor Clam to RoboClam: Burrowing Drag Reduction Mechanisms and Their Robotic Adaptation.”

Bioinspiration & Biomimetics 9 (3): 036009. https://doi.org/10.1088/1748-3182/9/3/036009.

Wu, Y, and H Yamamoto. 2014. “Numerical Analysis of the Effect of Pile Tip Shape on Soil Behavior around Pile” 45: 13.

Zeng, Z, and Y Chen. 2016. “Simulation of Soil-Micropenetrometer Interaction Using the Discrete Element Method (DEM).” *Transactions of the ASABE* 59 (5): 1157–63. https://doi.org/10.13031/trans.59.11726.

Zhang, Ningning, Marcos Arroyo, Matteo Oryem Ciantia, Antonio Gens, and Joanna Butlanska. 2019. “Standard Penetration Testing in a Virtual Calibration Chamber.” *Computers and Geotechnics* 111 (July): 277–89. https://doi.org/10.1016/j.compgeo.2019.03.021.